UC Irvine
UC Irvine Electronic Theses and Dissertations

Title
Mechanics of Minimal Surface-based Architected Materials

Permalink
https://escholarship.org/uc/item/95z755kr

Author
Hsieh, Meng-Ting

Publication Date
2020

Supplemental Material
https://escholarship.org/uc/item/95z755kr#supplemental

Copyright Information
This work is made available under the terms of a Creative Commons Attribution License, availalbe at https://creativecommons.org/licenses/by/4.0/

Peer reviewed|Thesis/dissertation

eScholarship.org Powered by the California Digital Library
University of California

UNIVERSITY OF CALIFORNIA,
IRVINE

Mechanics of Minimal Surface-based Architected Materials

DISSERTATION

submitted in partial satisfaction of the requirements
for the degree of

DOCTOR OF PHILOSOPHY

in Mechanical and Aerospace Engineering

by

Meng-Ting Hsieh

Dissertation Committee:
Professor Lorenzo Valdevit, Chair
Associate Professor Mo Li
Assistant Professor Edwin P. Hernandez

2020

© 2020 Meng-Ting Hsieh

DEDICATION

To my parents and my brother,

whose unconditional love and support made it possible for me to complete this work.

To my friends,

whose encouragement motivated me to overcome the challenges in my Ph.D. study.

To Albert Einstein,

whose contributions to the mankind inspired me to be a scientist since I was small.

To almighty God,

I thank you for giving me strength, wisdom, skills, and patience.
I thank you for your protection and blessings.
Lastly, I thank you for all the obstacles you put in my life to help me a better person.

I always believe
天将降大任于斯人也, 必先苦其心志, 劳其筋骨, 饿其体肤 ,空乏其身, 行拂乱其所为
Before God gives a great purpose and responsibility to us,
we will be challenged, tested, trialed so that we can be ready.

TABLE OF CONTENTS

Page

LIST OF FIGURES v

LIST OF TABLES xi

ACKNOWLEDGEMENTS xii

CURRICULUM VITAE xiii

ABSTRACT OF THE DISSERTATION xvii

CHAPTER 1 Introduction 1

1.1 Overview 1
1.2 Mechanics of architected cellular materials 2
1.2.1 Stiffness and strength of cellular materials 2
1.2.2 Strut-based topology 3
1.2.3 Shell-based topology 4
1.2.4 Advantages of nanoscale architectures and associated scalability issues 5
1.3 Architected material for bone implants 6
1.3.1 The need of bone implants 6
1.3.2 Requirements for bone implants 6
1.3.3 Categories of bone implants 7
1.3.4 Design of porous metallic implants with cellular materials 8
1.3.5 State-of-the-art implant topologies 9
1.4 Approaches to obtain the fracture toughness of architected cellular materials 10
1.4.1 Fracture toughness of cellular materials 10
1.4.2 Dimensional analysis 10
1.4.3 Continuum Cosserat theory 11
1.4.4 Finite element modeling on the single-edge-notched-bend and center-cracked plate 12
1.4.5 Boundary layer analysis 13
1.5 Problem statement and research objectives 15

CHAPTER 2 The mechanics of architected materials with spinodal topologies 18
2.1 Introduction 18
2.2 Numerical construction of spinodal topologies 20
2.2.1 Generation of solid spinodal topologies 20
2.2.2 Calculation of the characteristic feature size 21
2.2.3 Generation of shell spinodal topologies 24
2.2.4 Calculation of the surface curvature 25

2.3 Mechanical performance of spinodal topologies 26
2.3.1 Numerical modeling of mechanical response 26
2.3.2 Imperfection sensitivity analysis 28
2.3.3 Experimental verification 32
2.3.4 Scaling laws and mechanical performance 33
2.4 Conclusion 42

CHAPTER 3 Architected implant designs for long bones: The advantage of minimal-surface based topologies 44
3.1 Introduction 44
3.2 Materials and methods 45
3.2.1. Synopsys of approach 45
3.2.2. Generation of composite topologies 46
3.2.3. Investigation of interfacial morphology 50
3.2.4. Mechanical simulations 51
3.3 Results and discussion 53
3.3.1 Young's modulus 53
3.3.2 Interfacial surface area 57
3.3.3 Safety factor: peak stress 58
3.3.4 Relative bone growth index 60
3.4 Conclusions 63

CHAPTER 4 A versatile numerical approach to obtain fracture toughness/R-curve of cellular materials 65
4.1 Introduction 65
4.2 The numerical model 66
4.2.1 Synopsis 66
4.2.2 Specimen design 68
4.2.3 Constitutive and damage models 70
4.2.4 Finite element methodology for extraction of the fracture toughness 71
4.3 Fracture toughness of 2D lattices 74
4.3.1 Mechanisms of deformation and damage and the size of the plastic zone 74
4.3.2 Scaling relations for fracture toughness and R-curve 81
4.4 Discussion 85
4.5 Conclusions 87

CHAPTER 5 Summary and conclusions 89

REFERENCES 92

APPENDICES 106

SUPPLEMENTARY MATERIALS 122

LIST OF FIGURES

Page

Fig. 1.1 (a) Long bones (indicated in red hollow circles): femur, tibia, fibula, radius, ulna, and humerus in human skeleton [68,69] and (b) Anatomy of a long bone [69] for illustration purposes. 8

Fig. 2.1 Examples of self-assembled spinodal topologies at different length scales: (a) nano-porous Au, obtained by selective etching of Au/Ag solid solutions (reproduced from [123]); (b) spinodally decomposed bijel (reproduced from [124]); (c) micro-porous metallic shell spinodal architected material, obtained by material conversion of spinodally decomposed bijels (reproduced from [124]). 19

Fig. 2.2 3D spinodal solid models with different relative densities, $\bar{\rho} = 0.2, 0.3, 0.5,$ and 0.7 extracted at different evolution times, t_1, t_3, and t_5. 21

Fig. 2.3 2D slices of spinodal solid models in (a) space domain and (b) frequency domain, at different relative densities ($\bar{\rho} = 0.2, 0.3, 0.5,$ and 0.7) and different evolution times (t_1, t_3, and t_5). The characteristic feature size is extracted from the FFT transforms of the models, and depends on the evolution time, but not on the relative density. 22

Fig. 2.4 Time evolution of the inverse of the characteristic feature size, as extracted from 3D FFT analyses of solid spinodal models. (a) FFT amplitude along the x direction at five evolution times; the frequency with highest amplitude is the inverse of the characteristic feature size. (b) The characteristic feature size scales with the cubic root of the evolution time (normalized by t5), as predicted by the LSW theory of spinodal decomposition. 23

Fig. 2.5 (a) 3D spinodal shell models corresponding to the interfaces of spinodal solid models of $\bar{\rho} = 0.5$, extracted at three different evolution times (t_1, t_3, and t_5). (b) Relative density of shell spinodal cellular materials, as a function of the shell thickness, b, normalized by the characteristic feature size, λ. L denotes the cubic domain size. 25

Fig. 2.6 Principal curvature maps of the surface of shell spinodal models, derived from different relative densities ($\bar{\rho} = 20\%, 30\%, 50\%,$ and 70%) and different characteristic features sizes ($\frac{\lambda}{L} = \frac{1}{8}, \frac{1}{5},$ and $\frac{1}{3}$) of solid spinodal preforms. Notice that only the 50%-derived shell topology has near-zero mean curvature, $H = \frac{1}{2}(\kappa_1 + \kappa_2)$, throughout the surface. 27

Fig. 2.7 Finite element model of (a) a solid spinodal model ($\bar{\rho} = 50\%$) and (b) the corresponding shell spinodal model. The nodes on the positive x surface are highlighted in red indicating how the boundary conditions are applied to the models. (c-d) Boundary conditions applied to a spinodal solid model in the x-y and x-z planes. Red, green, and blue

triangles indicate that translations are constrained along the x, y, and z directions, respectively. The sides opposite to those indicated with red, green, and blue triangles are allowed to displace in the x, y, and z directions, respectively, but with the condition that all nodes on the side displace by the same amount. The same boundary conditions are applied to spinodal shell models. 29

Fig. 2.8 Comparisons of perfect (a,c) and perturbed (c,d) meshes for spinodal shell topologies with characteristic feature size, $\frac{\lambda}{L} = \frac{1}{8}$ (a,b) and $\frac{\lambda}{L} = \frac{1}{3}$ (c,d).The magnitude of the imperfection is equal to $\psi = 20$ (b) and $\psi = 9.3$ (d), respectively. Red circles in (a,b) represent examples of subtle imperfections. 31

Fig. 2.9 Imperfection insensitivity of shell spinodal models. The non-dimensional imperfection magnitude, ψ, is defined as the largest displacement from a perfect mesh normalized by the shell thickness. Comparison of post-buckling stress-strain curves of 10% dense spinodal shells with characteristic feature size, $\frac{\lambda}{L} = \frac{1}{8}$ (a) and for $\frac{\lambda}{L} = \frac{1}{3}$ (b), with three different magnitudes of imperfection. The constituent material has Young's modulus, $E_s = 210$ GPa and yield strength, $\sigma_{ys} = 235$ MPa. 31

Fig. 2.10 Comparison of numerical and experimental stress-strain curves for (a) solid and (b) shell spinodal topologies at different relative densities, loaded in uniaxial compression. The characteristic feature size, $\frac{\lambda}{L} = \frac{1}{5}$ is used for all models. The insets depict SEM images of the samples, fabricated by two-photon polymerization Direct Laser Writing in IP-Dip, with a Nanoscribe GT Photonics Professional, and tested with an Alemnis Nanoindenter. Higher resolution SEM images of all samples are shown in Fig. S1. The properties of IP-Dip were measured by micropillar compression tests, and input in the simulations as an elastic-perfectly plastic solid with $E_s = 2$ GPa, and yield strength $\sigma_{ys} = 60$ MPa. 34

Fig. 2.11 Numerical predictions of (a) Relative Young's modulus and (b) relative yield strength of spinodal solid models, as a function of their relative density, $\bar{\rho}$. Hollow markers indicate models with isolated internal islands, which have been excluded from the scaling calculations. The constituent material has Young's modulus, $E_s = 210$ GPa and yield strength, $\sigma_{ys} = 235$ MPa. Different curves refer to models with different characteristic feature size, λ. L denotes the domain size. 35

Fig. 2.12 Numerical predictions of (a) Relative Young's modulus and (b) relative yield strength of spinodal shell models, as a function of their relative density, $\bar{\rho}$. The constituent material has Young's modulus, $E_s = 210$ GPa and yield strength, $\sigma_{ys} = 235$ MPa. Different curves refer to models with different characteristic feature size, λ. L denotes the domain size. The black dots mark the transition from yielding to buckling failure. 37

Fig. 2.13 – Comparison of von Mises stress distribution in a hollow microlattice unit cell with bar aspect ratio ~6, and angle $\theta = 60^{\circ}$ [10] and a spinodal shell model with characteristic feature size, $\frac{\lambda}{L} = \frac{1}{3}$, both at relative density of 0.01%, and under a compressive strain of 0.1%.

The constituent material has Young's modulus, $E_s = 210$ GPa and yield strength, $\sigma_{ys} = 235$ MPa. The stress limits (used to distinguish stress contours where $\frac{\sigma_{vm}}{\sigma_{limit}} \geq 1$) are colored "red", with $\sigma_{limit} = 4$ MPa. Notice that the spinodal shell topology has a much more uniform stress distribution, yielding excellent mechanical efficiency. 38

Fig. 2.14 The effect of mean surface curvature, H, on the mechanical efficiency of shell spinodal topologies. The insets display contours of von Mises stress. Notice that spinodal shell topologies derived from 50%-dense spinodal solids (and hence exhibiting near-zero mean curvature everywhere on the surface) are more efficient than spinodal shell topologies of equal relative density but derived from 20% and 70% solid spinodals (and hence having non-zero mean curvatures throughout the surface). The constituent material has Young's modulus, $E_s = 210$ GPa and yield strength, $\sigma_{ys} = 235$ MPa. The stress limits (used to distinguish stress contours where $\frac{\sigma_{vm}}{\sigma_{limit}} \geq 1$) are colored "red", with (a) $\sigma_{limit} = 2.2$ MPa and (b) $\sigma_{limit} = 2$ MPa. 39

Fig. 2.15 Comparison of the mechanical performance of solid and shell spinodal topologies and well-established strut-based and shell-based architected materials: hollow octahedral-type metallic microlattices [11], hollow octet ceramic nanolattices [12], hollow octet metallic microllatices [138], hollow octahedron-octet nanolattices [137], solid glassy carbon nanolattices [30], double gyroid nanolattices [32], P-surface [20] and D-surface [27] architected materials. Only spinodal topologies with characteristic feature size, $\lambda/L = 1/5$ are depicted for clarity, for two different values of the base material yield strain: ε_{ys}=0.01 (representative of IP-Dip, thus allowing direct comparison with experimental results) and ε_{ys}=0.001 (representative of a metal). Also depicted are the Hashin-Shtrikman upper bound for stiffness [97] and the Suquet-Ponte-Castaneda nonlinear upper bound for strength [32,97–99], which represent theoretical limits for the mechanical performance of isotropic cellular materials. 41

Fig. 3.1 The numerical generation process of (a) octet lattice, (b) Schwartz P shell and (c) spinodal-shell reinforced composites. For illustration purposes, only 10%-reinforced composites are shown. All insets are not drawn to scale. 49

Fig. 3.2 Illustration of the applied boundary conditions in the y-z and x-y plane. The triangles represent roller supports. 52

Fig. 3.3 (a) Effective Young's modulus E of composites with four different implant topologies (represented by the markers) — octet, primitive, early-stage and late-stage spinodal— with three different implant constituent materials (represented by colors) — Ti-6Al-4V, 316L SS, and Co-Cr-Mo — at implant relative density $\bar{\rho}_r = 0.1, 0.2$ and 0.3. The typical Young's modulus range for human long bones are bounded by two brown dashed lines [149,150,159–162,151–158]. (b) The von Mises stress field in both the encompassed tissue and the implant of the composites under 1% uniaxial compressive strain. The stress legend bar is limited by

a stress limit σ_{limit} such that all stresses above it are colored with red. E_b is the base material Young's modulus. 55

Fig. 3.4 Relative Young's modulus E/E_b versus interfacial surface area constant D for implant topologies: octet, primitive, early and late stage spinodal with relative densities of 10%, 20%, and 30% ($\bar{\rho}_r = 0.1$, 0.2, and 0.3). 58

Fig. 3.5. Relative Young's modulus E/E_b versus minimum safety factor $SF_{min} = \sigma_y/S_{peak}$ (S_{peak} is the von Mises peak stress and σ_y is the yield strength of Ti-6Al-4V) for octet, primitive, early and late stage spinodal implants with relative densities of 10%, 20%, and 30% ($\bar{\rho}_r = 0.1, 0.2,$ and 0.3). 60

Fig. 3.6 Bone growth index I in the tissue (the green matrix phase in each composite inset) surrounding octet lattice, Schwartz P shell and spinodal shell-based implants versus effective Young's modulus E/E_b. 61

Fig. 3.7. The maximum shear strain S_{maxs} and the volumetric strain S_{vol} field experienced in the tissue matrix phase (analogous to the encompassed tissue of an implant) of octet, primitive, early and late-stage spinodal-reinforced composites. 62

Fig. 4.1 (a) Unit cell topology and (b) SENB (single edge notched bend) specimen dimensions of triangular, kagome, and hexagonal specimens from top to bottom. Out-plane thicknesses are shown to illustrate the physical dimensions that would be required to perform a SENB experiment in accordance with ASTM standard; these thicknesses are irrelevant for the 2D plane-strain simulation performed in this work. 70

Fig. 4.2 Representative stress-strain curves of (a) constitutive and damage model, (b) titanium alloy (Ti-6Al-4V), and (c) silicon carbide. 71

Fig. 4.3 (a) Boundary conditions on a SENB specimen made of 2D lattices. Three spreaders are used: one at the top midspan and two at the bottom locations distance 4W from each other, to prevent highly localized deformation. Load-line displacement are applied at the top spreader while each of the bottom spreaders can rotate around a reference point, representing the center of a roller. (b) Construction of R-curve with fracture toughness, K_J against normalized change of crack length, $\frac{\Delta a}{a}$. Two-term power law fit, $K_J = K_{JIC} + c(\frac{\Delta a}{a})^m$, where K_{JIC} is the initial fracture toughness, c is the toughening coefficient, and m is the toughening power. 74

Fig. 4.4 Deformation maps of topological specimens made of silicon carbide at $\bar{\rho}$ =13% and 20%: (a) load, P, versus load-line displacement, v, were plotted till overall kinetic energy exceeds 5% of overall internal energy of each specimen in each simulation. Encircled number one corresponds to the initial fracture followed immediately by catastrophic failures (significant load drop) and(b) the corresponding initial fracture locations are represented by red dashed line (c) Illustration of crack branching of the $\bar{\rho}$ =20% triangular lattice immediately after fracture. All lattices are not drawn to scale. 77

Fig. 4.5 Deformation maps of topological specimens made of Titanium Alloy (Ti-6Al-4V) at $\bar{\rho}$ =13% and 20%: load, P, versus load-line displacement, v, of (a) triangular specimens, (b) kagome lattices, and (c) hexagonal lattices were plotted till overall kinetic energy exceeds 5% of overall internal energy of each specimen in each simulation. Encircled number one corresponds to initial fracture and the subsequent encircled numbers correspond to each load drop. The fracture locations of each encircled number in (a), (b), and (c) are represented by corresponding colored dashed line in (d), (e), and (f) respectively; the lattices are not drawn to scale. 78

Fig. 4.6 Contours of absolute normalized plastic strain, $\varepsilon_p/\varepsilon_{plimit}$, around the crack tip between (a) triangular lattices, (b) kagome lattices, and (c) hexagonal lattices made of titanium alloy (Ti-6Al-4V) with ℓ = 3 mm at relative density, $\bar{\rho}$ = 20% and 13% right before the initial fracture. The corresponding location on the load-displacement curve of each contour is indicated by a red dot. Plastic strain limit, ε_{plimit} = 0.01 is used in the strain contours such that for all $\varepsilon_p/\varepsilon_{plimit} > 1$, the contour appears to be red. Red rectangles or circles are used to estimate the size of plastic regions. The inset lattices are not drawn to scale. 80

Fig. 4.7 Scaling relationships for initial fracture toughness in triangular, kagome, hexagonal specimens made in silicon carbides with (a) the relative density $\bar{\rho}$ and (b) the square root of bar length, $\sqrt{\ell}$. 83

Fig. 4.8 Scaling relationships for initial fracture toughness in triangular, kagome, hexagonal specimens made in titanium alloys (Ti-6Al-4V) with (a) the relative density $\bar{\rho}$ and (b) the square root of bar length, $\sqrt{\ell}$. 83

Fig. 4.9 (a) scaling relationships for toughening coefficients, C, and (b) R-curves of triangular, kagome, and hexagonal specimens made in titanium alloy (Ti-6Al-4V). 84

Fig. 4.10 Material space charts for fracture toughness versus density. Three lattices are shown by their representative unit cell topologies: triangular (red), kagome (black), and hexagonal (blue). The prediction is based on titanium alloy material properties with the bar length, ℓ = 3 mm. 85

Fig. C1 Determination of 1% von Mises stress threshold as the peak stress in a porous implant. Percentage of the porous implant volume is defined as the volume of partial implant regions, that have a specific von Mises stress value, divided by the total volume of the implant. 111

Fig. E1 Specimen design: number of unit cells. (a) Specimen aspect ratio. (b) Normalized axial stress contour of triangular specimens at number of unit cells, n_y = 8 and n_y = 40. (c) Convergence of the pre-factor, D, with number of unit cells, n_y. The chosen n_y for the simulations are circled in black. 115

Fig. F1 Specimen design: number of elements per bar. (a) Demonstration of refined mesh

region around the crack tip. (b) Magnified views of mesh seeding around the crack tip with number of elements per bar, n_e = 4 and n_e = 50. (c) Convergence of the load-line displacement, at which the maximum axial strain around the crack tip reached ε_f, with number of elements per bar, n_e. The chosen n_e for simulations are circled in red. 117

Fig. G1 Illustration of boundary conditions applied in linear perturbation analyses: (i) two pin-jointed supports at 4W distance apart to prevent translate in the vertical direction and (ii) a fixed boundary condition applied at the left pin-jointed support to prevent rigid body motion. 118

Fig. H1 Illustration of load-line reaction force, P, versus load-line displacement, v, at crack extension instant i = 1 and 2 with the area under the curve, A_{pl}, at crack extension instant i = 1 for J-integral calculations. 121

Fig. S1 SEM images of spinodal samples fabricated in IP-Dip by two-photon polymerization Direct Laser Writing. All samples have characteristic feature size, $\frac{\lambda}{L} = \frac{1}{5}$, with L the domain size. (a) Spinodal solid model, $\bar{\rho}$ = 50%. (b) Spinodal solid model, $\bar{\rho}$ = 30%. (c) Spinodal solid model, $\bar{\rho}$ = 20%. (d) Spinodal shell model, $\bar{\rho}$ = 10%. (e) Spinodal shell model, $\bar{\rho}$ = 7%. (f) Spinodal shell model, $\bar{\rho}$ = 5%. 122

Fig. S2 Uniaxial response of the material IP-Dip, measured by compression experiments on micro-pillars of aspect ratio of 4 and different diameters, manufactured by two-photon polymerization Direct Laser Writing with a Nanoscribe Photonics GT Professional. 123

LIST OF TABLES

Page

Table 3.1 The effective Young's modulus E of composites with spinodal, primitive, and octet implant topologies. 56

Table 3.2 The typical Young's modulus of human long bones. 66

Table 4.1 Pre-factors, D, and scaling exponents, d, for mode-I initial fracture toughness, K_{IC} (elastic brittle base materials) and K_{JIC} (elastoplastic base materials) of triangular, kagome, and hexagonal lattices. Results are taken from [I] [108], [II] [120], * current work. The strain hardening exponent, p =16* is obtained by fitting the titanium alloy material properties used in this work to Ramberg-Osgood description. ℓ is the bar length. ε_{ys} is the yield strength, and ε_f is the fracture strain. 68

Table 4.2 Specifications of triangular, kagome, and hexagonal specimens with bar length of (a) ℓ = 3 mm and (b) ℓ = 10 mm. 69

Table G1 Natural frequencies of titanium alloy (Ti-6AL-4V) lattice specimens made of triangular, kagome, and hexagonal topologies, at $\bar{\rho}$ = 0.13, 0.16, and 0.2. Base material properties of modified Young's modulus, E_s' = 135 GPa and Poisson's ratio, ν_s' = 0.43, and density ρ_s = 4,500 kg/m^3 were used. 119

ACKNOWLEDGEMENTS

I would like to express my deep gratitude towards my advisor, Professor Lorenzo Valdevit, who has guided me to become a well-rounded scientist during the past five years. Academically, he always provides interesting ideas and practical research directions. He has always been inspiring, encouraging and patient to his students. His help is very significant in all aspects of my Ph.D. life in developing new computational methods, improving my presentation and writing skills, and providing me opportunities to connect with other professors.

I would also like to appreciate the members of my thesis committee, Professor Mo Li and Professor Edwin P. Hernandez for their ideas and suggestions to improve my computational models. In addition, I would like to thank them for taking their time refining my thesis and presentations.

I am also much obliged to Professor Vikram Deshpande and Professor Matthew Begley for their participation in my research discussion and coauthoring my papers.

Special thanks go to all the current and past members of the Architected Materials Lab for their willingness to help coworkers in need. I thank you for providing a collaborative environment necessary for the advancement of scientific research. It was my great honor and pleasure to work with such amazing researchers, Dr. Babak Haghpanah, Dr. Vladyslav Turlo, Dr. Ladan Sharif, Dr. Zhifeng Huang, Dr. Anna Izard, Dr. Jens Bauer, Yunfei Zhang, and Marti Casanovas, just to name a few. Our discussions have stimulated creative research ideas and helped me solve some of my most difficult research problems.

In addition, I gratefully acknowledge the financial support from the Air Force Office of Scientific Research (PM: Dr. Joycelyn Harrison, Contract # FA9550-14-1-0352), NASA Early Stage Innovation program (award #80NSSC18K0259), and the Office of Naval Research (program Manager: D. Shifler, Award No. N00014-17-1-2874).

Finally, I would like to thank UCI High Performance Computing Department for providing all the technical resources and advices on parallel computing necessary for the completion for my Ph.D. study.

Thank you all for taking a part in my Ph.D. life.

CURRICULUM VITAE

Meng-Ting Hsieh

EDUCATION

Ph.D., Mechanical and Aerospace Engineering	2020	**University of California, Irvine** *Advisor*: Lorenzo Valdevit. *Thesis:* 'Mechanics of Minimal Surface-based Architected Materials'
Master of Science, Mechanical and Aerospace Engineering	2014	**Oklahoma State University**
Bachelor of Science, Aerospace Engineering	2012	**Wichita State University**

Research Interests

Meng-Ting Hsieh is interested in the general area of mechanics of materials and solid mechanics developing novel analytical techniques and numerical approaches to solve problems encountered in materials at multiple length scales.

Research Experiences

Department of Mechanical and Aerospace Engineering, UCI December 2015- Present

Graduate Research Assistant

Project: Thermo-structurally optimized lattice materials and structures for large-scale space applications

(In collaboration with Professor Jaeho Lee at UCI)

- Developed a numerical approach to calculate the fracture toughness and R-curve of cellular materials
- Modeled the high-speed debris impact on sandwiched primitive shells using spherical particle hydrodynamics

Project: Armor as a system: Multi-threat mitigation by optimal design of nano-architected composite materials

- Simulated large deformation response of interpenetrating phase composites with octet, primitive, and spinodal reinforcement

Project: Optimal low-density materials with architected porosity from the nano to the macro scale

(In collaboration with Professor Andrea Hodge (USC))

- Fully investigated the mechanical response (stiffness, strength, and imperfection sensitivity) of cellular materials with spinodal topology

Journal Publications

[J1] **M.-T. Hsieh**, M. Begley, L. Valdevit*, Architected implant designs for long bones: The advantage of minimal surface-based topologies, Materials and Design (2020), in preparation.

[J2] Y. Zhang, **M.-T. Hsieh**, L. Valdevit*, Mechanical performance of 3D printed interpenetrating phase composites with spinodal topologies, Composite Structures (2020), submitted.

[J3] **M.-T. Hsieh***, L. Valdevit, Minisurf – A minimal surface generator for finite element modeling and additive manufacturing, Software Impacts. 6 (2020) 100026. doi:10.1016/j.simpa.2020.100026.

[J4] **M.-T. Hsieh**, V.S. Deshpande, L. Valdevit*, A versatile numerical approach for calculating the fracture toughness and R-curves of cellular materials, J. Mech. Phys. Solids. 138 (2020) 103925. doi:10.1016/j.jmps.2020.103925.

[J5] **M.-T. Hsieh**, B. Endo, Y. Zhang, J. Bauer, L. Valdevit*, The mechanical response of cellular materials with spinodal topologies, J. Mech. Phys. Solids. 125 (2019) 401–419. doi:10.1016/J.JMPS.2019.01.002.

*Corresponding author

Presentations at Conferences

[P1] 'The mechanical response of architected materials with spinodal topologies', Society of Engineering Science Meeting, Northeastern University, Boston, MA, July 25-28, 2017.

[P2] 'Spinodal structures with supreme scaling laws', Mach Conference, Annapolis, MD, April 4-6, 2018.

[P3] 'Fracture toughness of truss and shell-based architected materials', Materials Research Society, Boston, MA, November 26-29, 2018.

Invited lectures and seminars

[I1] 'Mechanics of architected materials with minimal surface characteristics', Civil and Environmental Engineering Department, University of California at Los Angeles, Los Angeles, CA, June 16th, 2020.

Professional Appointments

University of California, Irvine June - August 2020

Teaching Associate (lecturer) of Mechanics of Materials

U.S. Food and Drug Administration (FDA) July - September 2019

Engineering Intern

Honor and Awards

UCSF-Stanford Center of Excellence in Regulatory Science and Innovation (CERSI) fellowship

Certificates

[C1] Certificate of Completion of the 2020 Summer Remote Teaching Institute for Grads and Postdocs, Division of Teaching Excellence and Innovation, University of California at Irvine, Irvine, CA, August 2020.

Teaching Experience

Department of Mechanical and Aerospace Engineering, UCI

Instructor for MAE 150 – Mechanics of Materials	June – August 2020
Teaching Assistant for MAE 150	September – December 2019
Teaching Assistant for MAE 150	September – December 2018
Teaching Assistant for MAE 157 – Lightweight structures	January – March 2018
Teaching Assistant for MAE 255 – Laminated composite materials	April - June 2017
Teaching Assistant for MAE 150	September – December 2015

ABSTRACT OF THE DISSERTATION

Mechanics of Minimal Surface-based Architected Materials

by

Meng-Ting Hsieh

Doctor of Philosophy in Mechanical and Aerospace Engineering

University of California, Irvine, 2020

Professor Lorenzo Valdevit, Chair

For decades, high strength and high fracture toughness have been among the most sought-after mechanical properties by scientists and engineers in the field of light-weight materials. One way to achieve such mechanical properties is by using an architected cellular material (a two-phase material where one phase is void space and the other phase is the constituent solid, with the volume fraction of the latter defining the relative density $\bar{\rho}$) with optimized unit cell topology. Hence, one can design a lighter and lighter cellular material with the same constituent solid by reducing $\bar{\rho}$ while striving to achieve the highest possible strength and fracture toughness. In addition, size effect (often leading to a 'smaller is stronger' behavior) can further improve mechanical properties if the constituent solid is a metal or a ceramic with nanoscale dimensional features.

The ultimate material is hence an architected material with an optimal topology at the nanoscale. However, such materials are often not scalable by conventional additive manufacturing technologies for practical engineering applications. We propose that the spinodal cellular topology derived from spinodal decomposition of a solid (or liquid) solution could provide a possible solution, as such a process followed by material conversion techniques has been demonstrated to produce architected material samples with overall size in the centimeter range and the smallest feature size of the architecture ranging from a few hundred nanometers to tens of microns. Unlike topologically optimized architected materials (which are almost always periodic), spinodal-derived architected materials are intrinsically stochastic. Given the large body of knowledge that supports the structural benefit of periodic architectures, a fundamental question arises on the mechanical efficiency of these stochastic topologies.

In this thesis, we first numerically investigate the stiffness and strength of architected materials with spinodal topologies, considering both spinodal cellular solids (when one spinodally decomposed phase represents the solid constituent) and spinodal cellular shells (where the solid constituent occupies the thickened interface between two spinodally decomposing phases). We show that spinodal cellular solids are generally inferior to state-of-the-art topologies, whereas spinodal cellular shells are extremely stiff, strong, and imperfection-insensitive, features attributed to their minimal surface characteristics.

Inspired by the excellent mechanical efficiency and scalability of spinodal shell topology, and the possibility to design spinodal shell architected materials with extremely large specific surface area (the smaller the unit cell size, the larger the surface area per unit

volume), we numerically explore the potential benefits of these architected materials as porous long bone bio-implants, and compare them with more established periodic truss and minimal surface-based designs. By using mechanical and bio-mechanical performance indices, we suggest that minimal surface-based topologies are in general more suitable for bone implants than beam-based topologies. Furthermore, we show that spinodal shells have the potential to evoke more bone growth via periodic application of shear stresses to the surrounding tissues. When coupled with the intrinsic scalability of spinodal shell-based architected materials, which allows fabrication of biologically relevant implants with pore sizes at the micron-millimeter range (hence promoting large tissue/implant contact), these results suggest a strong potential as long bone implant materials.

Although micro/nano-architected materials can be designed with exceptional specific strength, their fracture toughness (an essential engineering properties for structural materials) is typically very low. While compressive strength and stiffness are relatively easy properties to model and experimentally measure in architected materials, extraction of fracture toughness (whether from numerical or experimental approaches) is much more challenging. In the final chapter of this thesis, we develop a versatile numerical approach to calculate the fracture toughness/R-curve of a cellular material. The approach is based on Finite Elements Analysis of the J-integral on a single-edge-notch-bend specimen, with a local maximum strain-based damage model. This approach is applied to 2D isotropic lattices. We show that the initial fracture toughness calculated from our approach agrees well with the results obtained from other methods. In addition, we show that careful design of unit cell topology can result in values of the steady-state fracture toughness that match or even exceed the initial fracture toughness of the constituent material itself. In the future, we plan

to apply this approach to investigate the fracture toughness and R-curve of spinodal shells-based architected materials, with the overarching goal of identifying design strategies to optimize this essential property.

CHAPTER 1

Introduction

1.1 Overview

Architected materials are multi-phase solids consisting of many repeating unit cells whose topology can be optimally designed to result in the desired effective properties or functionalities. Because of this multifunctional tunability, architected materials have been widely used in a wide range of multi-disciplinary fields. For mechanical functionality, the unit cell topology can be optimized to obtain unprecedented stiffness, strength, and fracture toughness at ultra-low relative density. In addition, recent advancements in additive manufacturing technologies allow architected materials with nearly arbitrary unit cell complexity to be fabricated in a relatively scalable manner (subject to limitations discussed in section 1.2.3) for several practical engineering applications, from metamaterials for controlled wave-matter interaction to bone implants.

In this chapter, we provide an overall introduction to three aspects of architected materials performance and design that are investigated in this thesis: (i) stiffness and strength of architected cellular materials, (ii) bio-mechanical properties of architected cellular materials relevant for bone implant applications, and (iii) fracture toughness of architected cellular materials. We first introduce two classes of unit cell topologies (strut and shell-based topologies) and explore the impact of unit cell topology on stiffness and strength. We then proceed to discuss the benefits of micro/nanoscale unit cell dimensions and the associated issue of scalability (section 1.2). Second, we explore the opportunities of using

architected materials in porous bone implants: the need, requirements, and the types of common bone implants are briefly discussed, together with advantages and disadvantages of state- of-the-art implant topologies (section 1.3). Third, we introduce the most common approaches to calculate the fracture toughness of architected cellular materials, including analytical (dimensional analysis and continuum Cosserat theory) and numerical approaches (finite element modeling on established fracture toughness specimens and boundary layer analysis) (section 1.4). We conclude this chapter with a concise problem statement for this thesis and the key research objectives (section 1.5).

1.2 Mechanics of architected cellular materials

1.2.1 Stiffness and strength of cellular materials

Architected materials are multi-phase materials. In the simplest form, we can have bi-phase architected materials where one phase is void and the other phase is the constituent material, also known as "architected cellular materials" or "cellular materials" in short. Their Young's modulus, *E,* and yield (or buckling) strength, σ_y, are a strong function of the relative density, $\bar{\rho}$ (i.e., the volume fraction of the constituent material phase), generally following a power-law behavior: $E \sim E_s \bar{\rho}^{\,n}$ and $\sigma_y \sim \sigma_{ys} \bar{\rho}^{\,m}$, with E_s and σ_{ys} the Young's modulus and yield (or buckling) strength of the constituent material, respectively. The values of the exponents *n* and *m* have a dramatic effect on the mechanical efficiency of the material and are strongly affected by the topology of the unit cell architecture [1].

1.2.2 Strut-based topology

The mechanical properties of open-cell, strut-based cellular materials like foams and lattices have been studied extensively over the past two decades [2–4]. Depending on the nodal connectivity (number of struts meeting at each node) and the balance between the number of states of self-stress and internal mechanisms, strut-based topologies can be classified into bending-dominated or stretching-dominated: in the former, local deformation upon global loading (e.g., compression) occurs primarily by bending of the struts (a weak deformation mode); by contrast, in the latter the vast majority of the strain energy is stored by axial deformation of the struts [5]. The implication is that stretching-dominated lattices are much more mechanically efficient than bending dominated lattices, with effective stiffness and yield strength scaling as $E, \sigma_y \sim (\bar{\rho})^1$ (versus $E \sim (\bar{\rho})^2$ and $\sigma_y \sim (\bar{\rho})^{1.5}$ for bending-dominated 3D lattices and stochastic foams) [6]. In all cases, at low relative density, strut buckling limits the strength of both stretching- and bending-dominated lattices. For nearly any strut-based lattice architecture, the effective elastic buckling strength scales with $\bar{\rho}$ as $\sigma_{el} \sim (\bar{\rho})^2$ [2,7,8], dramatically reducing mechanical performance at low relative densities. For most solid-strut topologies, the yielding-to-buckling transition occurs at a relative density of the order of ~1% [9].

Hollow-strut lattices can potentially delay the onset of buckling, shifting the yielding-to-buckling transition to $\bar{\rho}$<0.1% [10–16]. However, their mechanical properties are often much worse than analytical predictions suggest: for example $E \sim (\bar{\rho})^{1.61}$ and $\sigma_y \sim (\bar{\rho})^{1.76}$ has been experimentally extracted for hollow-strut ceramic octet lattices [12]. The hollow nodes of these lattices were shown to deform through bending (regardless of the nodal

connectivity); this phenomenon, coupled with stress concentration at the nodes, causes a knock-down from classical scaling laws, which do not account for nodal topology [10,12,13,15,17,18]. Local node buckling (at low relative densities) and high sensitivity to imperfection (waviness of the strut and non-ideal strut cross section) during fabrication of these structures also contribute to the reduction of strength [10,19] . Adding fillets to the nodes efficiently reduces these stress concentrations, enhancing the strength of hollow-strut lattices. Increasing node-smoothening gradually converts hollow-strut lattices to shell-based cellular materials [20].

1.2.3 Shell-based topology

Shell-based cellular materials can be classified in closed-cell and open-cell materials, based on the connectivity of their porosity. The former include closed-cell stochastic foams [9] and 3D periodic arrangements of polygonal cells, e.g octet and cubic-octet regular foams [21]. While some of these materials are remarkably efficient (e.g., the nearly-isotropic cubic-octet regular foam approaches the theoretical Hashin-Shtrikman stiffness bounds [21]), their topology still results in stress localization near face edges and vertices, and hence sub-optimal material utilization. By contrast, open-cell shell-based materials can be constructed as a thin, smooth, interconnected membrane that occupies a 3D volume, with interconnected porosity. These topologies usually take the form of a locally area-minimized geometry [22], and are characterized by a mean curvature (the average of the principal curvatures) approximately equal to zero everywhere on the surface. The most famous examples are triply periodic minimal surfaces (TPMS), such as the Schwarz P surface [23,24], the Schwarz D surface [23,24] and the gyroid surface [25]. The uniform curvature of these surfaces has

been numerically shown to dramatically reduce local stress intensification upon macroscopic loading [26]. Furthermore, Schwarz P shell and Schwarz D shell materials were shown to be stretching-dominated, with E and σ_y on par with or better than most of the existing lattice architectures [20,27,28]. Unfortunately, all these thin shell materials are significantly imperfection sensitive, as any surface roughness or waviness due to manufacturing imperfections would cause them to buckle prematurely under compression [27,29].

1.2.4 Advantages of nanoscale architectures and associated scalability issues

Both the strut-based and shell-based topologies discussed thus far are generally difficult to fabricate in a scalable manner with the smallest feature size at the nanometer scale and overall sample size in the centimeter range (inverse opal and gyroid materials can be fabricated at the nanoscale, but upscaling is challenging). The development of architected materials that can be fabricated at macroscale dimensions while still retaining dimensional control of their nano/micro-scale features is a very active research endeavor. The driving force has been the quest for scale-up of the well-known beneficial size effects on strength that metallic and ceramic materials exhibit when one or more component dimensions are reduced to the nanoscale. Excellent performance has been demonstrated in solid ceramic nanolattices (Bauer et al., 2016), hollow metallic [11,31] and ceramic [12] micro and nano-lattices and nano-shell-based cellular materials [32,33]. The practical applicability of all these nano-architected materials, though, is dramatically hindered by scalability challenges that derive from their manufacturing process [15,34]. Approaches based on self-assembly, possibly combined with additive manufacturing at a larger scale, have the potential to

dramatically increase scalability. In this thesis, we will investigate architected materials with spinodal topologies, which can be fabricated by spinodal decomposition of a solution followed material conversion approaches; this material could provide the ideal combination of topological control of the micro/nanoscale architecture and scalable fabrication.

1.3 Architected materials for bone implants

1.3.1 The need for bone implants

Defects in bones can happen due to diseases (e.g., cancer), accidental damages (trauma or injuries) and surgeries (e.g., tumor resection, revision surgery) [35,36]. If the defects are small, the bone can self-heal through remodeling [37,38], via the process of mature bone resorption by osteoclasts followed by new bone generation by osteoblasts [39–42]. For large-scale bone defects (mostly bone fractures), complete self-healing by the body is not possible [43,44], and implants are often required to fixate and realign the bones for proper healing [45].

1.3.2 Requirements for bone implants

For these implants to be safe and effective in facilitating bone growth, they must be biocompatible with the tissues surrounding the bone defects. More specifically, the implants must be porous to allow efficient transport of nutrients and removal of waste and promote bone ingrowth (which is controlled by the surface area and permeability of the implant) [46–50]; they must have sufficient strength to support daily physical loadings and minimize the occurrence of fatigue failure (which is governed by the peak stress experienced in the implant) [47,51]; and they should have similar stiffness (characterized by the effective

Young's modulus of the implant) to the host bones, to prevent bone loss due to post-surgery stress shielding [47,52–54]. Designing and fabricating architected materials to meet these objectives is a significant challenge.

1.3.3 Categories of bone implants

The most biocompatible choice of implants is autograft (derived from a patient's own tissue), followed by allograft (derived from tissue harvested from another person). However, autograft requires additional surgical sites, with potential associated complications such as hematoma, whereas allograft increases the risk of infection and potential host rejection [55]. Additionally, due to their limited availability, they are not a suitable option for large bone fractures. As a synthetic alternative, one can choose biomimetic implants (i.e., implants that derive their design inspiration from natural bone), with porous metallic implants as the most prominent examples. Metallic cellular materials — made of either non-degradable metals, such as pure titanium, titanium alloys, cobalt alloys, and stainless steels [56–59], or degradable metals, such as magnesium, iron and zinc [60–62] — have been used for a long time in orthopedic applications [63,64], thanks to their combination of high mechanical strength, corrosion resistance and biocompatibility [65,66]. By careful introduction of porosity (φ), the stiffness of cellular materials can be fine-tuned to match that of patients' bones. As a critical added benefit, the porous environment resembles the physiological bone, and evokes a healing response similar to that of bone graft [67]. All these features make porous metallic implants ideal candidates for long bones (stiffest, strongest, load-bearing bones in the body), as illustrated in Fig. 1.1.

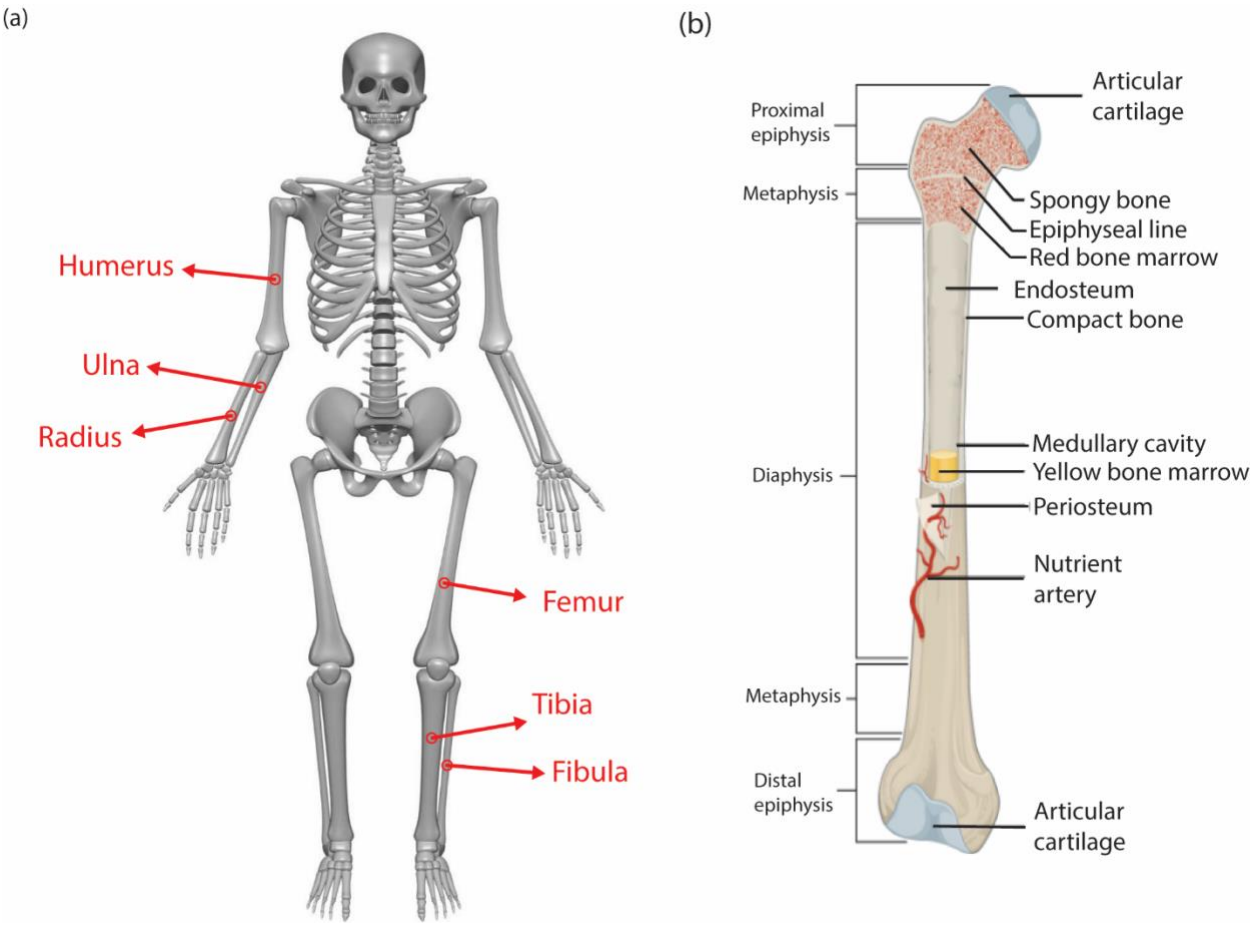

Fig. 1.1 *(a) Long bones (indicated in red hollow circles): femur, tibia, fibula, radius, ulna, and humerus in human skeleton [68,69] and (b) Anatomy of a long bone [69] for illustration purposes.*

1.3.4 Topological design and fabrication of porous metallic implants

Cellular materials, i.e. porous solids consisting of a (generally) periodic repetition of an optimally designed unit cell, have been extensively investigated over the past couple of decades: topology optimization of the unit cell provides a unique opportunity to tailor the effective properties of the material to maximize multifunctional performance for a wide range of applications. In the case of implants, the porosity φ and its topological arrangement (i.e., the unit cell design) can be designed to optimize bone growth, by matching the stiffness of the surrounding bone while providing constant mechanical stimulation to evolving tissue

in the pores, maximizing surface area for bone/implant adhesion [70,71] and maximizing fluid transport [48,72] through the pores, and to minimize stress intensification for optimal fatigue life [73,74]. With the advancement of metal additive manufacturing technologies, in particular selective laser melting (SLM) and electron beam melting (EBM), it is now possible to accurately and cost-effectively fabricate porous metallic implants made of unit cells with nearly arbitrary topological complexity [75–80].

1.3.5 State-of-the-art implant topologies

Currently, the most widely used unit cell topologies for implants are strut-based designs, such as cubic, diamond, and octet lattices [47,80–84]. This is because the mechanical properties of various beam-based topologies are well documented from the past studies and can be accurately predicted by well-established design principles [3,5,9]. Despite their popularity, though, beam-based implant topologies have the following shortcomings: (1) the substantial peak stresses, localized at beam-connecting nodes, often result in the short fatigue life [85–87]; (2) the sharp change in local geometrical environment is anti-biomorphic and creates an adverse environment for homogeneous cell migration [26,88,89].

Shell-based unit cell topologies, characterized by very uniform near-zero mean curvature and the lack of any defined nodes, can address both shortcomings. The most notable examples of these shell-based topologies are triply periodic minimal surfaces (TPMSs), such as Schwarz P (primitive) and Schwarz G (gyroid) surfaces [90]. Over the past few years, TPMSs have received significant attention and have been investigated for their multifunctional performance in multiple fields [91–93]. For bone implant applications,

TPMSs are rapidly becoming topologies of choice, thanks to their uniform curvature, high specific surface area, high strength, high permeability, and topological similarity to human trabecular bones [94–96].

1.4 Approaches to obtain fracture toughness of architected cellular materials

1.4.1 Fracture toughness of cellular materials

The optimal design of the architecture to achieve maximum stiffness and strength has been extensively investigated over the past two decades, both numerically and experimentally. While a number of efficient designs have been identified, both properties are limited by theoretical bounds: for any cellular material, the relative Young's modulus, $\bar{E} = E/E_s$ and the relative yield strength, $\bar{\sigma}_y = \sigma_y/\sigma_{ys}$ (with the subscript s denoting the properties of the constituent materials) cannot exceed the relative density of the material, $\bar{\rho} = \rho/\rho_s$ (Voigt bound). In the case of isotropic cellular materials, much tighter bounds exist, namely the Hashin-Shtrikman bound [97] and the Suquet-Ponte-Castaneda nonlinear bound [98,99], respectively. Conversely, the fracture toughness of cellular materials is theoretically unbounded, and has been much less investigated.

1.4.2 Dimensional analysis

The first systematic investigation dates back to 1984, when Maiti, Gibson, and Ashby derived the analytical expressions of mode I fracture toughness, K_{Ic}, for both open and closed-cell brittle isotropic foams, by using dimensional analysis that relates the global stress intensity factor, K, to the local microscopic stress in the cell wall [100]; fracture occurs ($K = K_c$) when the maximum stress in the cell wall around the crack tip reaches the tensile

strength, σ_{TS}, of the constituent material. K_{IC} of open and closed-cell isotropic foams is found to scale with $\bar{\rho}^{1.5}$ and $\bar{\rho}^{2}$, respectively [100]. Later, Gibson and Ashby showed that the K_{IC} of 2D elastic brittle hexagonal lattices scales with $\bar{\rho}^{2}$ [9]. Huang and Lin used the same approach to obtain analytical expressions for mode II fracture toughness, K_{IIC}, and mixed mode fracture toughness for both 2D hexagonal lattices and 3D elastic brittle isotropic foams [101]. These models predict that for all cellular materials, the initial fracture toughness can be expressed as $K_{IC} = D\ \sigma_{\mathrm{TS}} \sqrt{\ell}\ \bar{\rho}^{d}$, with ℓ, the unit cell size, and d and D, non-dimensional parameters that depend on the topology. While the exponent d can be derived from analytical considerations, the pre-factor D is in general extracted by numerical simulations or experiments.

1.4.3 Continuum Cosserat theory

Alternatively, one can evaluate the fracture toughness analytically using a enriched continuum Cosserat (micropolar) theory; the continuum model is developed by equating its strain energy to that of discrete lattices, in analogy with strain gradient theories [102–104]. The first applications of the enriched continuum theory to lattice structures were proposed by Banks and Sokolowski [105] and Bazant and Christensen [106] . Using this method, Chen *et al*. obtained the expressions of K_{IC} for 2D triangular, square, and hexagonal lattices, predicting the exponent value d = 1 [107]. Such prediction for hexagonal lattices is in disagreement with d = 2 obtained previously by dimensional analysis and experiment data [9]; this discrepancy is attributed to the assumption of affine deformation (stretching) implicit in the Cosserat medium calculations, which ignores cell wall bending [108]. As an additional limitation, enriched continuum techniques, as all techniques utilizing

homogenization, lack the ability to capture local instabilities in the individual struts of discrete lattices, such as those induced by elastic buckling [109].

1.4.4 Finite element modeling on the single-edge-notched-bend and center-cracked plate

Several numerical techniques, based on the Finite Elements method, have been introduced to calculate the fracture toughness of cellular materials (including the pre-factor *D*). Discrete lattices are modeled in configurations with known relations of stress intensity factor to remote boundary conditions such as single edge notched bend (SENB) or center-cracked plate specimens, and treated as a framework of rigid-jointed interconnected beams; the stresses in individual beams as a function of the remotely applied loads are then calculated using the finite element method and the fracture toughness is obtained under the same linear elastic fracture mechanics (LEFM) assumption implicit in the analytical derivations of Gibson and Ashby [9] and Maiti *et al.* [100]. Under these assumptions, accurate estimation of fracture toughness requires that the global K-field be sufficiently larger than the local microscopic cell size. The implication is that in the case of cellular materials, the characteristic size of the overall sample, *L*, must be much larger than the crack length, a, which in turn must be much larger than the unit cell size, ℓ. Huang and Gibson investigated 2D elastic brittle diamond lattices and showed that a/ℓ must be larger than 7 [110]. Quintana and Fleck demonstrated the existence of a transitional crack size, $\boldsymbol{a_T}$, such that below it no K-field exists (strength-controlled failure) and above it failure is well predicted by LEFM (toughness-controlled failure). It was shown that $a_T = 0.9(\ell^2/t)$ for single edge notched bend (SENB) specimens and $a_T = 0.14(\ell^3/t^2)$ for a center-cracked plate subjected to uniaxial tension, with t the in-plane thickness of a bar [111,112]. The

implication is that for $\bar{\rho} < 16\%$, smaller SENB specimens suffice as a fracture toughness testing method. These a_T values also explained the contradictory results between center-cracked plate specimens and SENB specimen of the same 2D lattice found by Huang and Chiang [113].

1.4.5 Boundary layer analysis

As an alternative to center-cracked plate and SENB specimens, the fracture toughness of 2D lattices can also be obtained via boundary layer analysis. In the simplest term, boundary layer analysis relates the local maximum stress around the macroscopic crack tip to the global asymptotic K-field of a crack [114,115] in an equivalent homogeneous medium with effective elastic properties, and K-corresponding displacements and rotations are prescribed onto the outer periphery of the finite element mesh. This technique was first applied by Schmidt and Fleck [116] to gain insights of fracture toughness of regular and irregular elasto-plastic hexagonal lattices. However, extensive usage of such technique is on the study of elastic brittle materials. For example, Fleck and Qiu [108] applied this technique to extract the fracture behaviors of 2D isotropic brittle elastic kagome, triangular, and hexagonal lattices, and demonstrated that K_{IC} scales as $\bar{\rho}^{0.5}$ for kagome lattices, as $\bar{\rho}^{1}$ for triangular lattices, and as $\bar{\rho}^{2}$ for hexagonal lattices. The superior fracture behavior of kagome lattices was attributed to a reduced stress level around the crack tip due to elastic crack tip blunting [1]. Subsequently, Romijn and Fleck applied the same technique with orthotropic K-field boundary conditions to show that K_{IC} of both square and diamond lattices scale as $\bar{\rho}^{1}$ [117,118]. Finally, Christodoulou *et al.* used a similar technique to investigate the effect of cell regularity on the fracture toughness of 2D hexagonal lattices [119]; they found that mode

I fracture toughness is more sensitive to topological variations than mode II in the vicinity of the crack tip.

The boundary layer analysis can also be used to investigate the crack initiation and crack propagation of elastoplastic 2D lattices [116]. Under the conditions of small yielding, Schmidt and Fleck applied the displacement boundary conditions corresponding to a K_I field to hexagonal lattices and assumed that the constituent material follows a bilinear hardening law until one of the beams near the crack tip attains the fracture strength, σ_f. The beam is then gradually removed while the magnitude of the applied K field is increased during the process, such that the work of fracture at the failed joint equals the prescribed fracture energy of the beam. Such requirement of adjusting the applied K field so as to match the prescribed value of fracture energy in a beam disallows the simulation of simultaneous failures of multiple beams. The initial fracture toughness of hexagonal lattices was shown to scale as $\bar{\rho}^2$ and the subsequent R-curves were extracted in both regular and irregular topologies [116]. More recently, Tankasala, Deshpande and Fleck [120] extracted the initial fracture toughness of elastoplastic 2D lattices (triangular, kagome, diamond, and hexagonal) by combining the boundary layer analysis with two sets of failure criteria: (i) maximum local tensile strain and (ii) average tensile strain. They showed that the predicted fracture toughness is only sensitive to the choice of failure criterion for hexagonal lattices (which are bending-dominated) but not for triangular and kagome lattices (which are stretching-dominated). The initial fracture toughness of elasto-plastic 2D lattices was shown to scale with the relative density with the same power laws as for elastic brittle materials [120].

1.5 Problem statement and research objectives

Additive manufacturing technologies have vastly improved over the past decade, in terms of resolution, printing speed, material palette and many other aspects. Notably, we can now additively manufacture artifacts and architected materials with nearly any complex topology in an efficient and cost-effective manner, for relatively large scale engineering applications (with features from hundred microns to few centimeters in size). This allows many architected materials with optimized unit cells topologies designed and studied over the years to be employed in real products in our daily life (for example, architected materials are used in shoe soles and bone implants). However, upscaling of architected materials (to further exploit nanoscale size effect and increase surface area), where the smallest feature size is of the order of hundreds of nanometers and the overall sample size is at the 10-100 centimeter scale, remains a great challenge. A potential solution for the scalable fabrication of nanoarchitected materials is to adopt self-assembly techniques to rapidly generate materials with billions of unit cells of semi-controlled desirable topologies. One such approach utilizes spinodal decomposition of a solution, resulting in a two-phase material with spinodal topology, followed by suitable materials conversion tecniques. While this approach is certainly scalable and can produce shell-based macroscale architected materials with shell thickness at the micro/nanoscale, the resulting topology is intrinsically stochastic. As two decades of research in the field of architected materials have consistently shown that stochastic topologies are less mechanically efficient than periodic designs, before much effort is spent in developing and perfecting scalable manufacturing techniques for architected materials with spinodal topologies, a thorough investigation of the mechanical performance of these topologies is warranted. Such an investigation is provided in this

thesis. Furthermore, the possibility to scalably fabricate shell-based architected materials with porosity at the microscale and exceptionally large surface area per unit volume suggests that these materials might be excellent candidates for bone implant applications. Here we will compare the performance of these materials with that of other state-of-the-art architected materials, in terms of a combination of properties that relate to bone implant performance. Finally, although strength is increased by exploiting size effects in micro/nanoarchitected materials, the fracture toughness decreases with the square root of the unit cell size. This worrisome trend could be somewhat compensated by a possible toughening effect provided by the nature of spinodal-shell topologies, which could deflect propagating cracks. Hence, it is instructive for us to investigate the fracture toughness of architected materials with spinodal shell topologies. Due to the lack of versatile approaches to obtain the fracture toughness/R-curve of architected cellular materials in 2D or 3D, in this work we develop a new numerical approach to address this issue.

In the subsequent three chapters, we will address the issues mentioned above by presenting and discussing the results from our studies as follows:

- *Chapter 2 – The mechanics of architected materials with spinodal topologies.* We investigate the topological characteristics, stiffness, strength, and imperfection sensitivity of architected materials with spinodal topologies and compare them to other state-of-the-art strut-based and shell-based topologies.
- *Chapter 3 – Architected implant designs for long bones: The advantage of minimal surface-based topologies*. We investigate the suitability of architected materials with spinodal shell topology as bone implants and compare their mechanical and bio-

mechanical performance to that of octet lattice (strut-based) and primitive shell (shell-based) architected materials.

- *Chapter 4 – A versatile numerical approach to obtain fracture toughness/R-curve of cellular materials*. We develop a versatile numerical approach to obtain the fracture toughness/R-curves of cellular materials, applicable to 2D or 3D topologies and elastic-brittle or elastoplastic constituent materials.

CHAPTER 2

The mechanics of architected materials with spinodal topologies

(the work in this chapter has been published before in doi:10.1016/J.JMPS.2019.01.002)

2.1 Introduction

Spinodal decomposition is a near-instantaneous diffusion-driven phase transformation that converts a single-phase material into a two-phase material (one possibly being void space), with the two phases arranged in a bi-continuous (both phases are interpenetrating and physically continuous) topology and separated by a surface with nearly uniform negative Gaussian curvature (the product of the principal curvatures) and nearly zero mean curvature (the average of the principal curvatures) [121,122]. Spinodal decomposition may occur by a variety of physical processes, e.g., the dealloying of an Au/Ag solid solution[123] or the heating/cooling of an emulsion gel through a critical point [124]. The former results in a gold solid spinodal structure with ~50% porosity and nanoscale feature size (Fig. 2.1a), whereas the latter gives rise to a ~50%/50% mixture of two liquids with microscale feature size, called a bicontinuous interfacially jammed emulsion gel (bijels) (Fig. 2.1b). While thermodynamics favors the growth of the feature size over time, this process can be arrested (thereby controlling the length scale), by lowering the temperature (in the case of nano-porous metal) or by jamming the interface with solid nano-particles (in the case of bijels). Bijels can be used as templates for the development of structural and functional micro-architected materials, via a suite of materials conversion processes [125,126]. For example, one of the liquid phases can be replaced by a photosensitive monomer, which is subsequently photopolymerized, and the other liquid phase removed,

resulting in a ~50% dense polymeric cellular spinodal architecture. The surface of this cellular solid can be subsequently coated with metal or ceramic, and the polymer ultimately dissolved, with the end result being a stochastic shell-based architected material with spinodal topology [124] (Fig. 2.1c). This process is extremely scalable and can result in rapid fabrication of macro-scale shell-based cellular materials with microscale feature size. The stochastic nature of this shell-based architecture, though, raises questions about its mechanical efficiency.

In this chapter, we thoroughly investigate the mechanical response (stiffness and strength) of both solid and shell-based architected materials with spinodal topologies. We numerically generate 3D spinodal cellular materials with different relative densities and characteristic feature sizes and extract shell-based spinodal cellular materials from the interface between the solid and the void space. We compute stiffness and strength under uniaxial compression by finite element simulations, which are verified by mechanical experiments conducted on polymeric samples produced by 2-photon polymerization Direct Laser Writing.

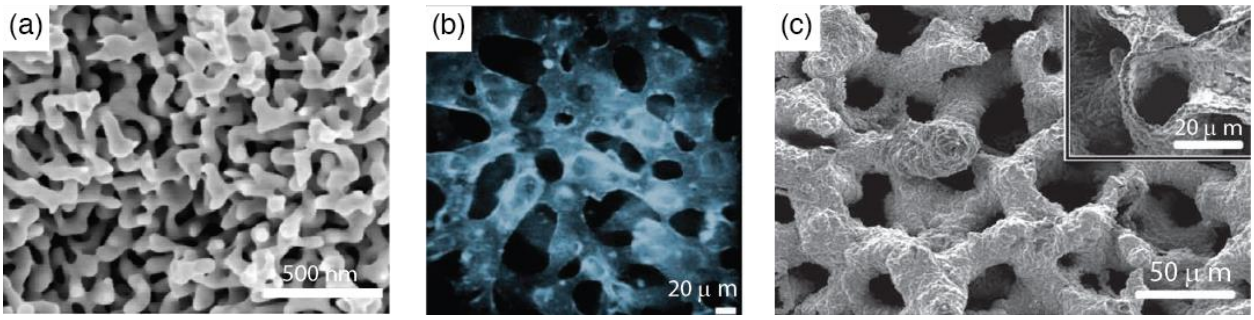

Fig. 2.1 *Examples of self-assembled spinodal topologies at different length scales: (a) nano-porous Au, obtained by selective etching of Au/Ag solid solutions (reproduced from [123]); (b) spinodally decomposed bijel (reproduced from [124]); (c) micro-porous metallic shell spinodal architected material, obtained by material conversion of spinodally decomposed bijels (reproduced from [124]).*

2.2 Numerical construction of spinodal topologies

2.2.1 Generation of solid spinodal topologies

Spinodal structures are formed through spinodal decomposition, a diffusion-type phase separation process that separates a compound into a mechanical mixture of phase A and phase B solid solutions by reducing the total free energy of the system [127]. The phase separation processes during spinodal decomposition can numerically be described with phase field approaches [128–130]. One of the most commonly used formulations is the Cahn-Hilliard equation [131,132], which can be written as:

$$\frac{\partial u}{\partial t} = \Delta\left(\frac{df(u)}{du} - \theta^2 \Delta u\right) \tag{2-1}$$

where $u(x, y, z, t)$, is the concentration difference between the two phases (phase A and phase B) at a coordinate *(x,y,z)* at the evolution time, t ($u(x, y, z, t)$ is bounded between -1 and 1, with $u = -1$ denoting full phase A and $u = 1$ denoting full phase B), and Δ is the Laplacian operator. At time $t = 0$, the system is nearly homogeneous, with $u \sim 0$ everywhere. As the simulation starts, phase separation is driven by a free-energy function with a double well, which can be chosen as $f(u) = \frac{1}{4}(u^2 - 1)^2$. Regions of phase A and phase B quickly develop, with θ denoting the width of the interface between the two phases (here set to 1.1, as suggested by [132]). As time progresses the size of the single-region domains increases and the curvature of the interface decreases. For a cellular material, one of the two phases represents void space. This equation is discretized by the Finite Difference method and solved on a cubic domain of 100 × 100 × 100 nodes, subject to periodic boundary conditions. The solution procedure is nearly identical to that reported in [132]; a synopsis is reported in Appendix A for completeness. Solid spinodal volumes at 5 different evolution times, $t_1 - t_5$ (and hence different domain sizes and surface curvatures) and 4 different

relative densities, $\bar{\rho}_1 = 20\%$, $\bar{\rho}_2 = 30\%$, $\bar{\rho}_3 = 50\%$ and $\bar{\rho}_4 = 70\%$, are extracted for post-processing (Fig. 2.2). Spinodal volumes were subsequently sliced in 2D images and the stack of images was imported in the commercial software Simpleware ScanIP to generate a 3D tetrahedral finite element mesh for subsequent mechanical characterization.

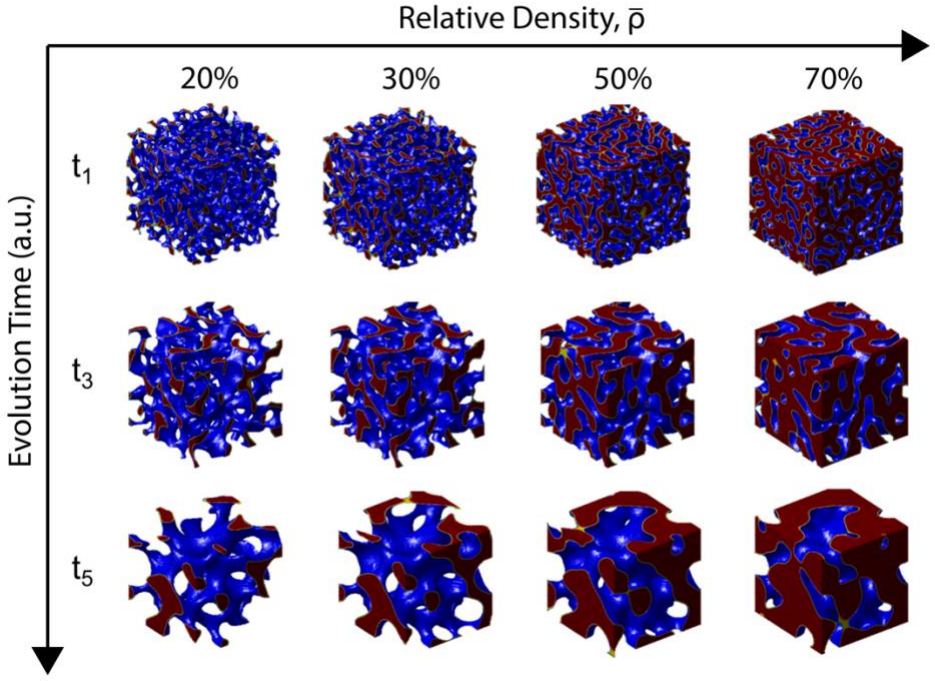

Fig. 2.2 *3D spinodal solid models with different relative densities,* $\bar{\rho} = 0.2, 0.3, 0.5, and\ 0.7$, *extracted at different evolution times,* t_1, t_3, *and* t_5.

2.2.2 Calculation of the characteristic feature size

Whereas periodic architected materials have a very well-defined unit cell size, for stochastic spinodal solid this definition is fuzzier. Nonetheless, a measure of the *characteristic feature size,* λ, is necessary to enable comparison with periodic cellular materials. This dimension can be defined as the inverse of the dominant frequency in a Fast Fourier Transform (FFT) of the spinodal model [133,134]. To graphically illustrate the relationships between real domain and frequency domain, FFTs are initially extracted on

two-dimensional slices of the solid spinodal topologies (Fig. 2.3). The results show three important features: (i) the intensity profiles in the FFT images are all nearly axisymmetric, indicating that all our spinodal models are isotropic; (ii) the dominant frequencies shrink as the evolution time increases, indicating that the characteristic feature size increases with evolution time; (iii) the dominant feature size is unaffected by the relative density of the solid spinodal models and only depends on evolution time, suggesting that this unique characteristic length scale can be used to uniquely describe the morphology evolution of the system (*in lieu* of time), a description that we adopt henceforth for both solid and shell spinodal topologies.

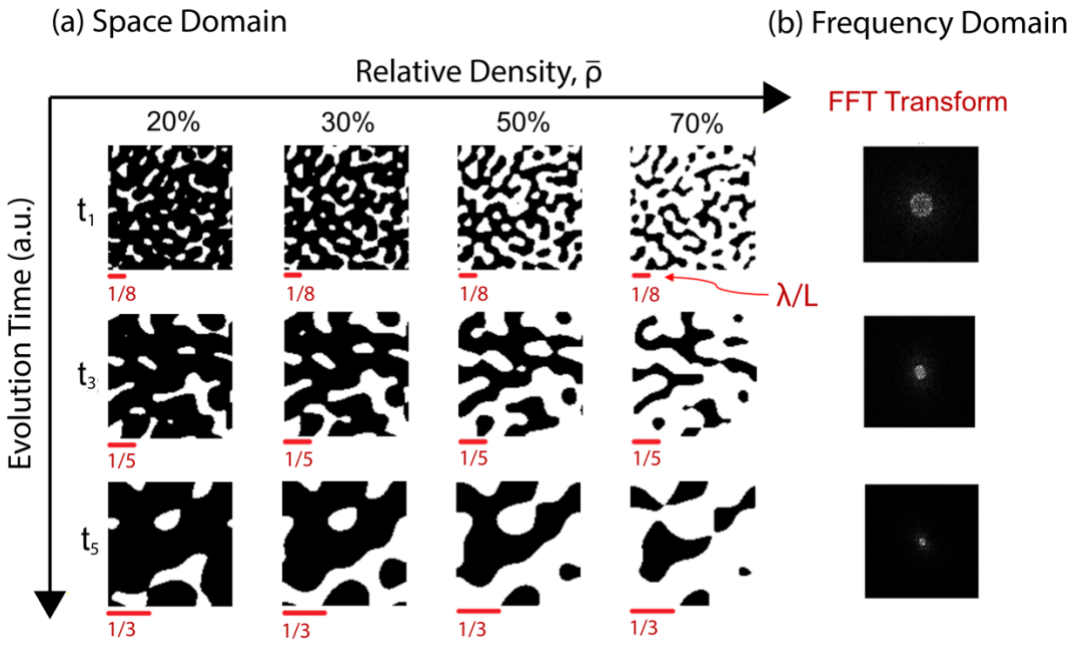

Fig. 2.3 *2D slices of spinodal solid models in (a) space domain and (b) frequency domain, at different relative densities ($\bar{\rho} = 0.2, 0.3, 0.5, and\ 0.7$) and different evolution times (t_1, t_3, and t_5). The characteristic feature size is extracted from the FFT transforms of the models, and depends on the evolution time, but not on the relative density.*

To properly measure the characteristic feature size for each topology, FFTs are extracted for full three-dimensional spinodal models. Plots of amplitude VS frequency along

the x-direction are extracted and depicted in Fig. 2.4a (the specific direction is immaterial, as the models were shown to be isotropic). Notice that the frequency has been multiplied by the domain size L in Fig. 2.4a; with this normalization, the x-position of the dominant frequency peak represents the number of unit cells in the domain, $N = L/\lambda$, with λ the characteristic feature size.

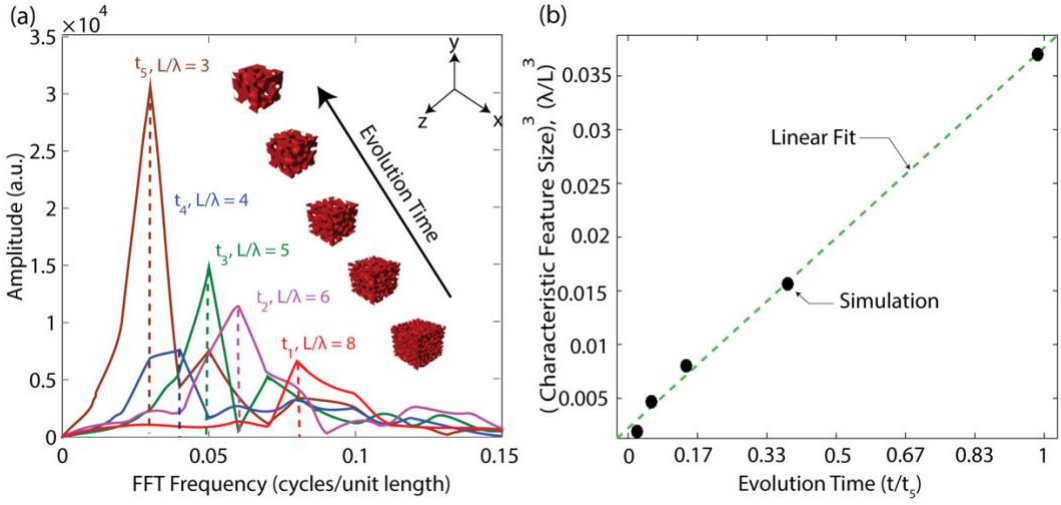

Fig. 2.4 *Time evolution of the inverse of the characteristic feature size, as extracted from 3D FFT analyses of solid spinodal models. (a) FFT amplitude along the x direction at five evolution times; the frequency with highest amplitude is the inverse of the characteristic feature size. (b) The characteristic feature size scales with the cubic root of the evolution time (normalized by t_5), as predicted by the LSW theory of spinodal decomposition.*

Fig. 2.4a clearly shows that the characteristic feature size increases with evolution time, as qualitatively observed in the 2D FFTs. This time evolution is explicitly plotted in Fig. 2.4b, where the characteristic feature size is shown to scale with the cubic root of the evolution time, as expected by the LSW (Lifshitz-Slyozov-Wagner) theory of spinodal decomposition [133,135], for all but the first simulation. The slight disagreement on the first simulation point is attributed to an incomplete phase separation in the Cahn-Hillard

evolution model (i.e., evolution is not yet fully completed at that short time, and feature growth had not fully started). This finding confirms that the numerical topologies obtained with the technique described in section 2.2.1 possess the characteristic features of naturally occurring spinodal structures.

2.2.3 Generation of shell spinodal topologies

Spinodal shell geometries are generated by extracting the interface between solid and void phases of spinodal solid models with a three-step process: (i) the stack of 2D images for each model is imported in Matlab and a 3D matrix containing the phase information of any point in the cubic domain at a particular instant in time is generated; (ii) the Matlab 'isosurface' function is used to extract the interface between solid and void phases; (iii) the Matlab 'surface smoothening' algorithm is applied to the isosurface patches, in order to remove sharp geometric transitions. The resulting three-dimensional surface is then meshed with triangular shell elements within Matlab and subsequently imported in the commercial finite element software Abaqus for further mechanical analysis. The relative density of spinodal shell topologies is tuned by controlling the shell thickness in Abaqus. With this procedure, we generate spinodal shell topologies from each of the five solid spinodal topologies with 50% relative density discussed above (each with a different evolution time, and hence domain size and surface curvature); three such topologies are depicted in Fig. 2.5a. Once the surface area per volume ratio, S/V, of each model is extracted, the relative density of the shell spinodal model is calculated as $\bar{\rho} = bS/V$, with b the shell thickness. This relationship is plotted in Fig. 2.5b; notice that the shell thickness has been normalized by the characteristic domain size, λ, defined in section 2.2.2 above. Using this approach, we

generate shell spinodal structures with relative densities, $\bar{\rho} = 0.01\%, 0.1\%, 1\%$, 5%, 7%, and 10% for further analysis.

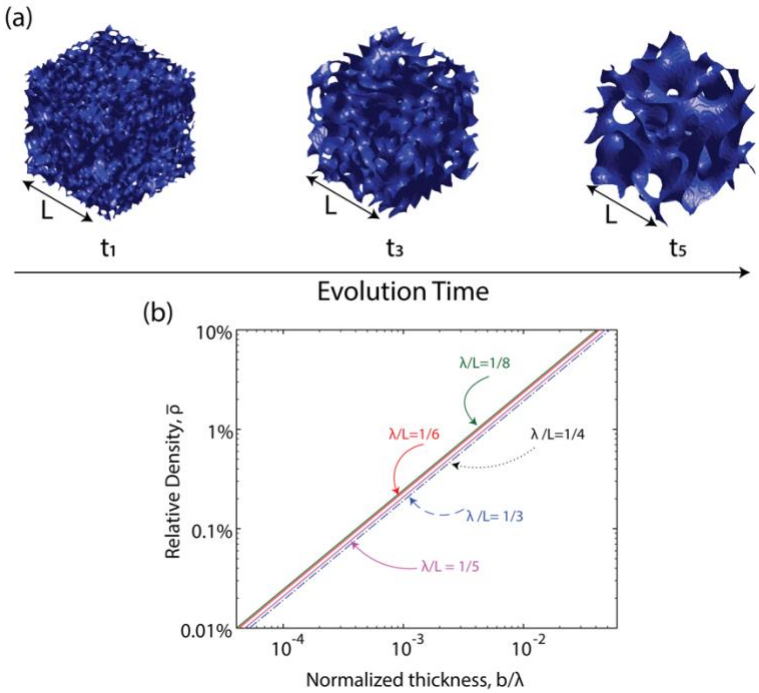

Fig. 2.5 *(a) 3D spinodal shell models corresponding to the interfaces of spinodal solid models of* $\bar{\rho} = 0.5$, *extracted at three different evolution times (t_1, t_3, and t_5). (b) Relative density of shell spinodal cellular materials, as a function of the shell thickness, b, normalized by the characteristic feature size, λ. L denotes the cubic domain size.*

2.2.4 Calculation of the surface curvature

While clearly stochastic in nature, spinodal structures possess a remarkable uniform distribution of surface curvatures, with every surface patch characterized by a near-zero mean curvature and negative Gaussian curvature. Mean and Gaussian curvatures can be expressed in terms of the principal curvatures as $H = \frac{1}{2}(\kappa_1 + \kappa_2)$ and $K = \kappa_1 \cdot \kappa_2$. To confirm that the models generated in sec. 2.21 conform to this important signature of spinodal structures, we extract the principal curvatures at any location in each shell spinodal model with the algorithm described in Appendix B. The results are plotted in Fig. 2.6. A

number of important results clearly emerge: (i) for all topologies derived from 50% dense solid models (i.e., same amount of solid and void phases), $H \sim 0$ and $K < 0$, with most surface points within a very narrow range, as predicted by the theory of spinodal decomposition [133]; henceforth, we will use these models to construct shell spinodal topologies for mechanical characterization; (ii) for topologies derived from solid models with densities lower (higher) than 50%, $H < (>) 0$ and $K < 0$, with most surface points within a very narrow range; (iii) for all topologies, the magnitudes of the principal curvatures decrease with evolution time, remaining consistent with the trends mentioned above; this is clearly consistent with the characteristic feature size coarsening over time, as noticed above.

2.3 Mechanical performance of spinodal topologies

2.3.1 Numerical modeling of mechanical response

The finite element (FE) meshes of the solid and shell spinodal models, generated as described in section 2.2, are imported in the commercial FE software package Abaqus Standard, and static simulations are performed to extract the mechanical response of these cellular materials under uniaxial loading, specifically the effective Young's modulus, E, and the effective yield strength, σ_y. The constituent material is modeled as isotropic elastic-perfectly plastic, with Young's modulus, $E_s = 210\ GPa$ and yield strength, $\sigma_{ys} = 235\ MPa$ (the actual values are immaterial, as the effective properties are normalized by these values). Geometric nonlinearity is allowed during deformation.

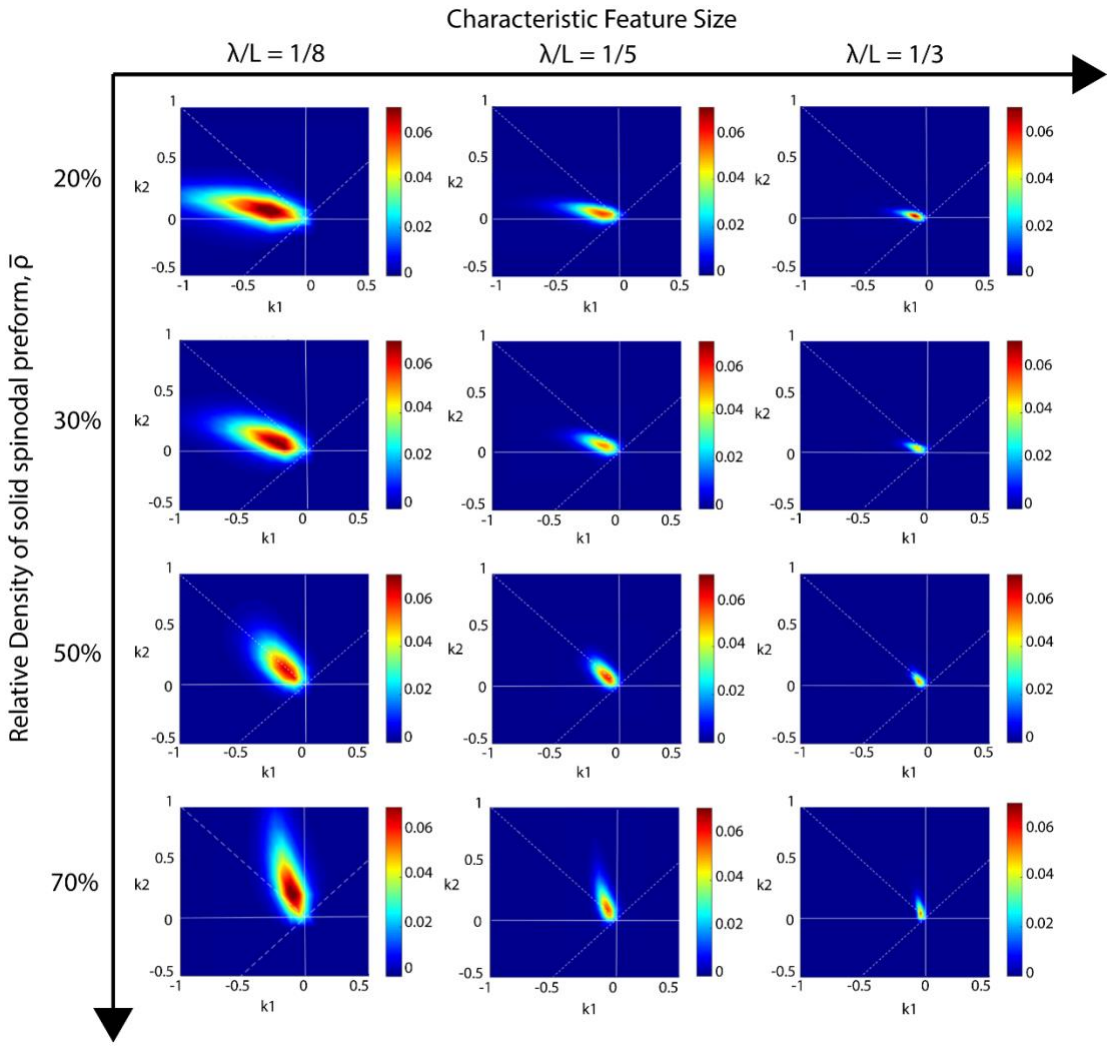

Fig. 2.6 *Principal curvature maps of the surface of shell spinodal models, derived from different relative densities* ($\bar{\rho} = 20\%, 30\%, 50\%, and\ 70\%$) *and different characteristic features sizes (* $\frac{\lambda}{L} = \frac{1}{8}, \frac{1}{5}, and \frac{1}{3}$*) of solid spinodal preforms. Notice that only the 50%-derived shell topology has near-zero mean curvature,* $H = \frac{1}{2}(\kappa_1 + \kappa_2)$*, throughout the surface.*

To simulate the uniaxial response of an infinite solid, the following boundary conditions are applied on the cubic domains (Fig. 2.7): (i) the nodes on the –x face are restrained from moving in the x-direction but allowed to move freely in the y- and z-direction; (ii) a compressive displacement, $\delta_x = -6$, corresponding to a lattice level strain $\varepsilon_x = -6\%$, is applied to all the nodes on the +x face, which are otherwise free to move in the

y- or the z-direction; (iii) all the nodes on the +y face are free to move in all directions, although their y-displacement is coupled to that of a reference node (and hence is the same for all nodes on the face); similarly, all the nodes on the +z face are free to move in all directions, although their z-displacement is coupled to that of a reference node (and hence is the same for all nodes on the face); (iv) the nodes on the –y face are constrained from moving in the y-direction but are free to move in the x- or z-direction, and the nodes on the –z face are constrained from moving in z- direction but are free to move the in x- or y-direction. Although not as rigorous as periodic boundary conditions, these boundary conditions can be applied to nonperiodic cellular materials (in this case spinodal topologies) simulating the mechanical response of infinite cellular structures, ensuring that all plane faces remain plane and allowing for Poisson's contraction upon uniaxial compression.

The reaction force (F_R) integrated on all the nodes on the –x face is extracted through the simulation. The stress-strain curve for the cellular material can then be generated, with stress and strain defined as $\sigma = F_R/L^2$ and $\varepsilon = \frac{\delta_x}{L}$, respectively, with L the cubic domain size. The effective Young's modulus of the cellular material, E, is calculated as the slope of the linear region in the stress-strain curve, and the effective yield strength, σ_y, is extracted as the 0.2% offset strength.

2.3.2 Imperfection sensitivity analysis

Thin shells (and by extension thin shell-based architected materials) are known to be stiff and strong but significantly sensitive to geometric imperfections [29], a characteristic that significantly limits their load carrying potential in practical applications. To quantify this effect in spinodal shell models, an imperfection sensitivity analysis is performed.

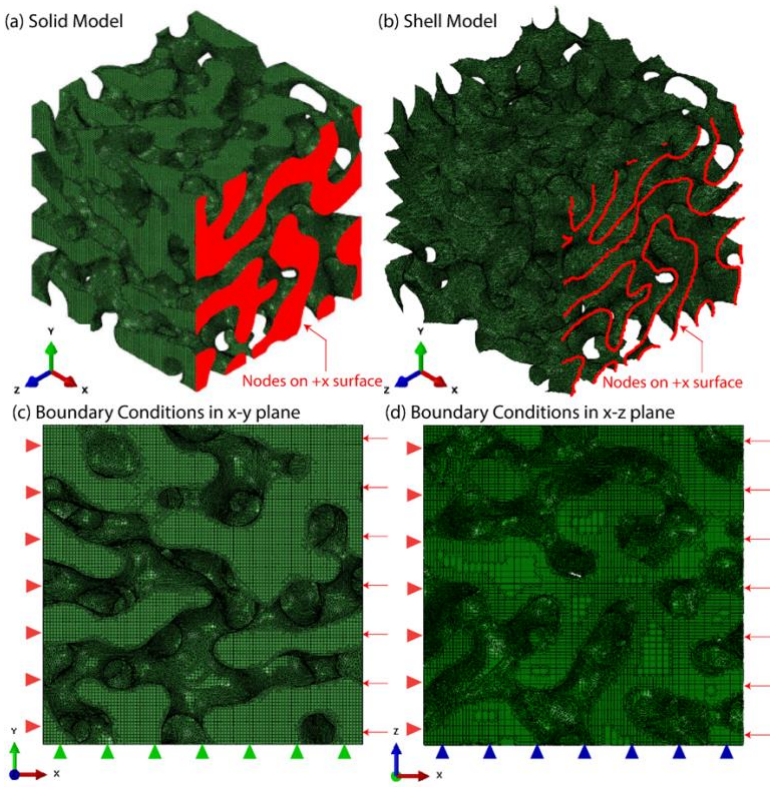

Fig. 2.7 *Finite element model of (a) a solid spinodal model ($\bar{\rho} = 50\%$) and (b) the corresponding shell spinodal model. The nodes on the positive x surface are highlighted in red indicating how the boundary conditions are applied to the models. (c-d) Boundary conditions applied to a spinodal solid model in the x-y and x-z planes. Red, green, and blue triangles indicate that translations are constrained along the x, y, and z directions, respectively. The sides opposite to those indicated with red, green, and blue triangles are allowed to displace in the x, y, and z directions, respectively, but with the condition that all nodes on the side displace by the same amount. The same boundary conditions are applied to spinodal shell models.*

First, linear eigenvalue (elastic buckling) analyses are performed on the original meshes and the first ten eigenmodes with positive eigenvalues are extracted from each mesh. Second, imperfections are introduced in the original meshes as linear combinations of the first ten eigenmodes with equal weights; the magnitude of the imperfection parameter, $\psi = h_{max}/b$, with h_{max} the largest displacement from the original mesh and b the shell thickness, is systematically increased in order to probe the imperfection sensitivity. Finally, post-buckling non-linear quasi-static Ricks analyses are performed in uniaxial compression,

subject to same boundary conditions described above, in order to capture the deformation evolution in imperfect meshes. Fig. 2.8 and 2.9 show meshes and stress-strain curves for two different 10% dense shell spinodal topologies, differing by the size of the characteristic feature, λ, relative to the domain size ((a) $\lambda/L = 1/8$, (b) $\lambda/L = 1/3$). For each topology, the response of the perfect structure ($\psi = 0$) is compared to the responses of the same topology with increasing amounts of imperfection. A very notable conclusion emerges: the topology with 8 X 8 X 8 'unit cells' in the domain (Fig. 2.9a) is absolutely imperfection insensitive, with imperfection magnitudes as large as 20 times the shell thickness showing no effect on the mechanical response. Even for very coarse topologies, with only 3 X 3 X 3 'unit cells' in the domain (Fig. 2.9b), the imperfection sensitivity becomes appreciable only when $\psi \sim 10$. (To further emphasize the imperfection insensitivity of these topologies, notice that the topology with characteristic feature size, $\frac{\lambda}{L} = 1/3$ (Fig. 2.8c-d and Fig. 2.9b) has much smaller surface area per unit volume than the topology with $\frac{\lambda}{L} = 1/8$ (Fig. 2.8a-b and Fig. 2.9a), and hence larger shell thickness; hence, in absolute terms, the imperfection magnitudes displayed in Fig. 2.9b are much larger than those in Fig. 2.9a (as evident from comparing Fig. 2.8a-b with Fig. 2.8c-d), explaining the emergence of some degree of imperfection sensitivity). Overall, the remarkable conclusion is that, unlike regular shell-based architected materials, spinodal shell based architected materials are remarkably imperfection insensitive; this important characteristic is attributed to the stochastic nature of the spinodal shell topologies. With this conclusion, all subsequent finite element analyses are performed on perfect meshed, without loss of conservatism.

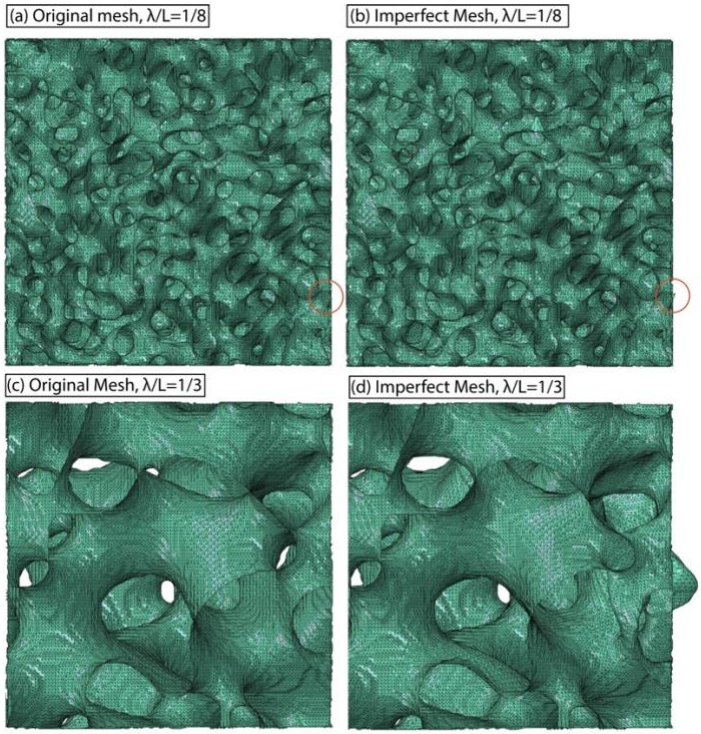

Fig. 2.8 *Comparisons of perfect (a,c) and perturbed (c,d) meshes for spinodal shell topologies with characteristic feature size,* $\frac{\lambda}{L} = \frac{1}{8}$ *(a,b) and* $\frac{\lambda}{L} = \frac{1}{3}$ *(c,d).The magnitude of the imperfection is equal to* $\psi = 20$ *(b) and* $\psi = 9.3$ *(d), respectively. Red circles in (a,b) represent examples of subtle imperfections.*

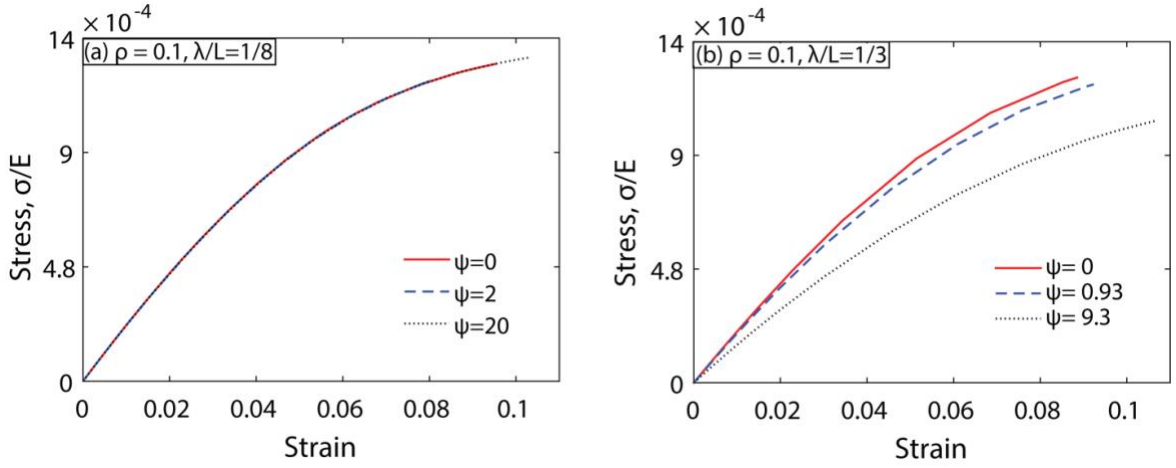

Fig. 2.9 *Imperfection insensitivity of shell spinodal models. The non-dimensional imperfection magnitude,* ψ*, is defined as the largest displacement from a perfect mesh normalized by the shell thickness. Comparison of post-buckling stress-strain curves of 10% dense spinodal shells with characteristic feature size,* $\frac{\lambda}{L} = \frac{1}{8}$ *(a) and for* $\frac{\lambda}{L} = \frac{1}{3}$ *(b), with three different magnitudes of imperfection. The constituent material has Young's modulus,* $E_s = 210\ GPa$ *and yield strength,* $\sigma_{ys} = 235\ MPa$*.*

2.3.3 Experimental verification

The accuracy of the finite element simulations is verified with a selected set of uniaxial compression experiments. Solid and shell spinodal samples were fabricated at the micro-scale via two-photon polymerization Direct Laser Writing (DLW), using a Nanoscribe Photonic Professional GT and a negative tone photoresist (IP-Dip, produced by Nanoscribe GmbH). All samples were fabricated using the Galvo mode with the 63X, N.A. 1.4 objective lens. Printing parameters were 35 mW and 17,000 μm/s for laser power and scan speed, respectively. Cubic samples with edge length, $L = 140\ \mu m$, are generated, using the solid and shell spinodal geometries generated in Section 2.2. A characteristic feature size, $\lambda/L = 1/5$, is used for all samples. Solid spinodal samples with relative densities of 20%, 30% and 50%, and shell spinodal samples with relative densities of 5%, 7% and 10% were fabricated, respectively (all shell spinodal topologies were extracted from a 50% dense solid spinodal, as explained in Section 2.2.3). After DLW, samples were first immersed in propylene glycol monomethyl ether acetate (PGMEA) for 20 minutes to dissolve the remaining liquid resin, and subsequently in isopropanol for 2 minutes for final cleaning. See Fig. S1 for SEM images of all samples.

The mechanical response of all spinodal structures was characterized by displacement-controlled uniaxial compression tests with a maximum strain of 15%, performed at a constant strain rate of $0.005/s$. All tests were performed with an Alemnis Nanoindenter. Load-displacement curves were recorded, extracted, and converted to stress-strain curves as explained in section 2.3.1. To compare experimental results with numerical predictions, finite element models of the same topologies were generated and loaded in uniaxial compression. In order to best approximate the experimental conditions, FE

simulations are performed with the bottom face fully constrained, the lateral faces free and the top face subjected to uniform vertical displacement but unconstrained laterally. In order to extract the constituent material properties for the numerical analyses, a number of IP-Dip cylinders with diameters between 12.5 and 50 μm and aspect ratios of four were DLW printed with the same parameters as the spinodal samples and tested in uniaxial compression (see Supplementary Material Fig. S2) [136]. As the mechanical properties of this DLW acrylate resin are affected by the printing conditions and feature size (which cannot be kept identical for all the structures being printed), extracting an accurate stress-strain curve for the base material is challenging. To simplify the model, and in agreement with the results in Fig. S2, the constituent material was modeled as elastic-perfectly plastic, with Young's modulus, $E_s = 2$ GPa, and yield strength $\sigma_{ys} = 60$ MPa. While this simplification will slightly under-predict the ultimate strength of the structures, it is appropriate for the scope of this section.

Experimental and numerical stress-strain curves are compared in Fig. 2.10a-b, for solid and shell spinodal models, respectively. With the caveat on ultimate strength mentioned above, the agreement is very good throughout, thus validating all the finite element results presented in this work.

2.3.4 Scaling laws and mechanical performance

Effective Young's modulus and yield strength were extracted from finite element calculations (performed as described in section 2.3.1) for solid and shell spinodal models, for a range of relative densities, $\bar{\rho}$ and characteristic feature size, λ/L. In all simulations the constituent material was modeled as isotropic elastic-perfectly plastic, with Young's

modulus, $E_s = 210$ GPa and yield strength, $\sigma_{ys} = 235$ MPa. These values are representative of a relatively low yield strain metal, with yield strain $\varepsilon_y \sim 0.001$. Most results presented here are general and independent on the choice of base material.

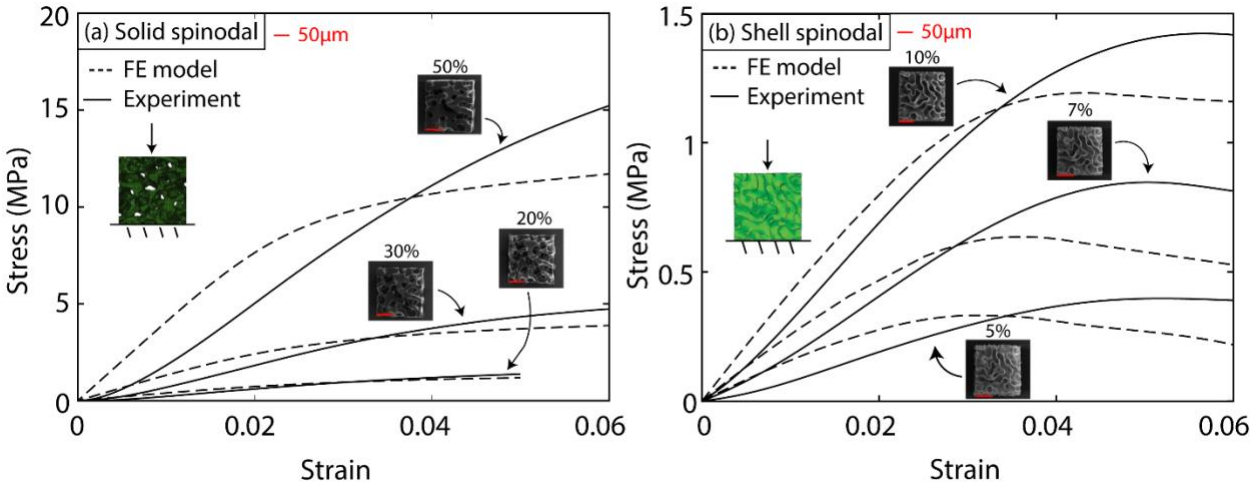

Fig. 2.10 *Comparison of numerical and experimental stress-strain curves for (a) solid and (b) shell spinodal topologies at different relative densities, loaded in uniaxial compression. The characteristic feature size, $\frac{\lambda}{L} = \frac{1}{5}$ is used for all models. The insets depict SEM images of the samples, fabricated by two-photon polymerization Direct Laser Writing in IP-Dip, with a Nanoscribe GT Photonics Professional, and tested with an Alemnis Nanoindenter. Higher resolution SEM images of all samples are shown in Fig. S1. The properties of IP-Dip were measured by micropillar compression tests, and input in the simulations as an elastic-perfectly plastic solid with $E_s = 2$ GPa, and yield strength $\sigma_{ys} = 60$ MPa.*

The effective Young's modulus and yield strength of solid spinodal models depending on $\bar{\rho}$ are depicted in Fig. 2.11. Notice that $E \sim (\bar{\rho})^{2.0-2.6}$ and $\sigma_y \sim (\bar{\rho})^{1.7-2.3}$, with the lower exponents corresponding to topologies with larger characteristic feature size to domain size ratios. We excluded the 20% dense samples from the scaling calculations, as the 20% dense spinodal topologies displayed isolated islands on the inside of the models that depressed the mechanical properties and unrealistically steepened the slopes. While these large exponents are not unexpected at such large relative densities, this likely indicates that the solid spinodal

topologies are bending dominated and the spinodal arrangement of matter is not very mechanically efficient. The numerical simulations indicate that solid spinodal models are yielding-limited (as opposed to elastic buckling-limited) for all relative densities of interest, 20-70%.

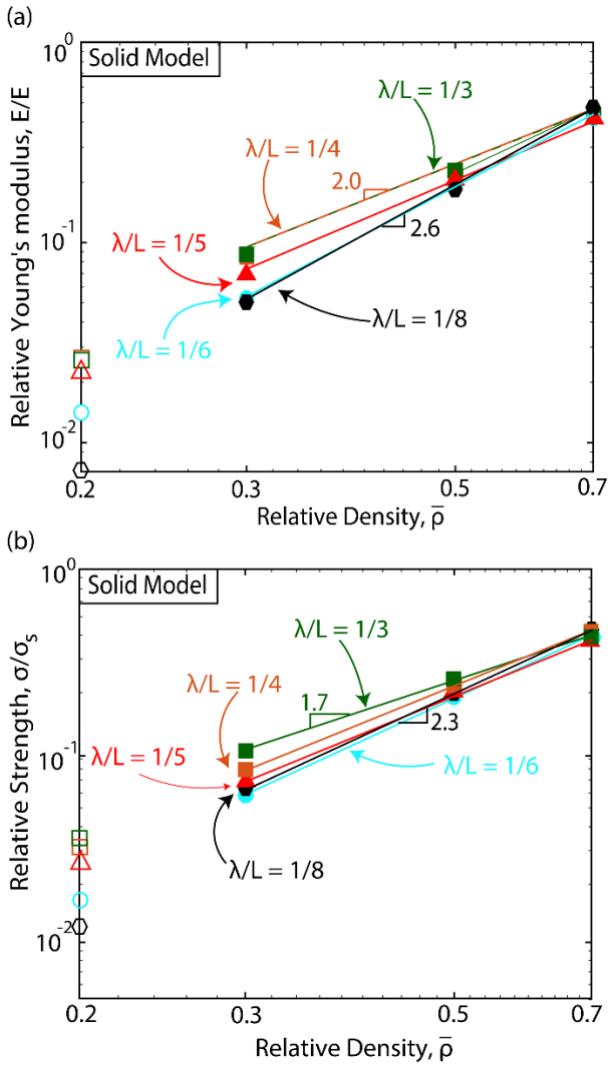

Fig. 2.11 *Numerical predictions of (a) Relative Young's modulus and (b) relative yield strength of spinodal solid models, as a function of their relative density, $\bar{\rho}$. Hollow markers indicate models with isolated internal islands, which have been excluded from the scaling calculations. The constituent material has Young's modulus, $E_s = 210\,GPa$ and yield strength, $\sigma_{ys} = 235\,MPa$. Different curves refer to models with different characteristic feature size, λ. L denotes the domain size.*

Remarkably, these conclusions change dramatically for shell spinodal topologies (Fig. 2.12). Here, $E \sim \sigma_y \sim (\bar{\rho})^{1.2-1.3}$, a scaling that is very similar to that of the best stretching dominated lattice materials. We attribute this exceptional performance to the deformation behavior of doubly curved surfaces, which cannot be readily bent without the introduction of significant membrane stresses – and hence deform in a stretching-dominated manner. For the base material yield strain used in the calculation, shell spinodal topologies remain yielding-limited down to relative densities in the order of 0.1%. Once the failure mechanism switches to buckling, the scaling worsens somewhat (as expected), but remains reasonably close to one. Interestingly, the relationship between scaling law exponent and characteristic feature size to domain size ratio, λ/L, is inverted compared to the case of solid spinodal topologies. In shell spinodal topologies, a larger λ/L corresponds to a steeper scaling exponent for both stiffness and strength.

The exceptional mechanical efficiency of shell spinodal topologies is attributed to its uniform surface curvature (see section 2.2.4), which results in a very uniform local stress distribution upon loading, avoiding areas of substantial stress intensification. To confirm this hypothesis, we contrast the local stress distribution upon uniaxial loading of a shell spinodal sample and a hollow microlattice material of the same relative densities, reproduced from [10] (Fig. 2.13); the difference in Mises stress uniformity is clearly evident. In other words, shell spinodal topologies are extremely efficient in terms of material utilization, with the entire structure yielding (or buckling) nearly simultaneously, rather than localizing failure at the nodes (a well-known shortcoming of hollow lattice materials [10–13,137].

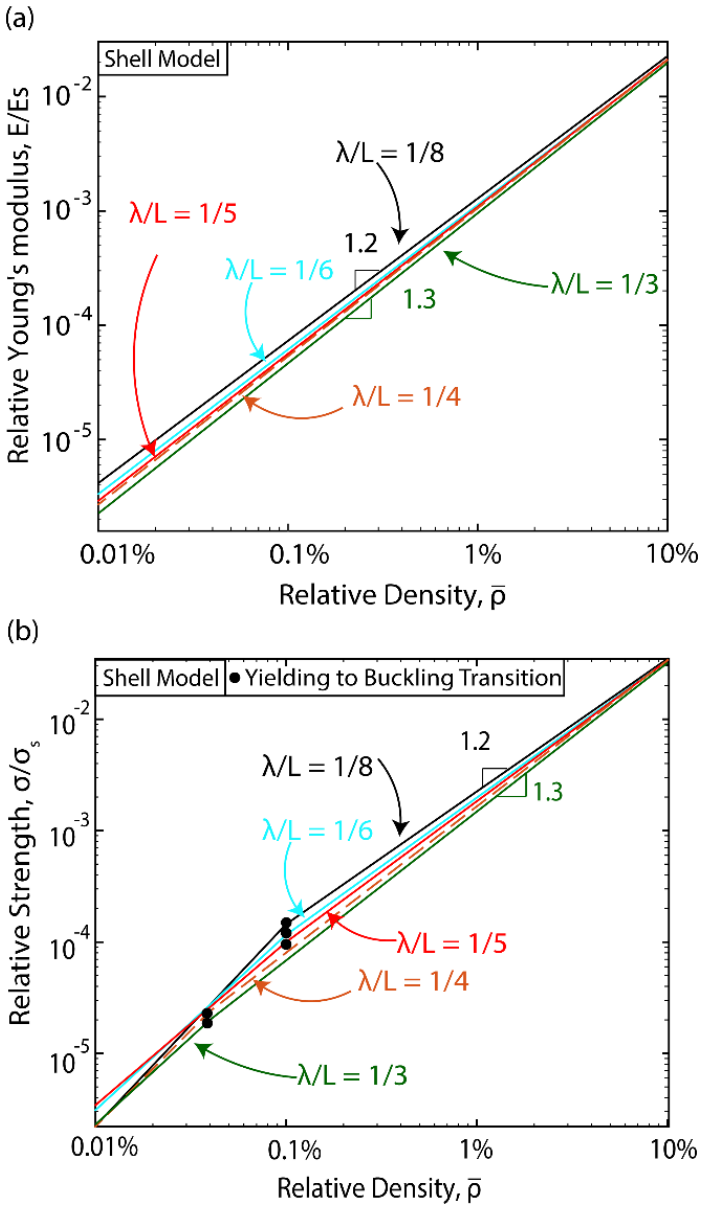

Fig. 2.12 *Numerical predictions of (a) Relative Young's modulus and (b) relative yield strength of spinodal shell models, as a function of their relative density, $\bar{\rho}$. The constituent material has Young's modulus, $E_s = 210\ GPa$ and yield strength, $\sigma_{ys} = 235\ MPa$. Different curves refer to models with different characteristic feature size, λ. L denotes the domain size. The black dots mark the transition from yielding to buckling failure.*

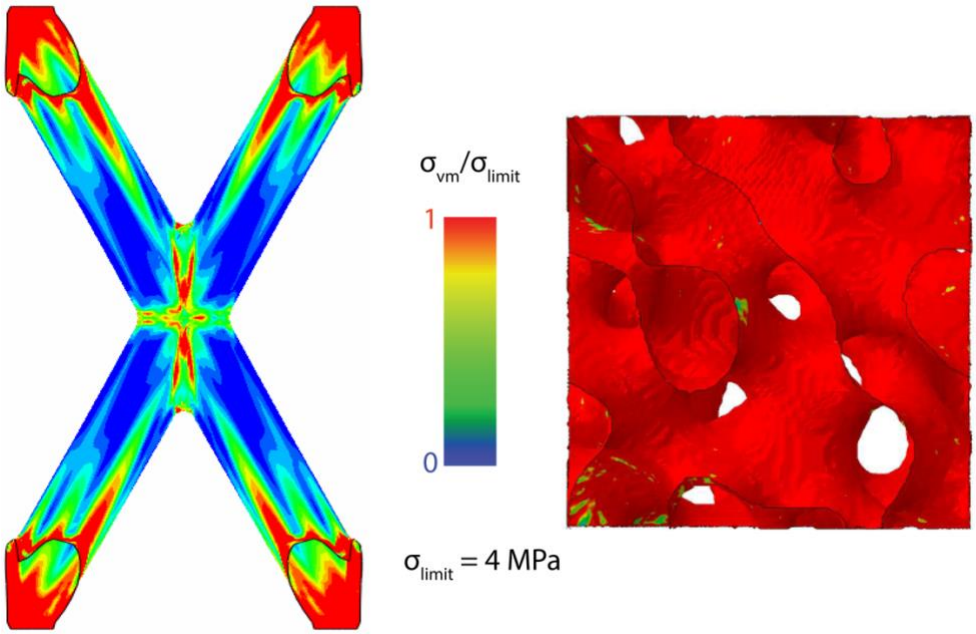

Fig. 2.13 *Comparison of von Mises stress distribution in a hollow microlattice unit cell with bar aspect ratio ~6, and angle* $\theta = 60^{\circ}$ *[10] and a spinodal shell model with characteristic feature size,* $\frac{\lambda}{L} = \frac{1}{3}$*, both at relative density of 0.01%, and under a compressive strain of 0.1%. The constituent material has Young's modulus,* $E_s = 210\ GPa$ *and yield strength,* $\sigma_{ys} = 235\ MPa$*. The stress limits (used to distinguish stress contours where* $\frac{\sigma_{vm}}{\sigma_{limit}} \geq 1$*) are colored "red", with* $\sigma_{limit} = 4\ MPa$*. Notice that the spinodal shell topology has a much more uniform stress distribution, yielding excellent mechanical efficiency.*

An obvious question emerges regarding the role of near-zero mean curvature on the uniformity of the stress distribution and hence the mechanical efficiency of shell spinodal topologies. As clearly illustrated in Fig. 2.6, all 50%-derived spinodal shell topologies possess the characteristics of minimal surfaces (i.e., $\kappa_1 = -\kappa_2$ almost everywhere on the surface), while the same is not true for shell spinodal topologies derived from solid spinodals with densities different from 50%. To quantitatively ascertain the impact of zero mean curvature on the mechanical properties of spinodal shell topologies, we generated finite element models of 20% and 70%-derived spinodal shell topologies at two different characteristic

feature sizes ($\frac{\lambda}{L} = \frac{1}{8}$ and $\frac{\lambda}{L} = \frac{1}{3}$), and compared their stress-strain curve to those of 50%-derived topologies. All shell thicknesses were chosen so that all shell topologies had a 10% relative density. The results are reported in Fig. 2.14. Two interesting results emerge: (i) 50%-derived shell spinodal topologies outperform both the 20% and the 70%-derived topologies, at both characteristic length scales, confirming that the minimal surface characteristics of 50%-derived spinodal structures are partly responsible for their mechanical efficiency. This is attributed to a more homogeneous stress distribution (see insets). (ii) The mechanical performance of topologies derived from solid spinodal structures with densities significantly different from 50% seem to be largely unaffected by the characteristic feature size, in contrast with 50%-derived spinodal topologies.

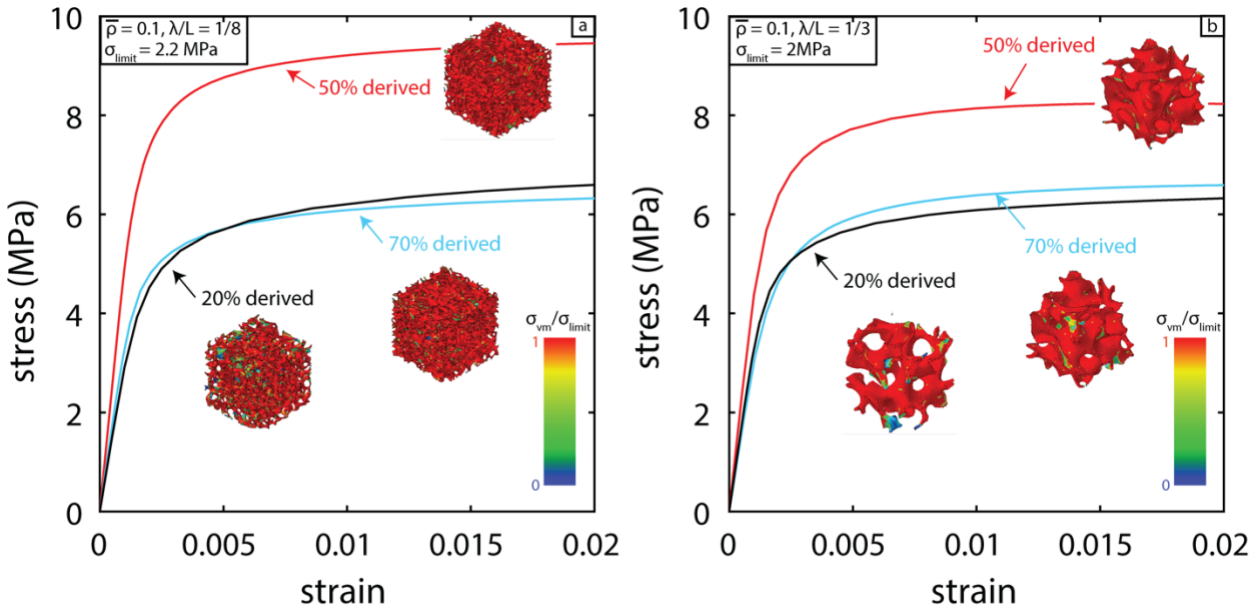

Fig. 2.14 *The effect of mean surface curvature, H, on the mechanical efficiency of shell spinodal topologies. The insets display contours of von Mises stress. Notice that spinodal shell topologies derived from 50%-dense spinodal solids (and hence exhibiting near-zero mean curvature everywhere on the surface) are more efficient than spinodal shell topologies of equal relative density but derived from 20% and 70% solid spinodals (and hence having non-zero mean curvatures throughout the surface). The constituent material has Young's modulus,* $E_s =$

210 GPa and yield strength, $\sigma_{ys} = 235\ MPa$. The stress limits (used to distinguish stress contours where $\frac{\sigma_{vm}}{\sigma_{limit}} \geq 1$) are colored "red", with (a) $\sigma_{limit} = 2.2\ MPa$ and (b) $\sigma_{limit} = 2$ MPa.

It is instructive to compare the mechanical efficiency of solid and shell spinodal topologies to that of a wide range of strut-based and shell-based architected materials, in particular solid strut metallic nanolattices [32], solid strut carbon nanolattices [30], hollow strut metallic microlattices [11,138], hollow strut ceramic nanolattices [12,137], and two mechanically efficient metallic shell-based architected materials, the P-surface material [20] and the D-surface material [27] . These comparisons are presented in Fig. 2.15 in terms of relative Young's modulus, E/E_s, and relative yield strength, σ_y/σ_{ys}, versus relative density, $\bar{\rho}$. Only spinodal topologies with $\lambda/L = 1/5$ are depicted for clarity, for two different values of the base material yield strain: ε_{ys}=0.01 (representative of IP-Dip, thus allowing direct comparison with experimental results) and ε_{ys}=0.001 (representative of a metal). As all the results depicted in Fig. 2.15 for the 10 comparison structures are obtained experimentally, experimental results for solid and shell spinodal topologies (obtained as described in section 2.3.3) are depicted as well. Also plotted on Fig. 2.15 are the Hashin-Shtrikman upper bound for stiffness [97] and the Suquet-Ponte-Castaneda nonlinear upper bound for strength [32,98,99], which represent theoretical limits for the mechanical performance of isotropic cellular materials. We emphasize that solid and shell spinodal architectures are the only isotropic topologies in Fig. 2.15. Notice that while spinodal solid topologies are worse than double gyroid materials and glassy carbon lattices at high relative densities, shell spinodal topologies are on par with or better than all referenced ultralight topologies across a relative

density range covering three orders of magnitude, clearly demonstrating their exceptional mechanical efficiency.

While the model predictions for spinodal shell topologies at ultra-low density (i.e., in the buckling-limited regime) are not verified experimentally due to fabrication challenges, the remarkable imperfection insensitivity of spinodal shell topologies demonstrated in section 2.3.2 strongly suggest that very small knock-down factors will apply, providing confidence in the numerical results.

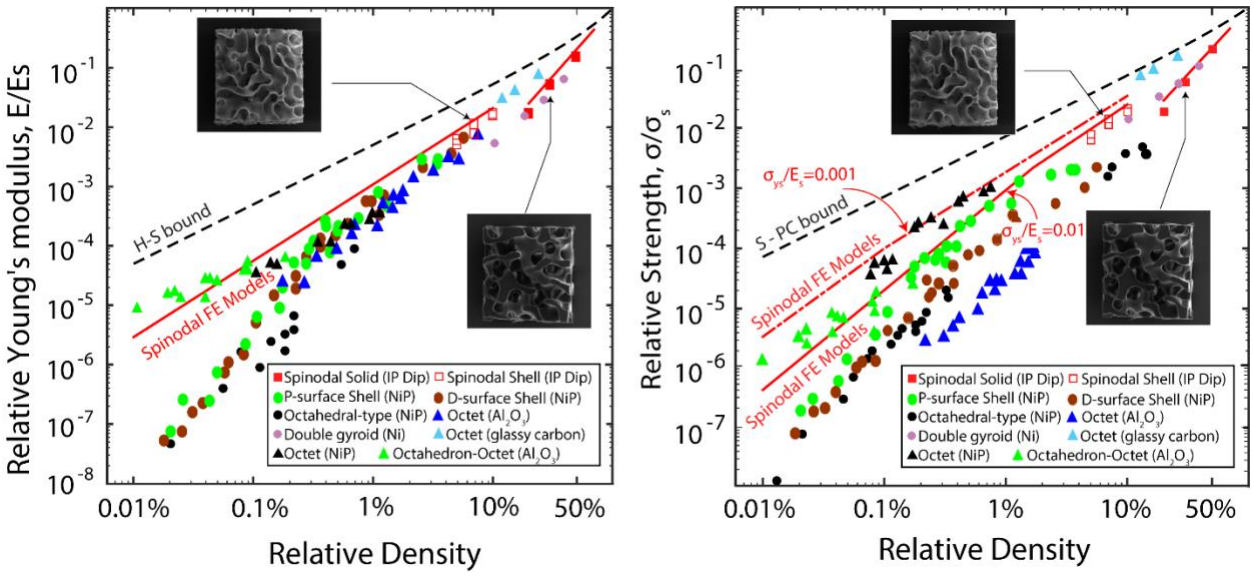

Fig. 2.15 *Comparison of the mechanical performance of solid and shell spinodal topologies and well-established strut-based and shell-based architected materials: hollow octahedral-type metallic microlattices [11], hollow octet ceramic nanolattices [12], hollow octet metallic microllatices [138], hollow octahedron-octet nanolattices [137], solid glassy carbon nanolattices [30], double gyroid nanolattices [32], P-surface [20] and D-surface [27] architected materials. Only spinodal topologies with characteristic feature size,* $\lambda/L = 1/5$ *are depicted for clarity, for two different values of the base material yield strain:* ε_{ys} *=0.01 (representative of IP-Dip, thus allowing direct comparison with experimental results) and* ε_{ys}*=0.001 (representative of a metal). Also depicted are the Hashin-Shtrikman upper bound for stiffness [97] and the Suquet-Ponte-Castaneda nonlinear upper bound for strength [32,97–99], which represent theoretical limits for the mechanical performance of isotropic cellular materials.*

2.4 Conclusion

The mechanical performance of spinodal topologies was numerically investigated and experimentally verified. Cellular materials with spinodal architectures were numerically generated by solving the Cahn-Hillard evolution equation with a Finite Difference numerical scheme. Topologies were extracted at different evolution times, corresponding to different characteristic feature size to domain size ratios, and different relative densities, i.e., different ratios of solid to void phase. We refer to these topologies as solid spinodal models. Another class of spinodal topologies was generated by retaining the interface between the solid and void phases of solid spinodal models and eliminating both volumetric phases: we refer to these topologies as shell spinodal models. The characteristic feature size of spinodal models was calculated by Fast Fourier Transform analysis, and used as a metric for 'unit cell size' of these stochastic cellular materials. This feature size was shown to scale with the cubic root of the evolution time, in agreement with the theory of spinodal decomposition. The distribution of principal curvatures of all spinodal models was also extracted, and verified to be representative of naturally occurring spinodal systems. The mechanical performance of solid and shell spinodal topologies was investigated numerically by finite element analysis.

The numerical models, verified by mechanical experiments performed on solid and shell spinodal samples fabricated at the microscale by two-photon polymerization Direct Laser Writing (DLW), showed three key results: (i) shell spinodal topologies are remarkably efficient, displaying stretching dominated behavior over a very wide range of relative densities; (ii) whereas shell-based architected materials are generally imperfection sensitive, shell spinodal topologies display remarkable imperfection insensitivity, which is expected to result in superior mechanical response at ultra-low relative densities, where

buckling knock-down effects plague the response of most architected materials; (iii) in the low-relative density regime ($\bar{\rho} < 1\%$) architected materials with shell spinodal topologies outperform most strut and shell-based architected materials in terms of specific stiffness and strength, while displaying complete isotropy in three dimensions.

These remarkable properties are entirely due to the topological characteristics of the architecture, and are attributed to the very uniform double curvature across the entire surface of the material, which avoids stress intensifications and prevents local bending deformations of the surface without the introduction of membrane stresses, thus imparting stretching dominated behavior to the cellular material. Importantly, base material effects have not been considered in this analysis: if emerging nano-scale fabrication techniques are used to exploit size effects in metallic and ceramic base materials [32,139,140], unprecedented specific strength can be achieved. These opportunities are currently under investigation.

Finally, we emphasize that the true potential of these topologies stems from the fact that they can be self-assembled, using a variety of physical processes at multiple length scales. While the experiments in this article are performed on 3D printed samples to facilitate fabrication of samples of controlled size and shape and application of mechanical loads, macroscale samples can be produced by selective etching of a metallic solid solution [123] or by phase separation of a colloidal suspension (bijel technology) [124], resulting in nanoscale and microscale characteristic feature size, respectively. These self-assembly methodologies can be combined with additive manufacturing at a larger scale to create macroscale architected materials with unprecedented structural hierarchy, vastly improving the scalability of micro/nano-architected materials processing.

CHAPTER 3

Architected implant designs for long bones: The advantage of minimal surface-based topologies

3.1 Introduction

In chapter 2, we characterized the topology and studied the mechanical properties of spinodal shell-based architected materials. The spinodal shell topology consists of a stochastic minimal surface extracted from the interface of two spinodally decomposing phases [141]. While naturally stochastic, architected materials based on this topology exhibit fully isotropic properties, exceptional specific stiffness and strength and energy absorption (almost on par with those of topologically optimized TPMSs), combined with high imperfection insensitivity (unique for shell-based systems) [141,142]. All these advantages suggest that spinodal shells-based architected materials might be an excellent choice for long bone metallic implants. Importantly, while spinodal-shell architected materials can be computationally designed and additively manufactured with pore sizes comparable to those of existing implants, they are uniquely amenable to self-assembly, where spinodal decomposition of a sacrificial material followed by materials conversion approaches can be used to cost-effectively generate cm-scale implants with micro-scale porosity, with unprecedented combination of specific surface area and pore topology optimization [126,143]. To the best of our knowledge, spinodal shell-based architected materials have not been explored for bone implant applications.

In this chapter, we numerically investigate and compare the performance of three distinct implant topologies for long bones, at three relative densities ($\bar{\rho}_r = 0.1, 0.2$ and 0.3):

the octet truss-based lattice (one of the most mechanically efficient periodic truss-based lattices), the Schwartz P shell-based lattice (a periodic and minimal surface-based design) and the spinodal shell-based lattice (a stochastic and minimal surface-based design). Performance metrics are defined based on the Young's modulus, the safety factor (related to the peak stress) under service conditions, the interfacial surface area per unit volume and the relative bone growth rate (the relative extent of endochondral ossification due to pure mechanical stimuli). Each implant topology (reinforcement) and its surrounding tissue (soft matrix) are modeled as a composite system via finite element analysis, for calculation and analysis of stress fields.

3.2 Materials and methods

3.2.1. Synopsys of approach

We use four measures of biomechanical efficiency used to assess implant performance: the Young's modulus of the implant, the safety factor of the implant under service load, the specific surface area of the implant and the relative bone growth rate index. Whereas the first three measures could be extracted by finite elements analyses of the porous metallic implant alone, the fourth one requires modeling of the tissue occupying the pores of the implant material. Hence, we model each implant as a composite material consisting of a metallic phase (the actual implant structure) with the desired topology, surrounded by a softer phase simulating the bone-forming tissue. Finite element meshes for each implant design (varying implant topology and relative density) are constructed as detailed in section 3.2.2, and interfacial surface areas per unit volume are extracted as explained in section 3.2.3. The models are then loaded in uniaxial compression, and the

Young's modulus, the safety factor and the bone growth rate index are calculated as described in section 3.2.4 and Appendices C and D.

3.2.2. Generation of composite topologies

Each of the three distinct implant topologies is generated numerically to fill a cubic volume of length L_s with 3 x 3 x 3 unit cells. The void space in the cubic unit cells is subsequently filled with a soft matrix to build the topology-reinforced composite. The generation process is illustrated in Fig. 3.1 (a)-(c) and is explained in detail below.

Octet lattices of relative densities $\bar{\rho}_r$ = 0.1, 0.2, and 0.3 (defined as the material-filled volume over the unit cell volume) are generated by manually connecting cylindrical beams of equal radius d and length ℓ, in the Dassault Systèmes CAD software Solidworks. The relative densities can be approximated by [2]:

$$\bar{\rho}_r = \frac{3\sqrt{2}\pi}{2}\left(\frac{d}{\ell}\right)^2 - C_1\left(\frac{d}{\ell}\right)^3 \tag{3-1}$$

where C_1 is a constant depending on nodal geometry and determined to be 5.75 for the current study by fitting the Solidworks-calculated $\bar{\rho}_r$ to d/ℓ. The octet lattices are exported to the Dassault Systèmes finite element software Abaqus where a Boolean operation is performed to fill the open space with a matrix. The resulting octet-reinforced composites are subsequently meshed in Abaqus.

Schwartz P shells-based lattices of $\bar{\rho}_r$ = 0.1, 0.2, and 0.3 are generated using the 3D image processing tool SimpleWare ScanIP. First, the mask generator function (a thresholding process that separates a portion of a given volume from the rest by assigning values to its voxels) of the built-in lattice factory is used to generate two masks, for the solid and its

inverse, by infilling the two equally divided sub-domains separated by the level set equation [26,144,145]:

$$\phi = \cos\left(\frac{2\pi n_x}{L_s}\right) + \cos\left(\frac{2\pi n_y}{L_s}\right) + \cos\left(\frac{2\pi n_z}{L_s}\right) = \mu \quad (3\text{-}2)$$

where n_x, n_y, and n_z are the number of unit cells in the x, y, and z direction, respectively, and μ is a level-set constant, here set to zero. Second, the shell active mask function is used to generate a thin shell on the boundary of the two masks obtained above; this step is conceptually equivalent to thickening the minimal surface represented by equation (3-2) such that it is bounded as $-\mu \leq \phi \leq \mu$, where 2μ represents the thickness of the Schwartz P shells that are generated. Third, Schwartz P shell-reinforced composites are generated using Boolean operations and meshed in ScanIP, and subsequently exported to Abaqus for mechanical analyses.

Spinodal shell-based lattices are generated by solving the Cahn-Hillard equation (the governing equation to model spinodal decomposition) [131]:

$$\frac{\partial u}{\partial t} = \Delta\left[\frac{df(u)}{du} - \theta^2 \Delta u\right] \quad (3\text{-}3)$$

where $-1 \leq u \leq 1$ is the concentration difference between the material and the void phase ($u = 1$ denotes full material and $u = -1$ denotes void space); θ is the interfacial width between the two phases; f is a double-well free-energy function, chosen as $f(u) = \frac{1}{4}(u^2 - 1)^2$; and time t describes the coarsening process (with $t = 0$ representing a nearly homogeneous system, and the final value of t chosen to result in a domain size, m). Eq. (3-3) is solved over a cubic domain A of M x M x M nodes using a finite difference approach, as detailed in [132,141]. The solution to equation (3-3) is a stochastic spinodal solid with 50% relative density [146]. The spinodal solids of $\bar{\rho}_r$ = 0.5 at early (M/m = 6) and later (M/m =

3) coarsening stages are obtained and resampled into 2-dimensional image slices. Note that the images of early stage spinodal solids are cropped along all directions, to result in 3 x 3 x 3 unit cells, consistently with all the other topological samples discussed above. Subsequently, we mask these images in ScanIP, where spinodal shells of $\bar{\rho}_r$ = 0.1, 0.2, and 0.3 are subsequently generated by adjusting the shell thickness pixel values via the shell active mask function; this is equivalent to assign a finite thickness to the interface of spinodal solids at $\bar{\rho}_r$ = 0.5. Finally, Boolean operations are performed where spinodal-reinforced composites are generated and meshed. The meshed spinodal-reinforced composites are imported into Abaqus for mechanical analyses.

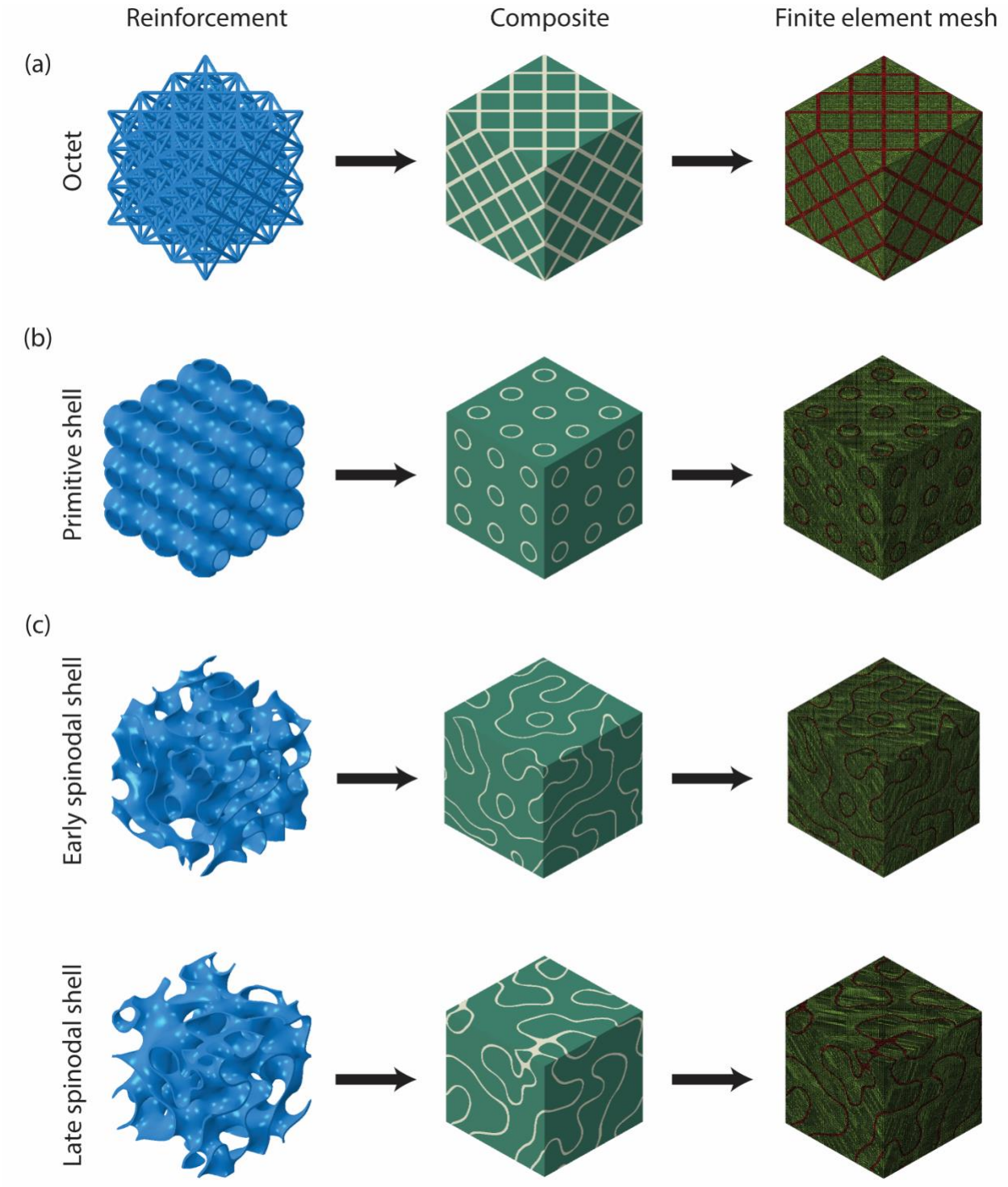

Fig. 3.1 *The numerical generation process of (a) octet lattice, (b) Schwartz P shell and (c) spinodal-shell reinforced composites. For illustration purposes, only 10%-reinforced composites are shown. All insets are not drawn to scale.*

3.2.3. Investigation of interfacial morphology

The interfacial surface area (S_A) between the two phases (implant reinforcement and tissue matrix) of a composite is proportional to the number of unit cells n and the unit cell volume V, and inversely proportional to the unit cell size m in the composite. We can write the topological relation as follows:

$$D = \frac{S_A \cdot m}{V \cdot n} \tag{3-4}$$

where D is a constant that uniquely depends on the interfacial surface topology.

For octet-reinforced composites, D can be obtained by the first-order approximation as:

$$D = \frac{24 \cdot \pi d \ell}{m^2} \tag{3-5}$$

with d and ℓ the diameter and length of the truss members, respectively. Equation (3-5) overestimates S_A by double counting the same surface area several times around the nodes. A higher-order approximation of D is given by:

$$D = \frac{24 \cdot \pi d \ell - C_2 d^2}{m^2} \tag{3-6}$$

where $C_2 = 115.8$ is determined by fitting the Solidworks-calculated S_A at various reinforcement phase densities ($\bar{\rho}_r$ = 0.1, 0.2, and 0.3) in this study.

For Schwartz P shell-reinforced composites, we first construct the interfacial surface according to equation (3-2) using *MiniSurf*, a minimal surface generating software [147]. The generated interfacial surface is composed of many triangular patches. S_A can then be obtained as:

$$S_A = \sum_{i=1}^{H} \|\boldsymbol{a} \times \boldsymbol{b}\|_i \tag{3-7}$$

where H is the total number of triangular patches, i is the patch index that goes from 1 to H, $\boldsymbol{a}$ and $\boldsymbol{b}$ are the two edge vectors of patch i, $\| \quad \|$ is the norm operator, and $\times$ stands for the cross product. Finally, D is extracted using equation (3-4).

For spinodal-reinforced composites, S_A can be simply calculated by the following procedures: first, the two-dimensional slices of spinodal images generated in section 3.2.2 are imported into Matlab as binary three-dimensional matrices (entries of 0 and 1 only). Second, The Matlab built-in function isosurface is used to generate a discretized three-dimensional interfacial surface between the 0s and 1s of the matrices; the discretization provides us with the information about the nodal connectivity. Third, equation (3-7) is used to obtain S_A of spinodal-reinforced composites and finally D is calculated using equation (3-4).

3.2.4. Mechanical simulations

All mechanical simulations are performed using quasi-static finite element analyses in Abaqus. All constituent materials are modeled as linearly elastic solids. The denser phase ($\bar{\rho}_m$ = 0.9, 0.8, and 0.7) of each composite is modeled as a soft matrix with Young's modulus, $E_b = 1$ MPa, and Poisson's ratio, $\upsilon_b = 0.3$ (representing the elastic response of a weak cartilage tissue), while the less dense phase ($\bar{\rho}_r$ = 0.1, 0.2, and 0.3) is modeled as a stiff implant reinforcement with $E_b = 123$ GPa and $\upsilon_b = 0.3$ (representing the elastic response of the commonly used titanium alloy Ti-6Al-4V).

We simulate the mechanical response of each composite under a displacement-controlled uniaxial compression by applying the following boundary conditions (Fig. 3.2):

(1) A downward displacement δ (corresponding to an effective strain $\varepsilon = \frac{\delta}{L_s} = 1\%$, with L_s the cube side length) in the z-direction is applied on the top surface while the bottom surface is constrained from moving in the same direction. Both surfaces are free to translate in the x and y-directions.

(2) All the side surfaces are free to translate in all directions.

(3) Two corner nodes are constrained to prevent rigid body translations and rotations: one node is fixed in the y-direction and the other node is fixed in the x-direction.

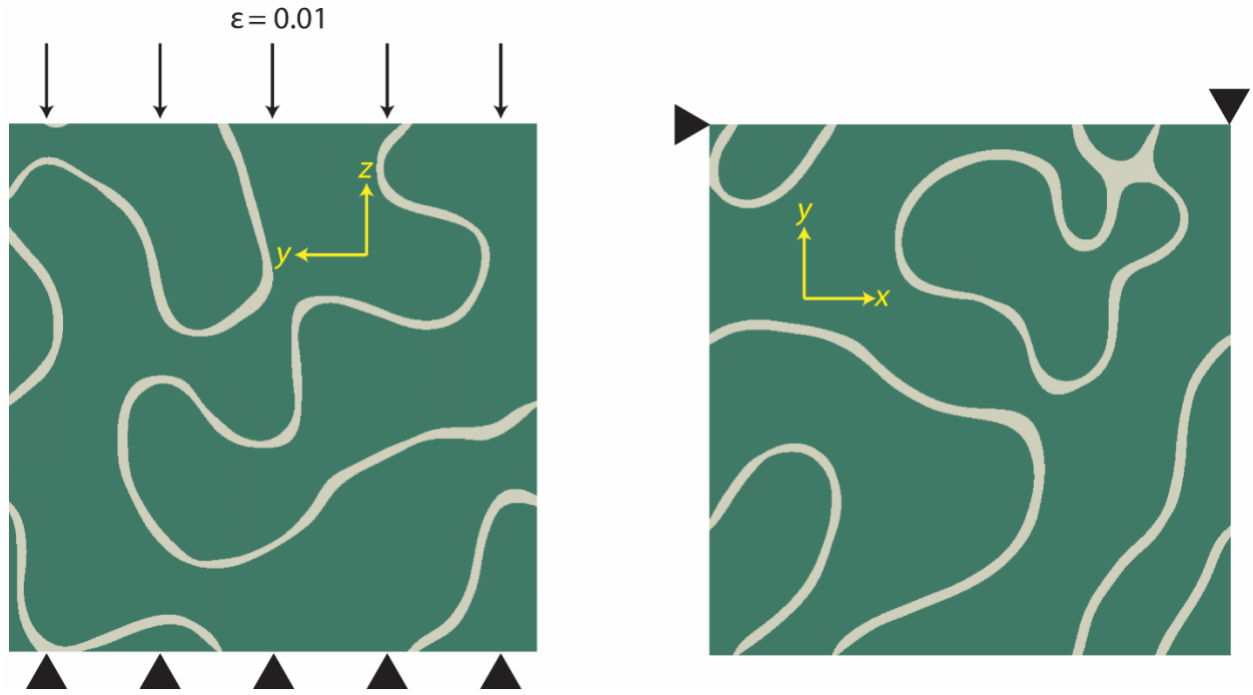

Fig. 3.2 *Illustration of the applied boundary conditions in the y-z and x-y plane. The triangles represent roller supports.*

To obtain the effective Young's modulus, E, we extract the reaction force F in the z-direction such that,

$$E = \frac{F}{L_s \delta} \tag{3-8}$$

The maximum allowable load in a porous implant is limited by the resulting peak stress S_{peak}, subjected to a desired safety factor, SF (SF $>$ $\mathrm{SF}_{\min} = \sigma_y / S_{peak}$, where σ_y is the yield strength of the porous implant's constituent material, taken to be 932 MPa —Ti-6Al-4V— in this case). For highly complex implant topologies, S_{peak} could be strongly affected by the underlying irregular mesh; hence we adopt a more robust measure of S_{peak} as the upper 1% von Mises stress threshold, as described in Appendix C.

Finally, the relative bone growth (an indicator of the extent of endochondral ossification, the process by which cartilage is gradually turned into bones) in the tissue matrix phase is estimated by calculating the combined effect of maximum shear strain and compressive volumetric strain following the procedures summarized in appendix D.

3.3 Results and discussion

3.3.1 Young's modulus

As we assumed linearly elastic small strain response in all mechanical simulations discussed in section 3.2.4 and the reinforcement dominates the mechanical response (the modulus of the reinforcement is 10^5 times larger than that of the matrix), the results corresponding to the constituent material Ti-6Al-4V can be readily extrapolated to other implant materials by simple scaling. E of composites with octet lattice, Schwartz P shell, and spinodal shell implant topologies in three different metallic materials (Ti-6Al-4V, 316L SS, and Co-Cr-Mo) commonly used in long bone implants [148] are plotted against the relative density of the implant in Fig. 3.3 (a).

Regardless of the choice of implant material and relative density of the implant, minimal surface-based topologies (spinodal and Schwartz P) are consistently stiffer than the

beam-based topology (octet lattice), with both early-stage and late-stage spinodal-topologies having very similar and the largest E. This can be explained by examining the von Mises stress distribution, displayed in Fig. 3.3(b): notice that spinodal topologies have the largest distribution of high von Mises stress, followed by the primitive and then by the octet topology. As discussed above, it is evident that the tissue matrix phase provides essentially no structural support, with nearly zero von Mises stress present everywhere.

In terms of mechanical biocompatibility (degree of similarity in mechanical properties, such as Young's modulus, between the porous implant and adjacent native tissue), all topologies are suitable in a wide range of densities: spinodal ($\bar{\rho}_r = 0.1 - 0.3$), primitive ($\bar{\rho}_r = 0.13 - 0.3$), and octet ($\bar{\rho}_r = 0.3 - 0.3$) as shown in Fig. 3.3(a). A summary on E of the composites and Young's modulus of each category of long bones are tabulated in Table 3.1 and Table 3.2 respectively. Since E is a main factor to consider in designing a mechanically compatible implants, it is plotted with other factors such as interfacial surface area in the subsequent sections.

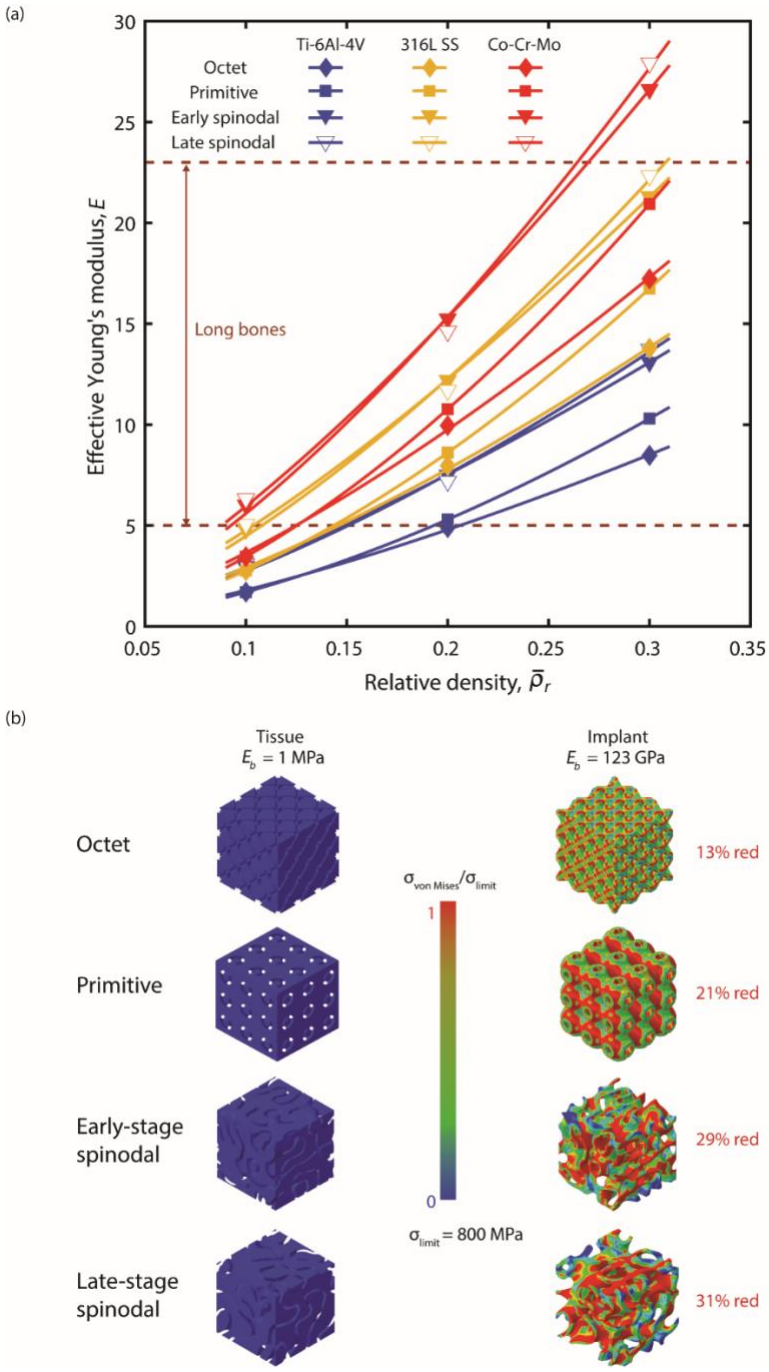

Fig. 3.3 *(a) Effective Young's modulus E of composites with four different implant topologies (represented by the markers) — octet, primitive, early-stage and late-stage spinodal— with three different implant constituent materials (represented by colors) — Ti-6Al-4V, 316L SS, and Co-Cr-Mo — at implant relative density* $\bar{\rho}_r = 0.1, 0.2$ *and 0.3. The typical Young's modulus range for human long bones are bounded by two brown dashed lines [149–162]. (b) The von Mises stress field in both the encompassed tissue and the implant of the composites under 1% uniaxial compressive strain. The stress legend bar is limited by a stress limit* σ_{limit} *such that all stresses above it are colored with red.* E_b *is the base material Young's modulus.*

Table 3.1 The effective Young's modulus E of composites with spinodal, primitive, and octet implant topologies.

Composites	$\bar{\rho}_r$ **of the implant**	**Implant material**	E (GPa)
Spinodal	10–30%	Ti-6Al-4V	3–14
		316L stainless steel	5–22
		Co-Cr-Mo	6–28
Primitive	10–30%	Ti-6Al-4V	2–10
		316L stainless steel	3–17
		Co-Cr-Mo	4–21
Octet	10–30%	Ti-6Al-4V	2–8
		316L stainless steel	3–14
		Co-Cr-Mo	4–17

Table 3.2 The typical Young's modulus of human long bones.

	Long bones	**Young's modulus** (GPa)
Arms	humerus	10 [160], 17 [156,157]
	radius	9-14 [158], 10-19 [159], 16 [160], 19 [156,157]
	ulna	13-16 [154], 16 [160], 18 [156,157]
Legs	femur	8-22 [161], 13-21 [162], 15-22 [151], 15 [152,153], 17 [156,157]
	tibia	15 [149], 8-23 [150], 17 [155], 18 [156,157]
	fibula	15 [149], 5 [155], 19 [156,157]

3.3.2. Interfacial surface area

The interfacial surface area between an implant topology and its surrounding tissue is another important factor that affects mechanical biocompatibility, as larger interfacial surface area allows more bone-implant contact and osseointegration [163,164]. In Fig. 3.4, the relative Young's modulus E/E_b, with E_b the Young's modulus of the base metal, is plotted against the interfacial surface area constant D, a non-dimensional measure of surface area, defined in section 3.2.3. It can be immediately noticed that D of beam-based topologies (octet) increases with increasing relative density, while D of minimal surface-based topologies (primitive and spinodal) is independent of relative density. The implication is that with minimal surface-based topologies we can decouple E from surface area: the relative density of the implant $\bar{\rho}_r$ can be chosen to match the desired long bone modulus, while the implant can still exhibit large surface area; by contrast, with beam-based topologies, the Young's modulus of an implant would need to be increased beyond that of human long bones in order to obtain the same surface area. Importantly, the early-stage spinodal topology has the largest interfacial surface area, almost 1.5–2 times that of the octet topology. This surface area can be further dramatically increased by reducing the pore sizes to the microscale, an opportunity only provided by self-assembly manufacturing approaches unique to spinodal topologies.

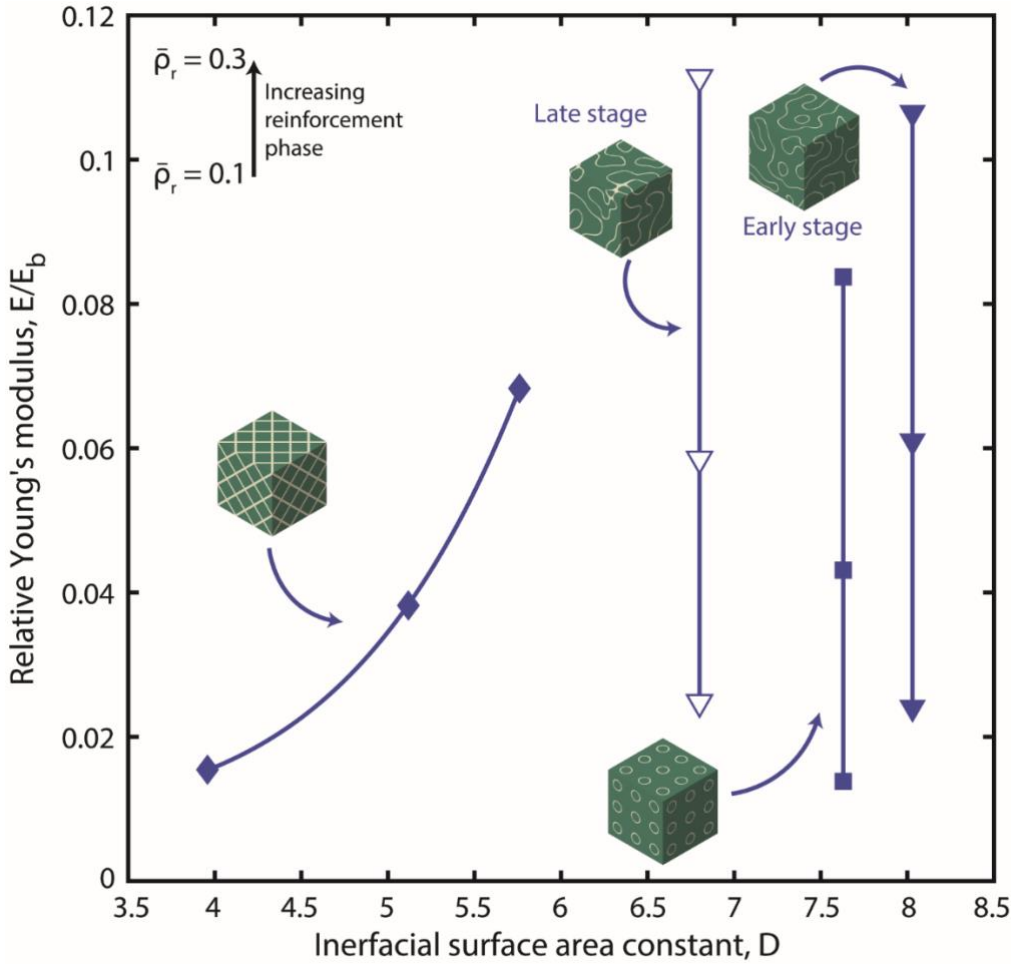

Fig. 3.4 *Relative Young's modulus E/E_b versus interfacial surface area constant D for implant topologies: octet, primitive, early and late stage spinodal with relative densities of 10%, 20%, and 30% ($\bar{\rho}_r = 0.1$, 0.2, and 0.3).*

3.3.3. Safety factor: peak stress

The effective normalized Young's modulus E/E_b is plotted against the safety factor $\mathrm{SF}_{\min} = \sigma_y/S_{peak}$ in the implants, resulting from an applied macroscopic stress of 10 MPa (a reasonable physiological estimate which is used to allow comparison of different implant topologies) in Fig. 3.5. At $\bar{\rho}_r = 0.3$, all minimal surface-based topologies have similar and much larger $\mathrm{SF}_{\min}$ (i.e., smaller S_{peak}) than beam-based topologies; however, this difference slowly diminishes as $\bar{\rho}_r$ is decreased to 0.2, where $\mathrm{SF}_{\min}$ in both minimal surface-based and

beam-based topologies are essentially the same. As $\bar{\rho}_r$ is decreased to 0.1, SF_{min} in beam-based topologies is about 18% larger than (S_{peak} is 15% smaller than) in minimal surface-based topologies. Such difference in SF_{min} is attributed to the fact that at $\bar{\rho}_r > 10\%$ beam-based topologies carry the majority of the load through their connecting nodes, resulting in high nodal stress concentration (higher S_{peak}) [18,165,166]. In addition, at $\bar{\rho}_r > 10\%$, the nodes, rather than the connecting beams, are often the initial point of failure [12,167,168]. By contrast, there are no defined nodes in minimal surface-based topologies [20,141], resulting in much more uniform stress distribution. Furthermore, minimal surface-based topologies also have higher Young's modulus, for a choice of SF and implant constituent material, than the beam-based topologies; notably, E of spinodal topologies outperform all others by almost 1.4-1.9 times. The implication is that with minimal surface-based topologies (especially spinodal-shell topologies), we can choose a smaller implant relative density $\bar{\rho}_r$ (resulting in less material) than with the beam-based topologies, in order to achieve the same required E while satisfying the desired SF and the choice of the implant material.

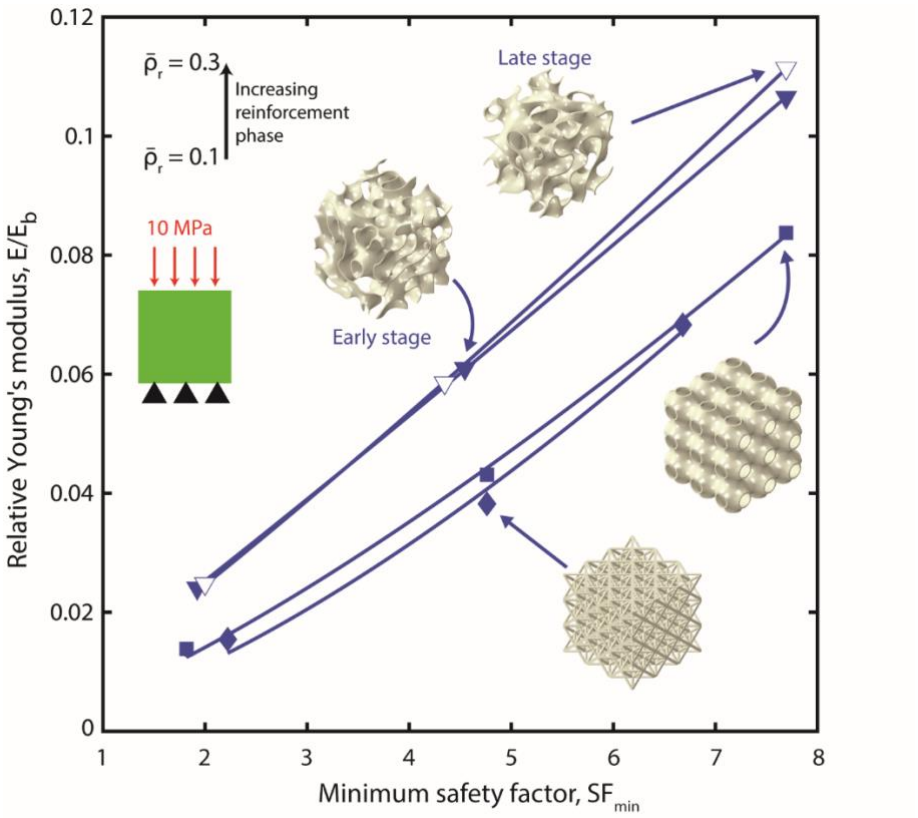

Fig. 3.5 *Relative Young's modulus E/E_b versus minimum safety factor $SF_{min} = \sigma_y/S_{peak}$ (S_{peak} is the von Mises peak stress and σ_y is the yield strength of Ti-6Al-4V) for octet, primitive, early and late stage spinodal implants with relative densities of 10%, 20%, and 30% ($\bar{\rho}_r =$ 0.1, 0.2, and 0.3).*

3.3.4. Relative bone growth index

The relative bone growth index I, an indicator of the relative endochondral ossification rate in the tissue surrounding an implant topology subject to external periodic loading, is estimated as detailed in appendix B and plotted against normalized effective Young's modulus E/E_b in Fig. 2.6. In general, I scales with E/E_b in a power-law fashion, with topology-specific exponent: I of minimal surface-based topologies decreases linearly with with increasing E/E_b, while it decreases parabolically in beam-based topologies. Furthermore, minimal surface-based topologies have much higher I, almost by a factor of

two, then to beam-based topologies. This can be explained by examining two strain fields in the soft tissue matrix: (1) the maximum shear strain ε_{maxs} (accelerating bone growth) and (2) the volumetric strain ε_{vol} (delaying bone growth when compressive), as shown in Fig. 2.7. Tissue matrices in beam-based topologies experience moderate ε_{maxs}, but highly compressive ε_{vol}; on the other hand, minimal surface-based composites experience high ε_{maxs} and relatively low compressive ε_{vol}. Due to their stochastic nature, spinodal topologies induce higher ε_{maxs} than other topologies; but in early-stage spinodal topologies, this gain is offset by a decrease in ε_{vol}, resulting in overall lower I than the primitive topologies.

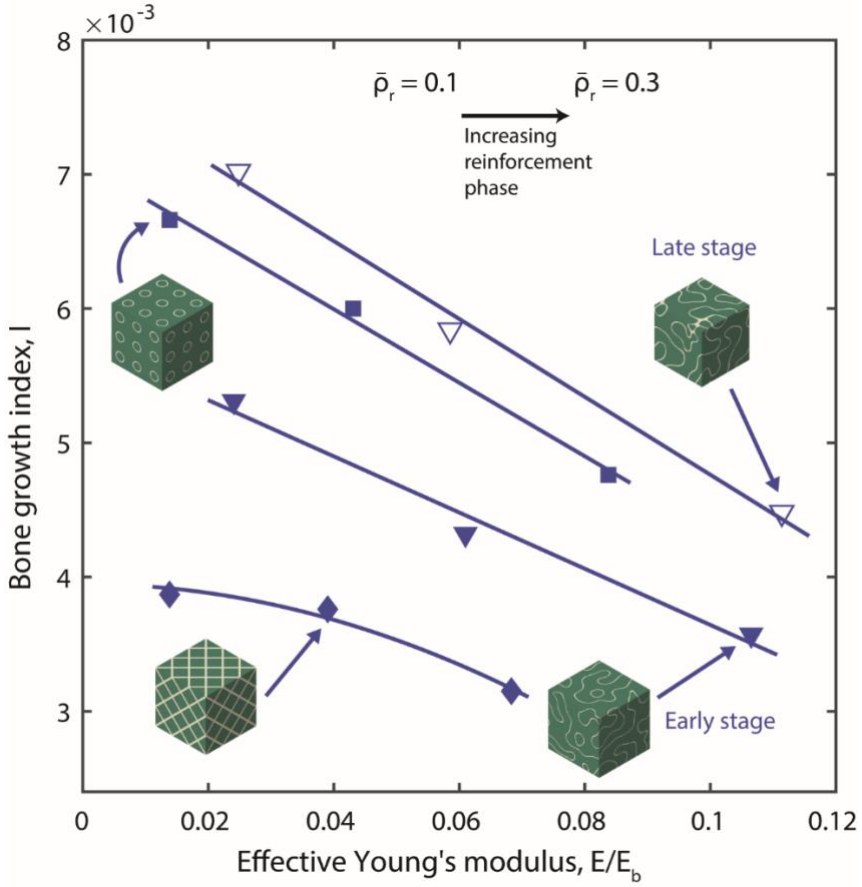

Fig. 3.6 *Bone growth index I in the tissue (the green matrix phase in each composite inset) surrounding octet lattice, Schwartz P shell and spinodal shell-based implants versus effective Young's modulus E/E_b.*

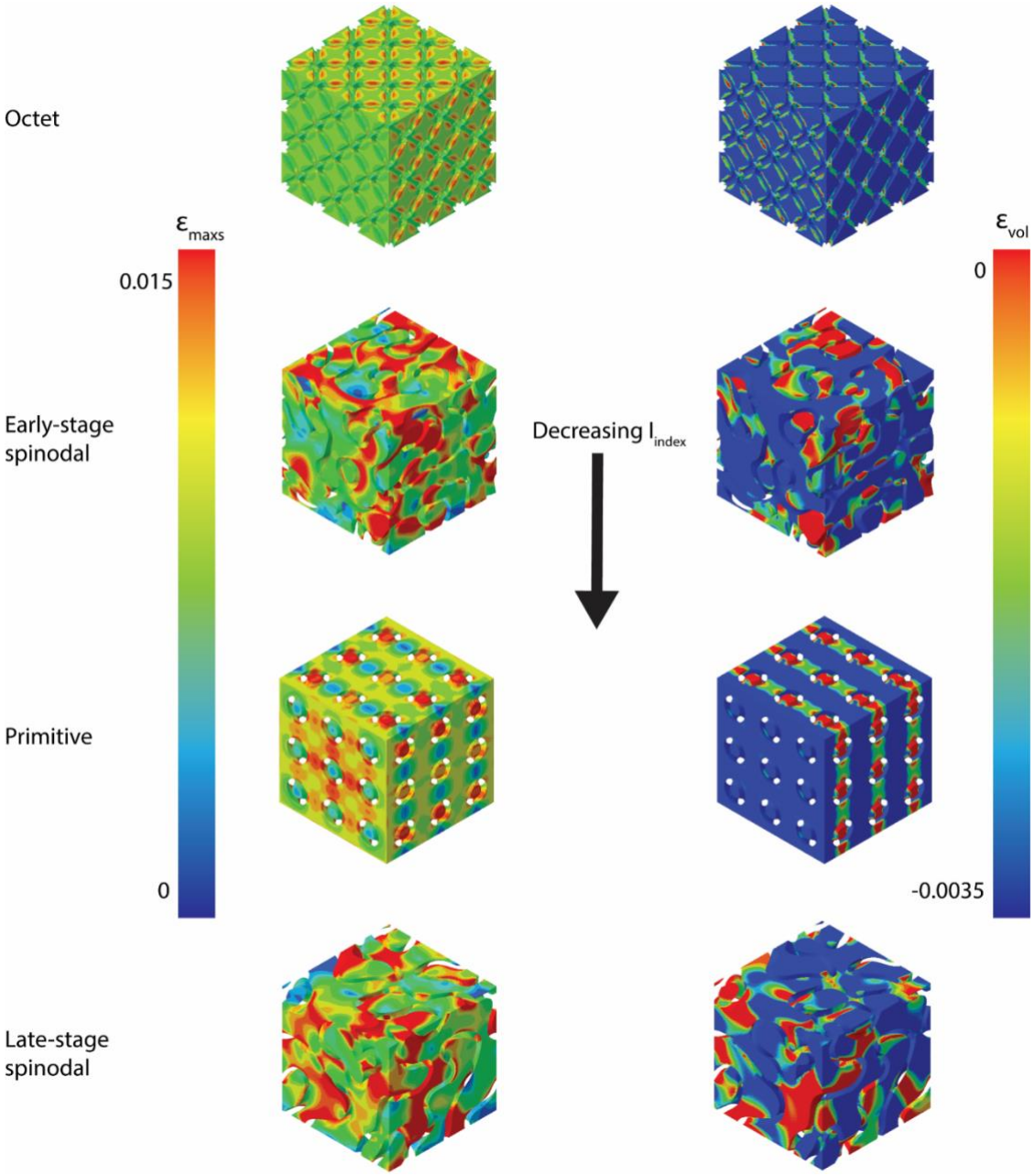

Fig. 3.7 *The maximum shear strain S_{maxs} and the volumetric strain S_{vol} field experienced in the tissue matrix phase (analogous to the encompassed tissue of an implant) of octet, primitive, early and late-stage spinodal-reinforced composites.*

3.4 Conclusions

The biocompatibility of both beam-based (octet) and minimal surface-based (primitive and spinodal) implant topologies was investigated numerically, and presented in terms of four key design factors: the Young's modulus E, the interfacial surface area S_A, the peak stress S_{peak} and the relative bone growth index I. Four key results emerged:

(i) All metallic implant topologies, across a wide range of relative densities, can be designed to have similar Young's modulus as human long bones (E = 5-22 GPa).

(ii) Unlike in beam-based topologies, E and S_A are decoupled in minimal surface-based topologies, allowing the choice of the desired implant stiffness without compromising the specific surface area.

(iii) Bone growth in the tissue surrounding the implant is expected to be much higher in minimal surface-based topologies than in beam-based topologies.

(iv) For a desired implant stiffness and a given external design load, spinodal shell-based implants require the smallest safety factor, resulting in minimal amount of metal required to meet all design constraints. The advantage is particularly pronounced over beam-based implants.

In summary, considering all the design factors discussed in this study for long bone implants, minimal surface-based topologies clearly emerge as superior candidates over beam-based designs. Among minimal surface-based topologies, one must consider the trade-offs between bone ingrowth (S_A and I), safety (S_{peak}), and mechanical biocompatibility (E) of the implants, with spinodal-shell designs often offering the best combinations of

properties. Although not explicitly investigated in the current work, the potential of scalable fabrication via self-assembly of spinodal shell-based micro-architected materials present a unique opportunity for a dramatic increase in specific surface area S_A , without compromising any other attribute.

CHAPTER 4

A versatile numerical approach to calculate the fracture toughness/R-curve of cellular materials

(the work in this chapter was published in doi:10.1016/j.jmps.2020.103925)

4.1 Introduction

In chapter 2, we showed that the spinodal shell topology is extremely mechanically efficient. Furthermore, architected materials with this topology can be manufactured in a by spinodal decomposition and material conversion, resulting in macroscopic cellular solids with unit cell size at the microscale and shell thickness at the nanoscale. These approaches potentially allow scalable fabrication of architected materials that exploit nanoscale size effects on strength, with further improvement on mechanical properties. However, the reduction of the unit cell size to micro/nanoscale necessary for these size effects to become appreciable also dramatically reduces the fracture toughness of the cellular material (please refer to section 1.4.2). This intrinsic reduction might be somewhat compensated by the shell-based topology of the material, which could induce toughening by crack deflection. Hence, it is our interest to investigate the fracture toughness of the spinodal shell-based architected materials. In section 1.4.5, we discussed the numerical approach, boundary layer analysis, that has been widely used to obtain the fracture toughness of cellular materials in many studies. We emphasize that all these numerical studies make three fundamental assumptions: (i) regardless of the constituent material response (linearly elastic brittle or elasto-plastic), the asymptotic stress field is governed by LEFM; (ii) the local fracture event is predicted using maximum stress/maximum strain criterion governed by a constituent

material parameter such as tensile strength σ_{TS}, fracture strength σ_f, or fracture strain ε_f; (iii) the crack tip must lie within the empty space of a unit cell. Under assumption (i), the numerical technique for ductile materials is limited to small displacement analyses such that the plastic zone size remains confined at the crack tip (small-scale yielding). Furthermore, complexity in applying the K-dependent displacement boundary conditions in the periphery of a finite element mesh could rise significantly in complicated topologies such as those with anisotropic properties. Finally, despite few recent attempts [117,169], this technique has yet to be proven as a viable approach for 3D lattice materials. The implication is that fracture toughness investigations of architected materials with spinodal shell-based topologies require the development of novel numerical approaches. In this chapter, we establish a versatile numerical approach (applicable to 2D or 3D cellular materials made of elastic brittle or elastoplastic constituent materials): finite element modeling on the single-edge-notched-bend (SENB) specimen with the maximum strain failure criterion.

4.2 The numerical model

4.2.1 Synopsis

In this work, we combine the maximum strain failure criterion with the single edge notched bend (SENB) specimen configuration to extract the initial fracture toughness, K_{IC}, and the R-curve of cellular materials. We apply this technique to three isotropic 2D lattice topologies (triangular, kagome, and hexagonal), two constituent materials (silicon carbide (elastic brittle) and titanium alloy (power-law elasto-plastic)), and three different relative densities ($\bar{\rho} = 13\%, 16\%, \text{and } 20\%$). We verify that our predictions for initial fracture toughness agree with previous works summarized in Table 4.1 [120,170], validating our

numerical approach. In addition, we show that scaling relationships for fracture toughness, K_{IC}, with relative density only depend on the lattice topology and not on the constituent material (i.e., the same scaling exits for elastic brittle and elastoplastic constituent materials). Furthermore, we demonstrate that triangular lattices exhibit toughening (rising R-curve) even when made of brittle constituent materials. When made of ductile elasto-plastic materials, triangular lattices have the largest initial fracture toughness and the most pronounced R-curves, with multi-stage stable crack propagations and significant spread of plasticity, while hexagonal lattices show nearly no toughening and very low resistance to crack growth. We conclude that the nature of crack propagation in lattices (brittle vs ductile) depends both on the constituent material and the lattice architecture. Finally, we emphasize that the numerical approach presented in this work is applicable to both 2D and 3D architected materials (whether truss or shell-based) made by both brittle and ductile constituent materials, with the only proviso that the crack tip must lie within the empty space of a unit cell (i.e., no stress singularity at the crack tip). These features make this approach ideally suited for further investigations on the toughness characteristics of a wide range of mechanical metamaterials.

Table 4.1 Pre-factors, D, and scaling exponents, d, for mode-I initial fracture toughness, K_{IC} (elastic brittle base materials) and K_{JIC} (elastoplastic base materials) of triangular, kagome, and hexagonal lattices. Results are taken from [I] [108], [II] [120], * current work. The strain hardening exponent, p =16* is obtained by fitting the titanium alloy material properties used in this work to Ramberg-Osgood description. ℓ is the bar length. ε_{ys} is the yield strength, and ε_f is the fracture strain.

	D for mode-I initial fracture toughness					Scaling
	Elastic Brittle $\boldsymbol{D} = \frac{K_{IC}}{\sigma_{TS}\sqrt{\ell}\,\bar{\rho}^{d}}$		Elastoplastic $\boldsymbol{D} = \frac{K_{JIC}}{\sigma_{ys}\sqrt{\ell}\,\bar{\rho}^{d}}\left(\frac{\varepsilon_{ys}}{\varepsilon_f}\right)^{\frac{P+1}{2P}}$			
Topology	I	*	$p = 10^{II}$	$p = 16^{*}$	$p = \infty^{II}$	$d^{I,II,*}$
Triangular	0.5	0.53	0.42	0.57	0.38	1
Kagome	0.21	0.26	0.16	0.22	0.09	0.5
Hexagonal	0.8	0.82	0.5	0.47	0.22	2

4.2.2 Specimen design

Proper design of SENB specimens for fracture toughness investigations in cellular materials is dictated by several conditions: (i) the specimen aspect ratio must follow the ASTM E1820 standard for bulk materials [171], namely $L = 4.5W = 9B$, with L the in-plane specimen length, W the in-plane specimen width, and B the out-of-plane specimen thickness (B is only important if a physical experiment is conducted in accordance with the ASTM standard or in simulations of 3D lattices, but irrelevant in the 2D plane strain simulations discussed in section 2.4); (ii) the number of unit cells must be sufficient to ensure that the K-field exists and is accurately captured [167,169]; (iii) the number of elements per bar (in the case of strut-based structures) must be sufficient to allow nonlinear finite strain analysis under large deformations [120]; (iv) the degree of orthotropy of the cellular material must be carefully considered, given that K depends on a dimensionless function of orthotropy [112,172].

In this study, SENB specimens made of three isotropic 2D lattices (kagome, triangular, and hexagonal) were treated as rigid frames of connected bars, ignoring the nodal geometry. The unit cell of each topology is shown in Fig. 4.1 (a). As these lattices are isotropic, K is only a function of the number of unit cells for a given set of ℓ, $\bar{\rho}$ and σ_{ys}. First, we investigated the convergence of mode-I K-field with increasing number of unit cells, as detailed in Appendix A. Second, we investigated the convergence of the load-line displacement at which the maximum axial strain reached the fracture strain ε_f, with increasing number of Timoshenko beam elements per bar, as detailed in Appendix F. The specimens were built by tessellating the unit cells of each topology according to the results from Appendix E. A notch with $a = W/2$ was subsequently cut in the out-of-plane direction by removing bars. We ensured that $a > \ell^2/t$all densities of all topological specimen, so that failures are toughness-controlled [112]. The final designs of specimens are shown in Fig. 4.1 (b). See Table 4.2 for full specimens' specifications tabulated in Table 4.2.

Table 4.2 Specifications of triangular, kagome, and hexagonal specimens with bar length of (a) ℓ = 3 mm and (b) ℓ = 10 mm.

(a)

$\ell = 3$ mm	Triangular			Kagome			Hexagonal		
$\bar{\rho}$ (%)	13	16	20	13	16	20	13	16	20
t (mm)	0.11	0.14	0.17	0.23	0.28	0.35	0.34	0.42	0.52
a (mm)	104			136			107		
L (mm)	939			1247			936		
W (mm)	208			273			207		
B (mm)	105			139			104		
n_y	40			45			40		
n_e	4			20			30		

(b)

$\ell = 10$ mm	Triangular			Kagome			Hexagonal		
$\bar{\rho}$ (%)	13	16	20	13	16	20	13	16	20
t (mm)	0.37	0.47	0.57	0.77	0.93	1.17	1.13	1.4	1.73
a (mm)	347			453			357		
L (mm)	3130			4157			3120		
W (mm)	694			910			690		
B (mm)	350			464			347		
n_y	40			45			40		
n_e	4			20			30		

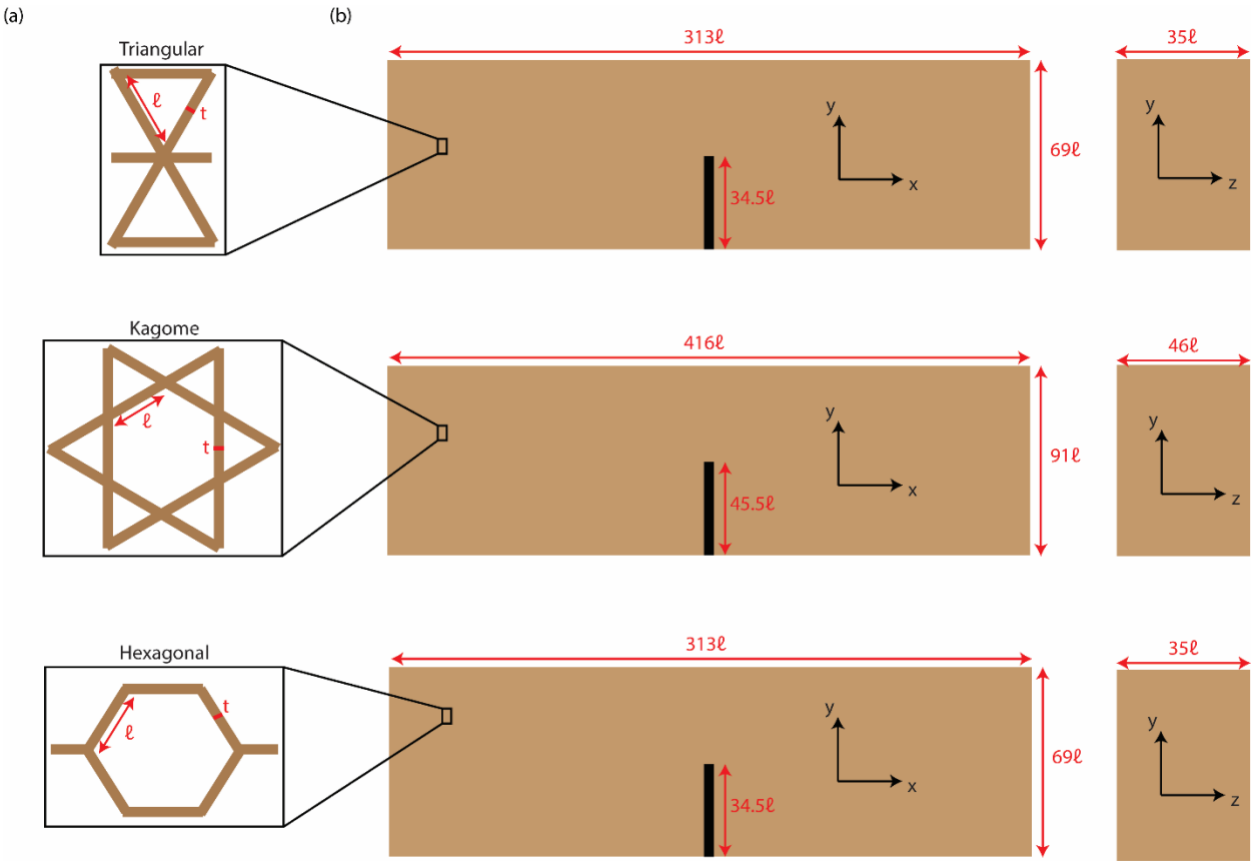

Fig. 4.1 *(a) Unit cell topology and (b) SENB (single edge notched bend) specimen dimensions of triangular, kagome, and hexagonal specimens from top to bottom. Out-plane thicknesses are shown to illustrate the physical dimensions that would be required to perform a SENB experiment in accordance with ASTM standard; these thicknesses are irrelevant for the 2D plane-strain simulation performed in this work.*

4.2.3 Constitutive and damage models

The mechanical behavior of the cell wall materials is described by two models: (i) a constitutive model, which governs the stress-strain behavior of the base material, and (ii) a damage model, which governs fracture of the base material, i.e. material degradation/removal of elements in the finite element analyses, as shown in Fig. 4.2 (a). The constitutive model is divided in two regions: (a) the linear elastic region, defined by the base material Young's modulus, E_s and Poisson's ratio, ν_s, and (b) the power-law strain-hardening plastic region, i.e., $\sigma = \sigma_{ys}(1 + \varepsilon_p{}^n)$, with σ_{ys} the initial yield strength, n the

strain hardening power, and ε_p the plastic strain of the base material. The damage model is described in terms of the fracture strain, ε_f, of the base material: fracture occurs when the maximum axial strain around the crack tip reaches ε_f. To bracket realistic material behavior, two extremely different base materials were considered: (i) titanium alloy (Ti-6Al-4V), representative of ductile metals, with E_s = 123 GPa, ν_s = 0.3, σ_{ys} = 932 MPa, n =0.7237 and ε_f = 0.1105 [173], as shown in Fig. 4.2 (b); and (ii) silicon carbide, representative of elastic brittle ceramics, with E_s = 410 GPa, σ_f = 550 MPa, ν_s = 0.14, and no strain hardening (resulting in $\varepsilon_f = \sigma_f/E_s$ = 0.0013), as shown in Fig. 4.2 (c).

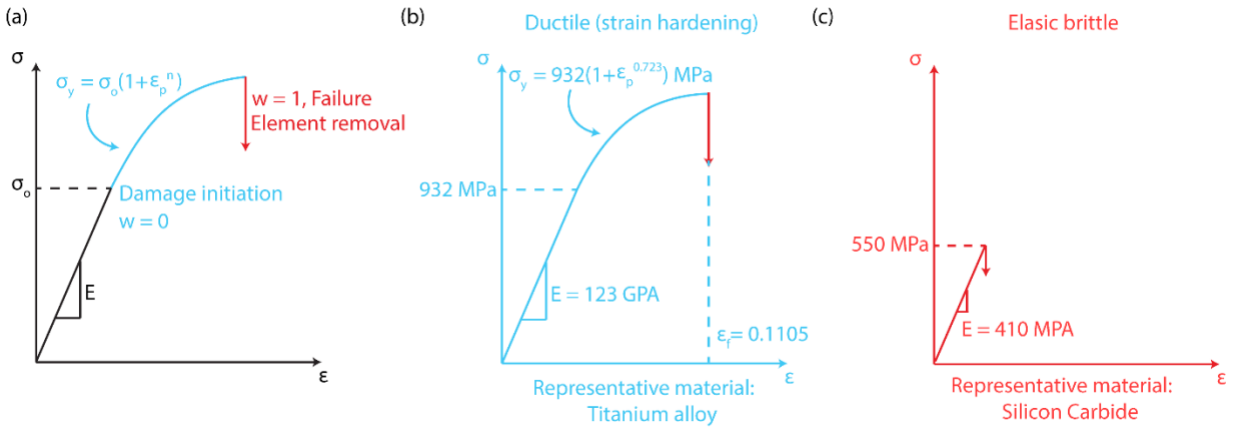

Fig. 4.2 *Representative stress-strain curves of (a) constitutive and damage model, (b) titanium alloy (Ti-6Al-4V), and (c) silicon carbide.*

4.2.4 Finite element methodology for extraction of the fracture toughness

Mode-I fracture toughness of SENB specimens made of triangular, kagome, hexagonal lattices at $\bar{\rho}$ = 13%, 16% and 20%, and ℓ = 3 mm and 10 mm was investigated by simulating three point bending experiments (as outlined in ASTM E1820 [171]) by finite elements analysis. We used Abaqus/Explicit for all simulations, with mass scaling appropriately

chosen to approach quasi-static response. To represent two-dimensional bars with rectangular cross sections in plane strain with one-dimensional beam elements, E_s and ν_s of the base materials were replaced by modified Young's modulus, $E_s' = E_s/(1-\nu_s^2)$ and Poisson's ratio, $\nu_s' = \nu_s/(1-\nu_s)$ [108,174]. Three spreaders (defined as analytic rigid surfaces in Abaqus) were used to apply three-point-bending boundary conditions without suffering local indentations; this practice had been used previously for fracture toughness testing of strut-based lattices [112,167] and was also recommended by ASTM C393/C393M [175] for flexural testing of sandwich beams. Frictionless contacts were assumed between the spreaders and the specimen, to further reduce localized deformation. One spreader was placed at the top midspan above the sample notch, while the other two spreaders were placed four sample widths apart at the bottom of the specimen, as shown in Fig. 4.3 (a).

Boundary conditions were applied as follows: (i) each bottom spreader could rotate around a fixed reference point, representing the center of a roller, and (ii) a sufficiently large load-line displacement was applied at the top spreader in the negative y-direction, until the final crack length is greater than the maximum crack capacity for fracture toughness calculations specified by ASTM E1820 [171], as shown in Fig. 4.3 (a). The damage model with maximum axial strain criterion (refer to section 4.2.3) was used to describe the local fracture around the crack tip.

For this criterion, accurate calculation of the axial stresses and strains in each beam is essential. For bending-dominated lattices, the maximum axial strain at the surface of each beam is significantly higher than the value at the neutral axis. As the default stress outputs for beam elements are at the neutral axis, an Abaqus user subroutine VUSFLD (vectorized user defined field) was created to extract beam surface stress and strain levels. As high

frequency oscillations of the mechanical response could occur during a fracture event, we applied Butterworth real-time filtering with a cutoff frequency equals to the twice natural frequency of the specimen, extracted during quasi-static analyses. The natural frequency of each specimen was obtained by performing a linear perturbation analysis (see Appendix G).

Following the procedures outlined for fracture toughness calculations in ASTM E1820 [171], and summarized in Appendix H, the load-line displacement and the load-line reaction force were extracted at the top spreader and used to calculate the J-integral, J, consisting of both elastic and inelastic contributions to crack resistance. As the specimens have simple 2D prismatic architectures, crack extensions were tracked visually in post-processing. The fracture toughness, K_J, was then calculated as $K_J = \sqrt{EJ}$ where E is the effective Young's modulus of the lattice material, simply extracted from the scaling laws of triangular, kagome, and hexagonal lattices [1,108]. The details of all fracture toughness calculation procedures are summarized in Appendix H. R-curves were constructed by plotting $K_J(i)$ against the change of crack length at instant (i), i.e., $\Delta a(i) = a(i) - a(1)$, and fitted with a two-term power law equation:

$$K_J = K_{JIc} + \mathrm{c}\left(\frac{a(i)-a(1)}{a(1)}\right)^{\mathrm{m}} \tag{4-1}$$

where K_{JIC} is the initial fracture toughness, c is the toughening coefficient, and m is the toughening power.

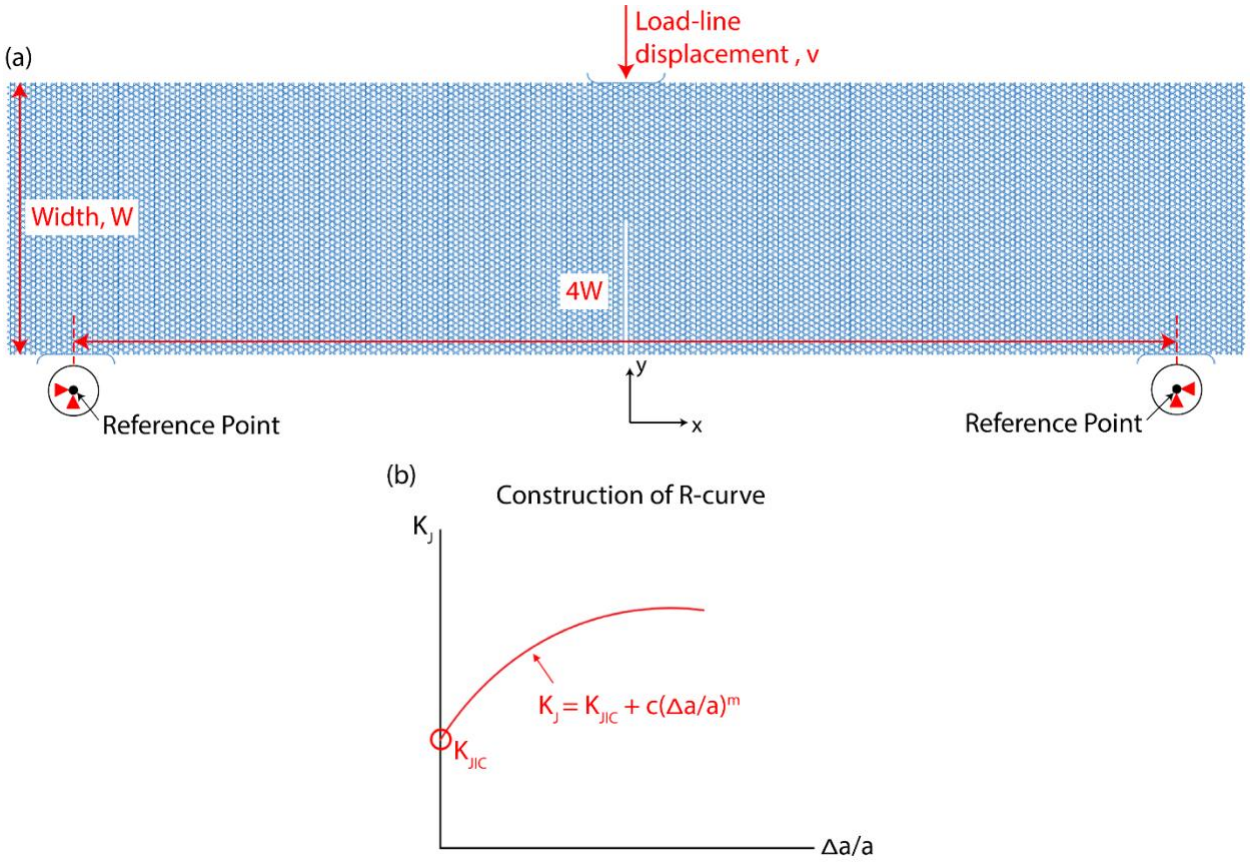

Fig. 4.3 *(a) Boundary conditions on a SENB specimen made of 2D lattices. Three spreaders are used: one at the top midspan and two at the bottom locations distance 4W from each other, to prevent highly localized deformation. Load-line displacement are applied at the top spreader while each of the bottom spreaders can rotate around a reference point, representing the center of a roller. (b) Construction of R-curve with fracture toughness, K_J against normalized change of crack length, $\frac{\Delta a}{a}$. Two-term power law fit, $K_J = K_{JIC} + c(\frac{\Delta a}{a})^m$, where K_{JIC} is the initial fracture toughness, c is the toughening coefficient, and m is the toughening power.*

4.3 Fracture toughness of 2D lattices

4.3.1 Mechanisms of deformation and damage and the size of the plastic region

(a) Silicon carbide specimens

The load-line reaction force, *P*, versus load-line displacement, *v*, curves for the three cellular specimens made of elastic brittle silicon carbide are shown in Fig. 4.4 (a). Two different relative densities are explored for each topology. Filtered and unfiltered curves are

identical until the initial fracture event, at which point the unfiltered *P*-*v* curves start to display high frequency response. In general, deformations are elastic brittle, such that *P* increases linearly with ν until initial fracture (denoted as point 1 in Fig. 4.4 (a)), followed immediately by catastrophic failure (significant loss of load-carrying capacity). The exception is the triangular specimen at $\bar{\rho}$ = 20%, which retains most of its load-carrying capacity after initial fracture and requires additional, albeit small, load to come to catastrophic failure. We hypothesize that this unusual behavior is likely due to crack deflection and crack branching occurring right after the initial fracture event, as shown in Fig. 4.4 (c): after the first bar, which is aligned with the principal stress direction, breaks, the crack hits a node and the next failure event occurs at side bars which are slightly less loaded, requiring additional work to fracture. Clearly, this behavior can be modified by node design, which is absent in the FEM simulations presented herein. The implication is that careful architectural design can potentially increase the fracture toughness, even in the case in which the constituent material is elastic brittle. In Fig. 4.4 (b), zoomed-in crack tip regions are drawn for each specimen to indicate initial fracture locations. These initial fracture locations agree well with those identified using boundary layer analyses in [108].

(b) Titanium alloy specimens

The specimens made of elastoplastic titanium alloy (Ti-6Al-4V) initially deform in a linear elastic manner, followed by yielding, strain hardening and subsequently initial fracture; afterwards, the specimens experience gradual damage propagation (rather than abrupt catastrophic load drop as in elastic brittle base materials), up to final failure (defined as significant loss of load-carrying capacity). As for the case of the brittle materials, both the filtered and unfiltered P- v curves are identical until the initial fracture events.

Triangular lattices exhibit the most gradual transitions to final failures: after the initial fracture (denoted as point 1 in Fig. 4.5 (a)), P still increases with ν to a peak load followed by multiple stages of small load drops (denoted as points 2, 3, 4, and 5 in Fig. 4.5(a)). Each load drop is determined by fracture of a few bars, with the precise sequence indicated in Fig. 4.5(d). Kagome lattices display the second most gradual transition to final failure: after initial fracture (denoted as point 1 in Fig. 4.5 (b)), P increases with v up to a peak load, followed by a couple of load drops (denoted as points 2 and 3 in Fig. 4.5(b)); each drop corresponds to fracture of a number of bars, which is generally larger than for triangular lattices, as shown in Fig. 4.5(e). Finally, hexagonal lattices show the most sudden transition to final failure: after the initial fracture event (denoted as point 1 in Fig. 4.5 (c)), P increases with v up to a peak load, but is immediately thereafter followed by a catastrophic load drop (denoted as point 2 in Fig. 4.5 (c)). In addition, the corresponding crack extends and branches along two paths (both at a 45-degree angle to the horizontal) as shown in Fig. 4.5 (f). Interestingly, the hexagonal lattice is the only lattice that exhibits crack branching.

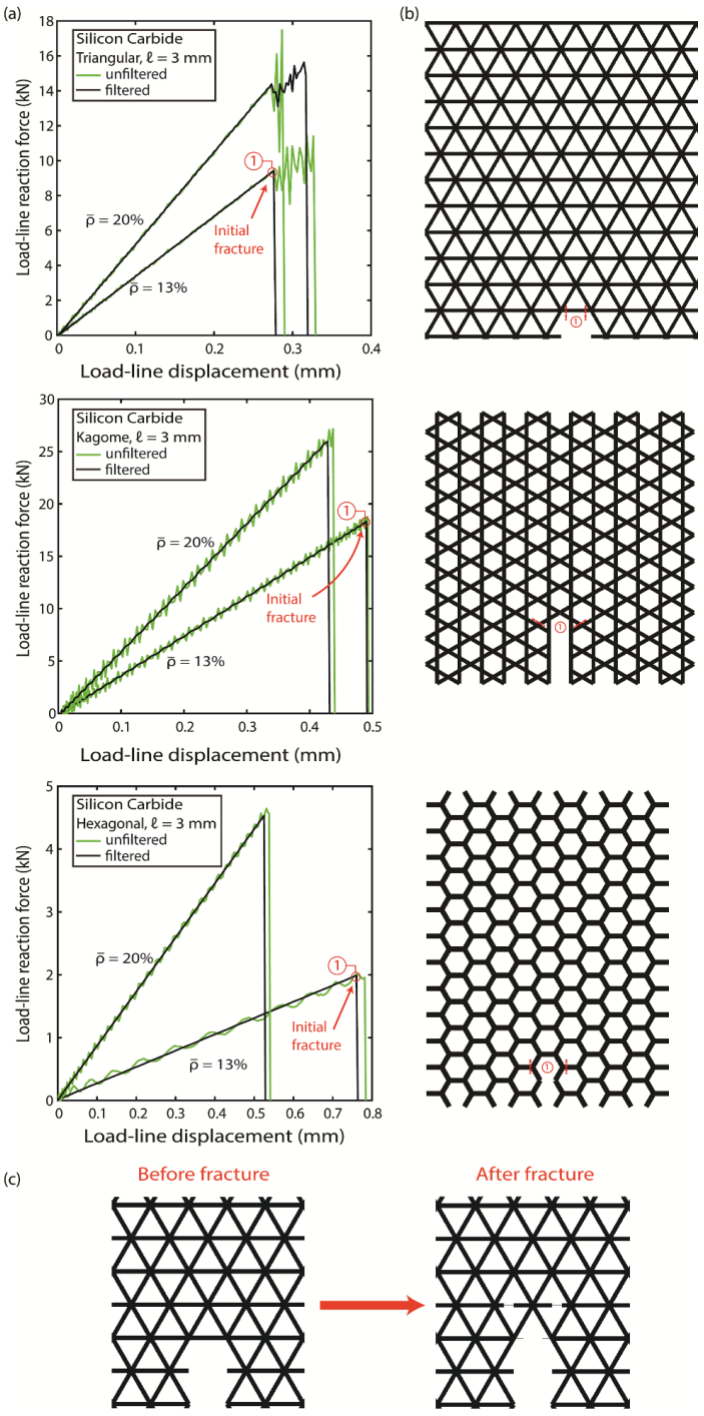

Fig. 4.4 *Deformation maps of topological specimens made of silicon carbide at $\bar{\rho}$ =13% and 20%: (a) load, P, versus load-line displacement, v, were plotted till overall kinetic energy exceeds 5% of overall internal energy of each specimen in each simulation. Encircled number one corresponds to the initial fracture followed immediately by catastrophic failures (significant load drop) and(b) the corresponding initial fracture locations are represented by red dashed line (c) Illustration of crack branching of the $\bar{\rho}$ =20% triangular lattice immediately after fracture. All lattices are not drawn to scale.*

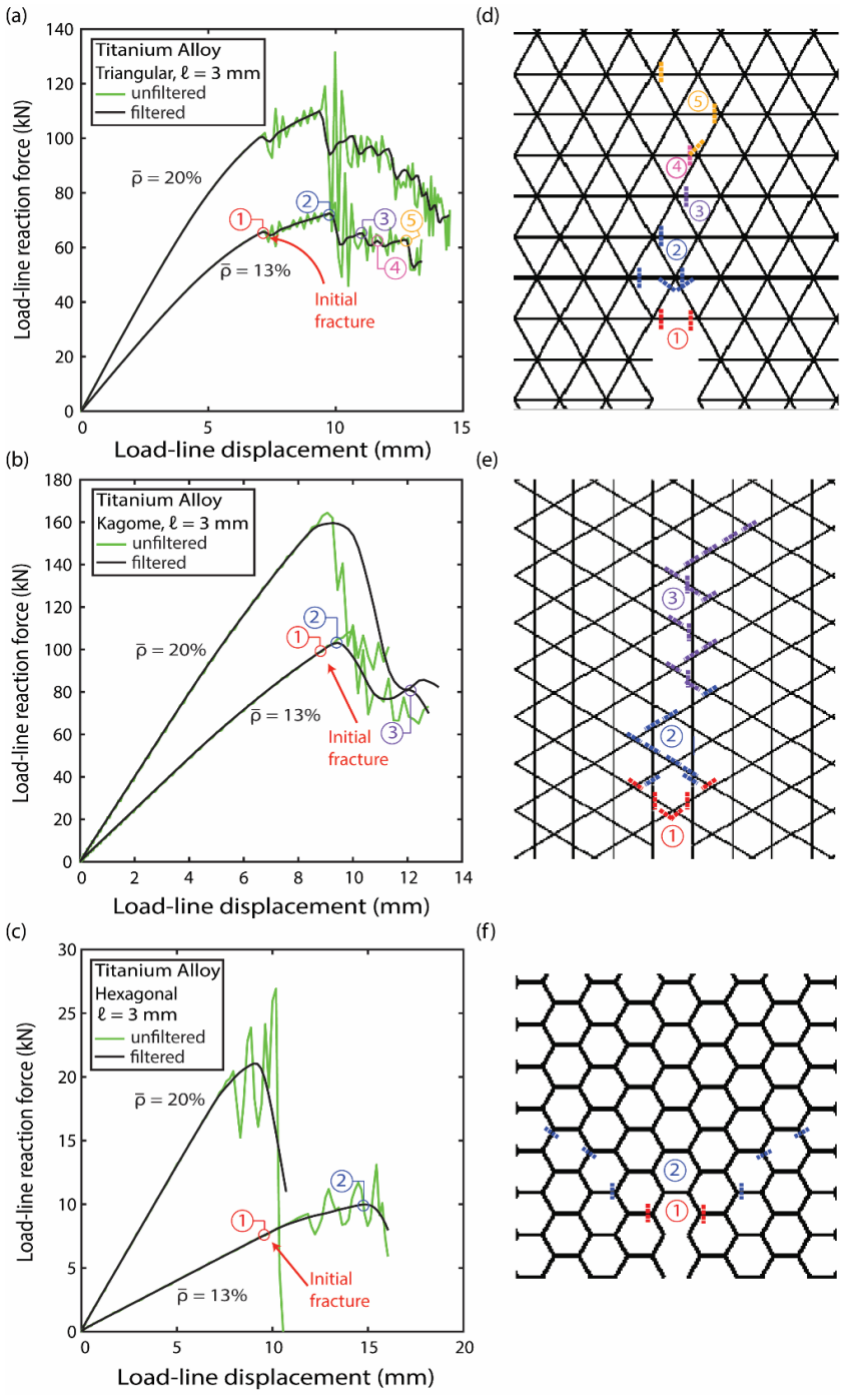

Fig. 4.5 *Deformation maps of topological specimens made of Titanium Alloy (Ti-6Al-4V) at $\bar{\rho}$ =13% and 20%: load, P, versus load-line displacement, v, of (a) triangular specimens, (b) kagome lattices, and (c) hexagonal lattices were plotted till overall kinetic energy exceeds 5% of overall internal energy of each specimen in each simulation. Encircled number one corresponds to initial fracture and the subsequent encircled numbers correspond to each load drop. The fracture locations of each encircled number in (a), (b), and (c) are represented by corresponding colored dashed line in (d), (e), and (f) respectively; the lattices are not drawn to scale.*

These differences in crack propagation can be directly related to the size of the process zone ahead of the crack tip. The larger the process zone (i.e., the number of bars that are experiencing significant plastic deformation during crack propagation), the more gradual the loss of load carrying capacity in the sample, and the more pronounced the toughening response of the lattice. For the purpose of simple comparison between three lattices, we arbitrarily define the process zone as the rectangular region encompassing all the bars that attain the plastic strain limit, ε_{plimit} = 0.01. The process zone size right before the initial fracture event for the three sample topologies at two relative densities is plotted in Fig. 4.6. Regardless of the relative density, the triangular specimens have the largest fractional area (defined as the process zone area normalized by the sample size) of 2.4%, about twice as large as that for kagome specimens; by contrast, the hexagonal specimens have extremely localized failures, with negligible process zone size.

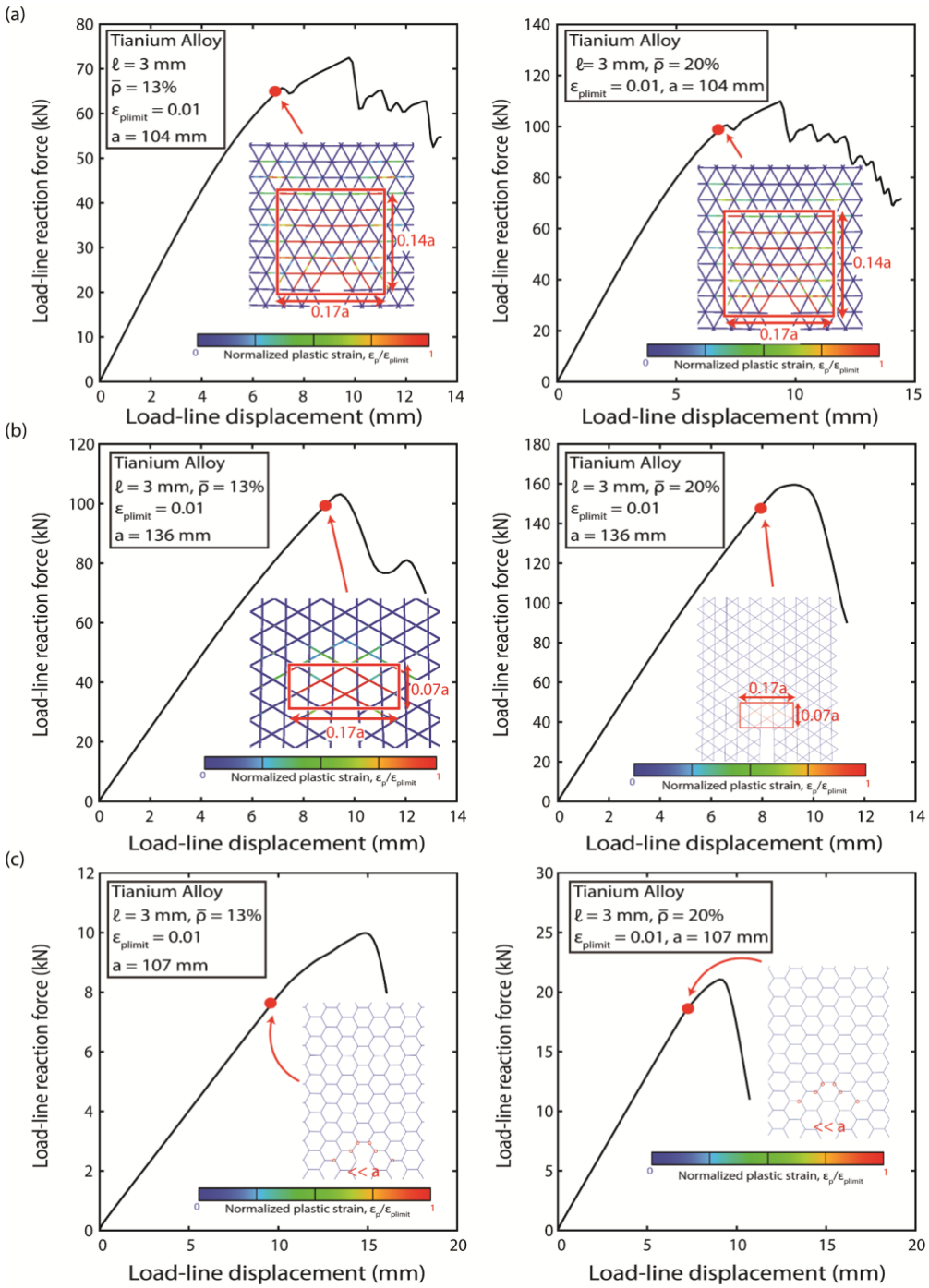

Fig. 4.6 *Contours of absolute normalized plastic strain, $\varepsilon_p/\varepsilon_{plimit}$, around the crack tip between (a) triangular lattices, (b) kagome lattices, and (c) hexagonal lattices made of titanium alloy (Ti-6Al-4V) with ℓ = 3 mm at relative density, $\bar{\rho}$ = 20% and 13% right before the initial fracture. The corresponding location on the load-displacement curve of each contour is indicated by a red dot. Plastic strain limit, ε_{plimit} = 0.01 is used in the strain contours such that for all $\varepsilon_p/\varepsilon_{plimit}$ > 1, the contour appears to be red. Red rectangles or circles are used to estimate the size of plastic regions. The inset lattices are not drawn to scale.*

4.3.2 Scaling relations for fracture toughness and R-curve

(a) Silicon carbide specimens

The fracture toughness of elastic brittle specimens was extracted using the J-integral method, only considering the elastic J component, J_{el}, (see Appendix D for details). The fracture toughness, K_{IC}, scales with relative density, $\bar{\rho}$ as $\bar{\rho}^1$, $\bar{\rho}^{0.5}$, and $\bar{\rho}^2$ in triangular, kagome, and hexagonal specimens, respectively, as shown in Fig. 4.7 (a). In addition, we found that the fracture toughness is largest for the Kagome specimens and lowest for the hexagonal specimens. Furthermore, we verified that K_{IC} depends linearly on the square root of the strut length, $\sqrt{\ell}$ [100], as shown in Fig. 4.7 (b). All these findings are perfectly consistent with the results obtained using boundary value analysis in [108], and thus validate our numerical approach for the calculation of the fracture toughness in cellular materials specimens.

(b) Titanium alloy specimens

The initial fracture toughness, K_{JIC}, toughening coefficient, C, and toughening power, m, of the titanium alloy (Ti-6Al-4V) lattice specimens were extracted following the procedures discussed in section 4.2.4.

The initial fracture toughness reveals some important results: (i) while the scaling relationships for K_{JIC} with $\bar{\rho}$ remain the same as for the elastic brittle case, the actual values of K_{JIC} are ~5 times larger, as shown in Fig. 4.8 (a); (ii) the difference between the performance of the triangular and kagome lattices is reduced relative to the brittle base material case, while the hexagonal lattice remains the least efficient design. The implication is that high initial fracture toughness can be achieved at low relative density by designing a triangular or kagome lattice made of a ductile base material. In addition, we show that even

in the plastic case, K_{JIC} still linearly depends on $\sqrt{\ell}$, as shown in Fig. 4.8 (b). The superior efficiency of the triangular lattices can be attributed to the extent of the process zone ahead of the crack tip (Fig. 4.6), which more than compensates the elastic crack blunting that makes kagome designs preferred for brittle materials [108].

Similar scaling relationships can be extracted for the toughening coefficient, C, as shown in Fig. 4.9 (a). Remarkably, the scaling exponents are the same as for the initial fracture toughness. Triangular lattices have the largest toughening coefficients, followed by kagome and hexagonal lattices. By contrast, the toughening exponent, m, does not substantially depend on the relative density or lattice topology, maintaining a value ~0.52-0.58. These features are evident in the R-curves displayed in Fig. 4.9 (b). Notice the substantial difference between triangular and kagome lattices: while their initial fracture toughness is very similar, triangular lattices toughen much more strongly during crack propagation. Again, this can be attributed to the larger process zone dimension in triangular specimens. Consistently with their very isolated yielding events, hexagonal lattices display much lower fracture toughness than the other lattice classes, especially at low relative density. We should emphasize that our choice to define local strut fracture when a critical value of the strain is reached at the outer surface of the strut potentially penalizes bending-dominated lattices made of ductile base materials, in which struts can still carry load after surface cracking has initiated. As hexagonal lattices are bending dominated, while triangular lattices are stretching dominated (with kagome lattices in between), this factor might contribute to the large performance difference among the three lattice topologies examined here. While in practice hexagonal and kagome lattices might perform a bit better than

predicted here, we do not expect this contribution (if present) to affect any of the conclusions of this work.

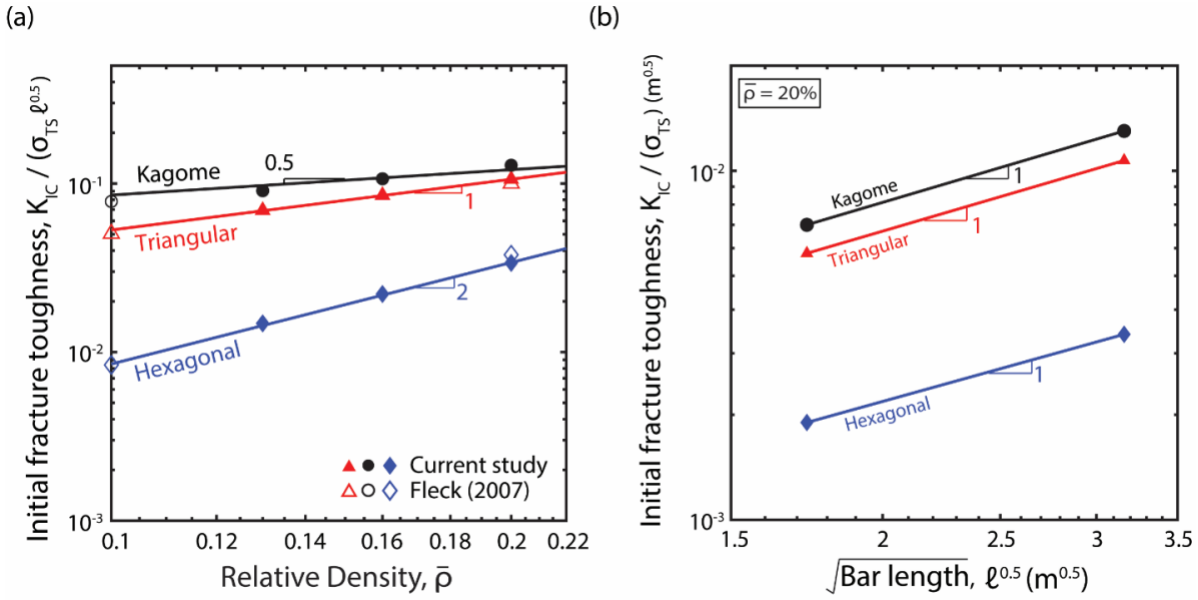

Fig. 4.7 *Scaling relationships for initial fracture toughness in triangular, kagome, hexagonal specimens made in silicon carbides with (a) the relative density $\bar{\rho}$ and (b) the square root of bar length, $\sqrt{\ell}$.*

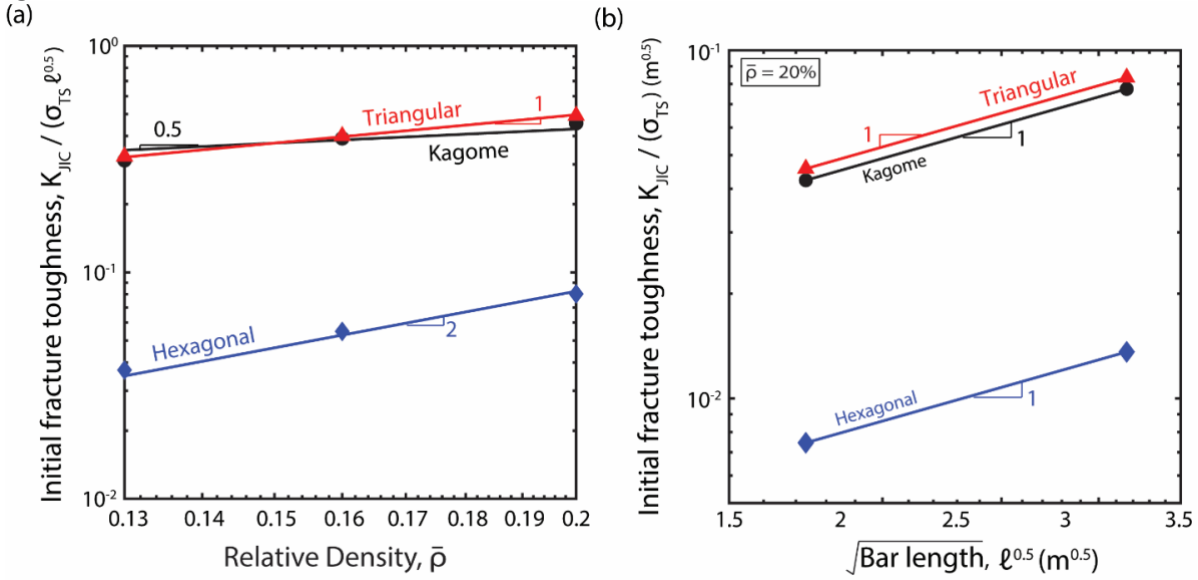

Fig. 4.8 *Scaling relationships for initial fracture toughness in triangular, kagome, hexagonal specimens made in titanium alloys (Ti-6Al-4V) with (a) the relative density $\bar{\rho}$ and (b) the square root of bar length, $\sqrt{\ell}$.*

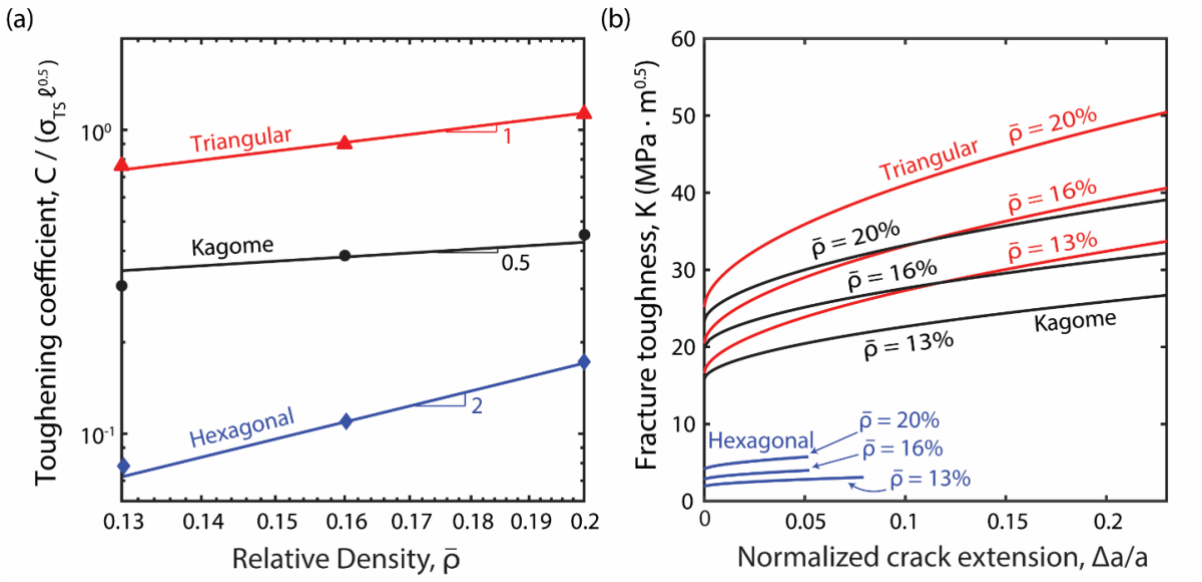

Fig. 4.9 *(a) scaling relationships for toughening coefficients, C, and (b) R-curves of triangular, kagome, and hexagonal specimens made in titanium alloy (Ti-6Al-4V).*

It is instructive to compare the fracture toughness of lattices with the universe of existing materials. We plot both initial fracture toughness, K_{JIC}, and fracture toughness at final failure, K_{JFC}, of triangular, kagome, and hexagonal lattices of ℓ = 3 mm at $\bar{\rho}$ = 13%, 16%, and 20% (corresponding to density of 585-900 kg/m^3) made in titanium alloy (E_s = 123 GPa, ν_s = 0.3, σ_{ys} = 932 GPa, n = 0.7237, $\varepsilon_f = 0.1105$) as shown in Fig. 4.10. Both triangular and kagome lattices at this length scale outperform the majority of natural materials in terms of K_{JIC}. When considering K_{JFC}, triangular lattices approach the fracture toughness of bulk titanium alloy. In contrast, hexagonal lattices are comparable to other natural materials (e.g, paper) in terms of both K_{JIC} and K_{JFC}. The conclusion is that topology manipulations can significantly alter both K_{JIC} and K_{JFC}. However, this conclusion is here only proved for 2D lattices, and remains unexplored for 3D topologies, either strut-based or shell-based.

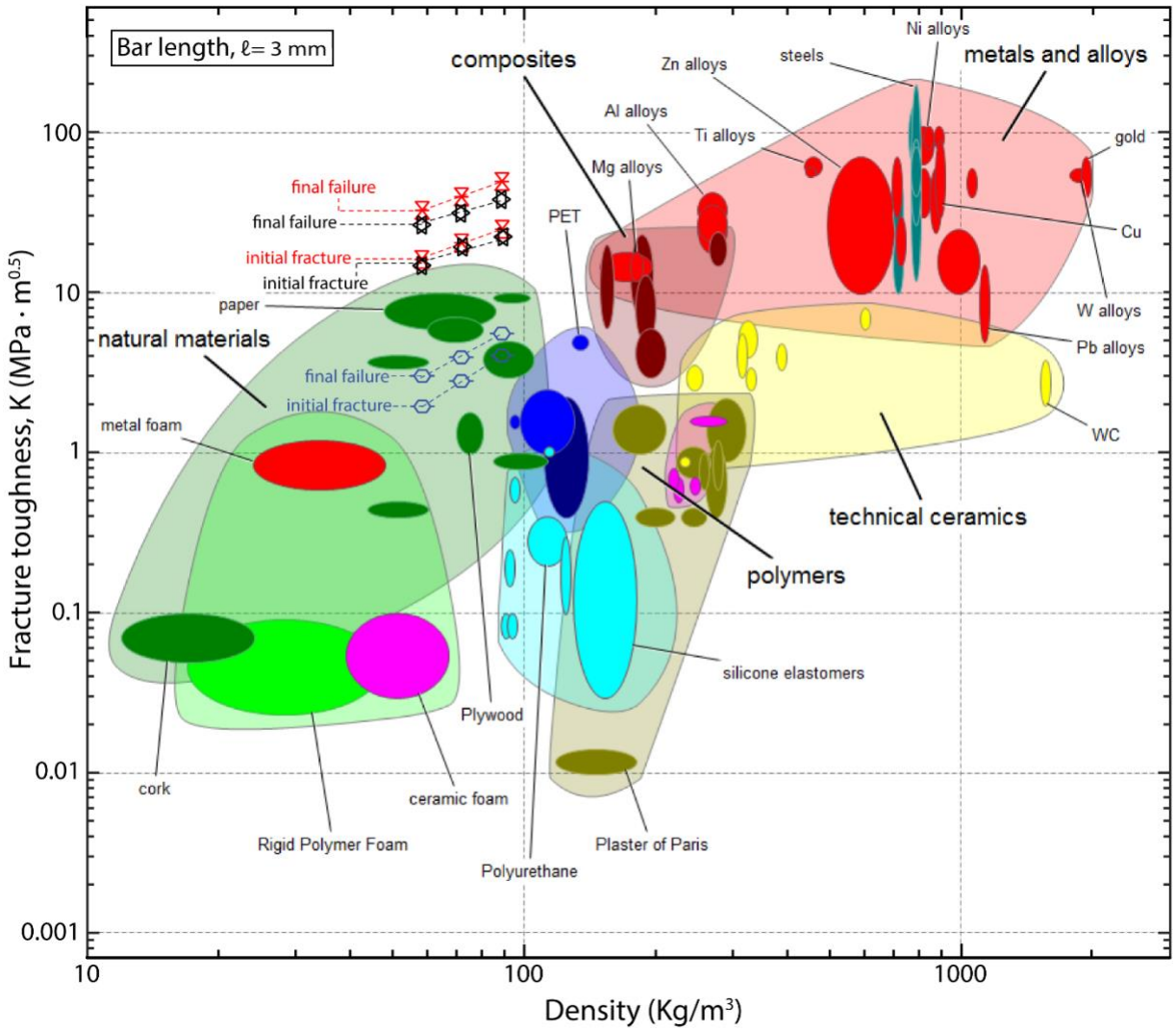

Fig. 4.10 *Material space charts for fracture toughness versus density. Three lattices are shown by their representative unit cell topologies: triangular (red), kagome (black), and hexagonal (blue). The prediction is based on titanium alloy material properties with the bar length, ℓ = 3 mm.*

4.4 Discussion

In the case of elastic brittle base materials, the fracture toughness is governed by linear elastic fracture mechanics (LEFM) and in general depends linearly on the tensile strength of the base material. The fracture toughness of lattices predicted from the proposed numerical approach is in good agreement with solutions derived using boundary layer

analyses for elastic brittle lattices as shown in Fig. 4.7 [108]. The 24% discrepancy in the pre-factor, *D* (see Table 1) for kagome lattices between this work and Fleck and Qiu, 2007 [108] is attributed to different density ranges over which the parameter was fitted ($\bar{\rho}$ = 13% - 20% in the current analyses VS $\bar{\rho}$ = 0.3% - 20% in [108], and the larger sensitivity of the parameter D over the density range in kagome lattices, due to the elastic blunting zone around the crack tip [108].

In the case of elastoplastic constituent materials, the fracture toughness is still governed by LEFM if the plastic region size in front of crack tip is negligible compared to the crack length, i.e., small-scale yielding (SSY); conversely, elasto-plastic fracture mechanics (EPFM) governs if the plastic region size in front of the crack tip grows comparable to the crack length. The simple criterion for the SSY conditions to be satisfied in SENB specimens can be derived by combining the ASTM specification that $a, B > 2.5\left(K_I/\sigma_{ys}\right)^2$ and the expression for the plane strain plastic zone size in a perfectly plastic solid, i.e., $r_p = \frac{1}{3\pi}\left(K_I/\sigma_{ys}\right)^2$, resulting in the condition $a, B > 25r_p$. The plastic region sizes right before initial fracture in three lattices (Fig. 6) reveal that only the hexagonal lattice satisfies the SSY criterion. Hence the initial fracture toughness, K_{JIC}, of hexagonal lattices derived from current numerical approach should be comparable to the results obtained using K-field boundary layer analyses under small-scale yielding conditions in [120]. For this reason, the *D* pre-factors for the hexagonal lattices obtained with the two approaches agree well for hexagonal lattices but deviate for triangular and kagome lattices (Table 4.1). These findings further validate the current numerical approach for elastoplastic materials.

Finally, we emphasize that the numerical approach proposed herein can be easily extended to 3D cellular materials (strut or shell-based) with small modifications on the sample design (number of unit cells, number of elements, degree of isotropy) and boundary conditions. The only essential assumption is that the crack tip must be within the empty space of a unit cell, in order to avoid stress singularity and hence mesh-dependent damage in the finite element analysis. In the case of shell-based cellular materials, care must be taken to ensure the shell surfaces are sufficiently smooth to avoid sharp corners. We recognize two limitations of the proposed approach: (i) SENB specimens can only be used to predict mode-I fracture toughness, and (ii) progressive failure of individual struts can only be properly addressed by using continuum elements (not beam element as done in the current study), with significant increase in computational expense.

4.5 Conclusions

We proposed a versatile numerical approach for fracture toughness and R-curve modeling of both brittle and ductile cellular materials, combining J-integral calculations in SENB specimens and a local maximum strain damage model. The proposed model does not impose small-scale yielding restrictions, and hence does not require exceeding large numbers of unit cells for highly deformable constituent materials. This approach was applied in finite element modeling to investigate fracture toughness (R-curves) of three 2D isotropic lattices: triangular, kagome, and hexagonal lattices, made of both silicon carbide (elastic brittle) and titanium alloy (elastoplastic) constituent materials. First, specimen design studies were systematically conducted in order to extract the required number of unit cells, number of elements per bar and degree of isotropy, in order to ensure that accurate

stress/strain fields are captured around the crack tip. Second, we validated the current numerical approach by comparing the predicted initial fracture toughness in both elastic brittle and small-scale yielding elasto-plastic cases with previous works [108,120]. Finally, we extracted four key results: (i) toughening via topological designs of the lattice architecture seems possible even in elastic brittle lattices; (ii) the power-law scaling relations for initial fracture toughness and toughening coefficients with relative densities only depend on the topology of the lattice, and not the mechanical response of the base material; (iii) triangular lattices outperform both kagome and hexagonal lattices in terms of toughening (R-curve) in the range of $\bar{\rho}$ = 0.13 – 0.2, and (iv) careful design of topology to exploit toughening mechanisms in cellular materials can significantly increase the steady-state fracture toughness that possibly exceed the initial fracture toughness or even the steady-state fracture toughness of the constituent material itself (especially true in the case of brittle base materials).

We emphasize that the strength of the proposed approach lies in its versatility, allowing analysis of both 2D and 3D lattice materials with virtually any topology (both truss and shell-based) and any constituent material behavior, with the only restriction that the crack tip must be contained inside the unit cell. This topological condition could be relaxed with further development. These features make the proposed approach ideally suitable for the toughness calculation of shell-based lattice materials.

CHAPTER 5

Summary and Conclusions

The best approach to design architected cellular materials with superior stiffness, strength and fracture toughness is to synergistically combine optimization of the unit cell topology and exploitation of constituent material size effects at the nanoscale. Traditionally, strut-based topologies have dominated the field. More recently, the interest has shifted to shell-based topologies with minimal surface characteristics. Although more complex in shape and behavior, these shell-based topologies can still be fabricated with the smallest feature size at the nanoscale through advanced additive manufacturing technologies. However, regardless of the topology of choice, upscaling of these architected materials with nanoscale feature sizes remains a incredible challenge. We propose that spinodal decomposition of an appropriate solution followed by material conversion approaches is a possible route for the scalable fabrication of architected materials with shell-based topologies. In this thesis, we fully investigate the mechanical (stiffness and strength) and bio-mechanical (specific surface area and bone growth index) properties of these architected materials and contrast them with those of state-of-the-art strut and shell-based topologies. Although the fracture toughness of spinodal topologies is not investigated in the thesis, we develop a versatile numerical approach that is applicable to 2D or 3D cellular materials (regardless of the topologies) made of elastic brittle or elastoplastic constituent materials, and apply it to obtain the fracture toughness/R-curve in 2D isotropic lattices. In the future, this approach can be extended to calculate the fracture toughness of spinodal topologies. The key conclusions of this work are summarized below:

- Chapter 2 — Spinodal shells derived from the interface of two spinodally decomposing phases are shown to be stochastic minimal surfaces (i.e., surfaces with mean curvatures approximately equal to zero everywhere). Due to such uniform double curvatures, spinodal shells are found to be extremely mechanically efficient, with stiffness and strength on par with or better than many other state-of-the-art periodic strut-based and shell-based topologies, in spite of their intrinsically stochastic nature. Furthermore, spinodal shells are extremely imperfection-insensitive even at ultralow relative densities and can be fabricated in scalable manner, providing a unique opportunity for the development of multi length-scale architected materials.
- Chapter 3 — The biocompatibility of porous metallic implants with spinodal shell (stochastic minimal surface-based design), primitive shell (one of the most common triply periodic minimal surface-based design) and octet lattice (one of the most mechanically efficient periodic truss-based lattices) topologies are investigated. Minimal surface-based topologies clearly outperform strut-based topologies in terms of Young's modulus, specific interfacial surface area, peak stress, and relative bone growth. Out of three implant topologies considered, the spinodal shell topology has the best combinations of properties. In addition, spinodal shells can be scalably fabricated to significantly increase its specific interfacial surface for better bone-implant integration.
- Chapter 4 — A versatile numerical approach based on the J-integral calculation of fracture toughness/R-curve in the SENB specimen with a maximum strain failure criterion is developed. The approach is applied to both elastic brittle and elastoplastic

2D isotropic lattices: triangular, kagome and hexagonal. The current approach is verified by comparing the obtained initial fracture toughness to that obtained in previous studies by boundary layer analyses. We conclude that careful architecture designs can result in toughening even though the constituent material is elastic brittle; in the case of elastoplastic constituent materials, it is possible to obtain a steady-state fracture toughness far greater than the initial fracture toughness or stead-state fracture toughness of the constituent material itself. Finally, we emphasize the versatility of the current numerical approach: It can be applied to obtain fracture toughness of virtually any topologies including 3D shell-based topologies such as TPMS and spinodal shells.

References

[1] N.A. Fleck, V.S. Deshpande, M.F. Ashby, Micro-architectured materials: Past, present and future, Proc. R. Soc. A Math. Phys. Eng. Sci. 466 (2010) 2495–2516. doi:10.1098/rspa.2010.0215.

[2] V.S. Deshpande, N.A. Fleck, M.F. Ashby, Effective properties of the octet-truss lattice material, J. Mech. Phys. Solids. 49 (2001) 1747–1769. doi:10.1016/S0022-5096(01)00010-2.

[3] M.F. Ashby, A.G. Evans, N.A. Fleck, L.J. Gibson, Wadley, H.N.G., J.W. Hutchinson, Metal Foams : A Design Guide Metal Foams : A Design Guide, Butterworth-Heinemann, Woburn, MA, USA, 2000.

[4] L.J. Gibson, M.F. Ashby, Cellular solids, 2nd ed., Cambridge University Press, Cambridge, MA, 1997.

[5] V.S. Deshpande, M.F. Ashby, N.A. Fleck, Foam topology: Bending versus stretching dominated architectures, Acta Mater. 49 (2001) 1035–1040. doi:10.1016/S1359-6454(00)00379-7.

[6] N. a Fleck, An overview of the mechanical properties of foams and periodic lattice materials, Cell. Met. Polym. 2004. (2004) 1–4.

[7] M.. Ashby, The properties of foams and lattices, Philos. Trans. R. Soc. A Math. Phys. Eng. Sci. 364 (2006) 15–30. doi:10.1098/rsta.2005.1678.

[8] M.F. Ashby, The mechanical properties of cellular solids, Metall. Trans. A. 14 (1983) 1755–1769. doi:10.1007/BF02645546.

[9] L.J. Gibson, M.F. Ashby, Cellular Solids: Structure and Properties, Pergamon Press, Oxford, United Kingdom, 1988.

[10] L. Valdevit, S.W. Godfrey, T.A. Schaedler, A.J. Jacobsen, W.B. Carter, Compressive strength of hollow microlattices: Experimental characterization, modeling, and optimal design, J. Mater. Res. 28 (2013) 2461–2473. doi:10.1557/jmr.2013.160.

[11] T.A. Schaedler, A.J. Jacobsen, A. Torrents, A.E. Sorensen, J. Lian, J.R. Greer, L. Valdevit, W.B. Carter, Ultralight Metallic Microlattices, Science (80-.). 334 (2011) 962–965. doi:10.1126/science.1211649.

[12] L.R. Meza, S. Das, J.R. Greer, Strong, lightweight, and recoverable three-dimensional, Science (80-.). 345 (2014) 1322–1326. doi:10.1126/science.1255908.

[13] A. Torrents, T.A. Schaedler, A.J. Jacobsen, W.B. Carter, L. Valdevit, Characterization of nickel-based microlattice materials with structural hierarchy from the nanometer to the millimeter scale, Acta Mater. 60 (2012) 3511–3523. doi:10.1016/j.actamat.2012.03.007.

[14] L. Valdevit, A.J. Jacobsen, J.R. Greer, W.B. Carter, Protocols for the optimal design of multi-functional cellular structures: From hypersonics to micro-architected

materials, J. Am. Ceram. Soc. 94 (2011) 15–34. doi:10.1111/j.1551-2916.2011.04599.x.

[15] J. Bauer, L.R. Meza, T.A. Schaedler, R. Schwaiger, X. Zheng, L. Valdevit, Nanolattices: An Emerging Class of Mechanical Metamaterials, Adv. Mater. 29 (2017) 1–26. doi:10.1002/adma.201701850.

[16] S.M. Pingle, N.A. Fleck, V.S. Deshpande, H.N.G. Wadley, Collapse mechanism maps for the hollow pyramidal core of a sandwich panel under transverse shear, Int. J. Solids Struct. 48 (2011) 3417–3430. doi:10.1016/j.ijsolstr.2011.08.004.

[17] J. Bauer, A. Schroer, R. Schwaiger, O. Kraft, The Impact of Size and Loading Direction on the Strength of Architected Lattice Materials, Adv. Eng. Mater. 18 (2016) 1537–1543. doi:10.1002/adem.201600235.

[18] C.M. Portela, J.R. Greer, D.M. Kochmann, Impact of node geometry on the effective stiffness of non-slender three-dimensional truss lattice architectures, Extrem. Mech. Lett. 22 (2018) 138–148. doi:10.1016/j.eml.2018.06.004.

[19] L. Salari-Sharif, S.W. Godfrey, M. Tootkaboni, L. Valdevit, The effect of manufacturing defects on compressive strength of ultralight hollow microlattices: A data-driven study, Addit. Manuf. 19 (2018) 51–61. doi:10.1016/j.addma.2017.11.003.

[20] S.C. Han, J.W. Lee, K. Kang, A New Type of Low Density Material: Shellular, Adv. Mater. 27 (2015) 5506–5511. doi:10.1002/adma.201501546.

[21] J.B. Berger, H.N.G. Wadley, R.M. Mcmeeking, Mechanical metamaterials at the theoretical limit of isotropic elastic stiffness, Nature. (2017) 1–12. doi:10.1038/nature21075.

[22] Meeks, Perez, The classical theory of minimal surfaces, Bull. Amer. Math. Soc. 48 (2011) 325–407. doi:10.1090/S0273-0979-2011-01334-9.

[23] H.A. Schwarz, Gesammelte Mathematische Abhandlungen, Springer, Berlin, 1890.

[24] S. Hyde, T. Landh, S. Lidin, B.W. Ninham, S. Andersson, K. Larsson, The Language of Shape, Elsevier, Danvers, Ma, 1996.

[25] A.H. Schoen, Infinite Periodic Minimal Surfaces without Self-Intersections, 1970.

[26] S. Rajagopalan, R.A. Robb, Schwarz meets Schwann: Design and fabrication of biomorphic and durataxic tissue engineering scaffolds, Med. Image Anal. 10 (2006) 693–712. doi:10.1016/j.media.2006.06.001.

[27] S.C. Han, J.M. Choi, G. Liu, K. Kang, A microscopic shell structure with schwarz's D-Surface, Sci. Rep. 7 (2017) 1–8. doi:10.1038/s41598-017-13618-3.

[28] B.D. Nguyen, S.C. Han, Y.C. Jung, K. Kang, Design of the P-surfaced shellular, an ultra-low density material with micro-architecture, Comput. Mater. Sci. 139 (2017) 162–178. doi:10.1016/j.commatsci.2017.07.025.

[29] J.W. Hutchinson, J.M.T. Thompson, Imperfections and Energy Barriers in Shell

Buckling, Int. J. Solids Struct. (2018) 1–32.

[30] J. Bauer, A. Schroer, R. Schwaiger, O. Kraft, Approaching theoretical strength in glassy carbon nanolattices, Nat. Mater. 15 (2016) 438–443. doi:10.1038/nmat4561.

[31] X. Zheng, W. Smith, J. Jackson, B. Moran, H. Cui, D. Chen, J. Ye, N. Fang, N. Rodriguez, T. Weisgraber, C.M. Spadaccini, Multiscale metallic metamaterials, Nat. Mater. 15 (2016) 1100–1106. doi:10.1038/nmat4694.

[32] S.N. Khaderi, M.R.J. Scherer, C.E. Hall, U. Steiner, U. Ramamurty, N.A. Fleck, V.S. Deshpande, The indentation response of Nickel nano double gyroid lattices, Extrem. Mech. Lett. 10 (2017) 15–23. doi:10.1016/j.eml.2016.08.006.

[33] S.N. Khaderi, V.S. Deshpande, N.A. Fleck, The stiffness and strength of the gyroid lattice, Int. J. Solids Struct. 51 (2014) 3866–3877. doi:10.1016/j.ijsolstr.2014.06.024.

[34] J. Bishop-Moser, C.M. Spadaccini, C. Andres, Metamaterials Manufacturing - Pathways to Industrial Competitiveness, MForesight, Ann Arbor, MI, 2018.

[35] S. Stewart, S.J. Bryant, J. Ahn, K.D. Hankenson, Bone Regeneration, in: Transl. Regen. Med., Elsevier, 2015: pp. 313–333. doi:10.1016/B978-0-12-410396-2.00024-4.

[36] A. Wiese, H.C. Pape, Bone Defects Caused by High-energy Injuries, Bone Loss, Infected Nonunions, and Nonunions, Orthop. Clin. North Am. 41 (2010) 1–4. doi:10.1016/j.ocl.2009.07.003.

[37] A. Schindeler, M.M. McDonald, P. Bokko, D.G. Little, Bone remodeling during fracture repair: The cellular picture, Semin. Cell Dev. Biol. 19 (2008) 459–466. doi:10.1016/j.semcdb.2008.07.004.

[38] J. Sheen, V. Garla, Fracture Healing Overview, StatPearls Publishing, Treasure Island, Florida, 2020. https://www.ncbi.nlm.nih.gov/books/NBK551678/.

[39] J. Currey, Bones: Structure and Mechanics, Princeton University Press, 2002.

[40] X. Wang, S. Xu, S. Zhou, W. Xu, M. Leary, P. Choong, M. Qian, M. Brandt, Y.M. Xie, Topological design and additive manufacturing of porous metals for bone scaffolds and orthopaedic implants: A review, Biomaterials. 83 (2016) 127–141. doi:10.1016/j.biomaterials.2016.01.012.

[41] V. Mouriño, A.R. Boccaccini, Bone tissue engineering therapeutics: Controlled drug delivery in three-dimensional scaffolds, J. R. Soc. Interface. 7 (2010) 209–227. doi:10.1098/rsif.2009.0379.

[42] S. Bose, S. Vahabzadeh, A. Bandyopadhyay, Bone tissue engineering using 3D printing, Mater. Today. 16 (2013) 496–504. doi:10.1016/j.mattod.2013.11.017.

[43] H. Seitz, W. Rieder, S. Irsen, B. Leukers, C. Tille, Three-dimensional printing of porous ceramic scaffolds for bone tissue engineering, J. Biomed. Mater. Res. - Part B Appl. Biomater. 74 (2005) 782–788. doi:10.1002/jbm.b.30291.

[44] A.C. Jones, C.H. Arns, A.P. Sheppard, D.W. Hutmacher, B.K. Milthorpe, M.A. Knackstedt,

Assessment of bone ingrowth into porous biomaterials using MICRO-CT, Biomaterials. 28 (2007) 2491–2504. doi:10.1016/j.biomaterials.2007.01.046.

[45] T. Kim, C.W. See, X. Li, D. Zhu, Orthopedic implants and devices for bone fractures and defects: Past, present and perspective, Eng. Regen. 1 (2020) 6–18. doi:10.1016/j.engreg.2020.05.003.

[46] P. Joly, G.N. Duda, M. Schöne, P.B. Welzel, U. Freudenberg, C. Werner, A. Petersen, Geometry-Driven Cell Organization Determines Tissue Growths in Scaffold Pores: Consequences for Fibronectin Organization, PLoS One. 8 (2013) 1–11. doi:10.1371/journal.pone.0073545.

[47] S. Arabnejad, R. Burnett Johnston, J.A. Pura, B. Singh, M. Tanzer, D. Pasini, High-strength porous biomaterials for bone replacement: A strategy to assess the interplay between cell morphology, mechanical properties, bone ingrowth and manufacturing constraints, Acta Biomater. 30 (2016) 345–356. doi:10.1016/j.actbio.2015.10.048.

[48] V. Karageorgiou, D. Kaplan, Porosity of 3D biomaterial scaffolds and osteogenesis, Biomaterials. 26 (2005) 5474–5491. doi:10.1016/j.biomaterials.2005.02.002.

[49] G.H. Billström, A.W. Blom, S. Larsson, A.D. Beswick, Application of scaffolds for bone regeneration strategies: Current trends and future directions, Injury. 44 (2013) S28–S33. doi:10.1016/S0020-1383(13)70007-X.

[50] S.J. Hollister, W.L. Murphy, Scaffold translation: Barriers between concept and clinic, Tissue Eng. - Part B Rev. 17 (2011) 459–474. doi:10.1089/ten.teb.2011.0251.

[51] B. Gervais, A. Vadean, M. Raison, M. Brochu, Failure analysis of a 316L stainless steel femoral orthopedic implant, Case Stud. Eng. Fail. Anal. 5–6 (2016) 30–38. doi:10.1016/j.csefa.2015.12.001.

[52] S. Wu, X. Liu, K.W.K. Yeung, C. Liu, X. Yang, Biomimetic porous scaffolds for bone tissue engineering, Mater. Sci. Eng. R Reports. 80 (2014) 1–36. doi:10.1016/j.mser.2014.04.001.

[53] C. Boyle, I.Y. Kim, Comparison of different hip prosthesis shapes considering micro-level bone remodeling and stress-shielding criteria using three-dimensional design space topology optimization, J. Biomech. 44 (2011) 1722–1728. doi:10.1016/j.jbiomech.2011.03.038.

[54] R. Rahmanian, N. Shayesteh Moghaddam, C. Haberland, D. Dean, M. Miller, M. Elahinia, Load bearing and stiffness tailored NiTi implants produced by additive manufacturing: a simulation study, Behav. Mech. Multifunct. Mater. Compos. 2014. 9058 (2014) 905814. doi:10.1117/12.2048948.

[55] T.T. Roberts, A.J. Rosenbaum, Bone grafts, bone substitutes and orthobiologics the bridge between basic science and clinical advancements in fracture healing, Organogenesis. 8 (2012) 114–124. doi:10.4161/org.23306.

[56] M. Geetha, A.K. Singh, R. Asokamani, A.K. Gogia, Ti based biomaterials, the ultimate

choice for orthopaedic implants - A review, Prog. Mater. Sci. 54 (2009) 397–425. doi:10.1016/j.pmatsci.2008.06.004.

[57] G.M. Raghavendra, K. Varaprasad, T. Jayaramudu, Biomaterials: Design, Development and Biomedical Applications, Elsevier Inc., 2015. doi:10.1016/B978-0-323-32889-0.00002-9.

[58] A. WOESZ, S.M. BEST, 6 - Cellular response to bioceramics, in: L.B.T.-C.R. to B. Di Silvio (Ed.), Woodhead Publ. Ser. Biomater., Woodhead Publishing, 2009: pp. 136–155. doi:https://doi.org/10.1533/9781845695477.1.136.

[59] K.S. KATTI, D. VERMA, D.R. KATTI, 4 - Materials for joint replacement, in: P.A.B.T.-J.R.T. Revell (Ed.), Woodhead Publ. Ser. Biomater., Woodhead Publishing, 2008: pp. 81–104. doi:https://doi.org/10.1533/9781845694807.1.81.

[60] W. Jin, G. Wu, A. Gao, H. Feng, X. Peng, P.K. Chu, Hafnium-implanted WE43 magnesium alloy for enhanced corrosion protection and biocompatibility, Surf. Coatings Technol. 306 (2016) 11–15. doi:10.1016/j.surfcoat.2016.02.055.

[61] P. Wen, M. Voshage, L. Jauer, Y. Chen, Y. Qin, R. Poprawe, J.H. Schleifenbaum, Laser additive manufacturing of Zn metal parts for biodegradable applications: Processing, formation quality and mechanical properties, Mater. Des. 155 (2018) 36–45. doi:10.1016/j.matdes.2018.05.057.

[62] Y. Li, H. Jahr, K. Lietaert, P. Pavanram, A. Yilmaz, L.I. Fockaert, M.A. Leeflang, B. Pouran, Y. Gonzalez-Garcia, H. Weinans, J.M.C. Mol, J. Zhou, A.A. Zadpoor, Additively manufactured biodegradable porous iron, Acta Biomater. 77 (2018) 380–393. doi:10.1016/j.actbio.2018.07.011.

[63] M. Long, H.. Rack, Titanium alloys in total joint replacement—a materials science perspective, Biomaterials. 19 (1998) 1621–1639. doi:10.1016/S0142-9612(97)00146-4.

[64] M. Niinomi, Recent research and development in titanium alloys for biomedical applications and healthcare goods, Sci. Technol. Adv. Mater. 4 (2003) 445–454. doi:10.1016/j.stam.2003.09.002.

[65] M. Abdel-Hady Gepreel, M. Niinomi, Biocompatibility of Ti-alloys for long-term implantation, J. Mech. Behav. Biomed. Mater. 20 (2013) 407–415. doi:10.1016/j.jmbbm.2012.11.014.

[66] A. Goharian, M.R. Abdullah, Bioinert Metals (Stainless Steel, Titanium, Cobalt Chromium), Elsevier Inc., 2017. doi:10.1016/B978-0-12-804634-0.00007-0.

[67] M.J. Cross, G.J. Roger, J. Spycher, Cementless fixation techniques and challenges in joint replacement, Jt. Replace. Technol. (2014) 186–211. doi:10.1533/9780857098474.2.186.

[68] A. Wahab, Skeleton System, Science4Fun. (2020). https://science4fun.info/skeletal-system/.

[69] OpenTax College, Anatomy & physiology, OpenTax CNX, Houston, TX, 2013. https://openstax.org/details/books/anatomy-and-physiology.

[70] G. Li, L. Wang, W. Pan, F. Yang, W. Jiang, X. Wu, X. Kong, K. Dai, Y. Hao, In vitro and in vivo study of additive manufactured porous Ti6Al4V scaffolds for repairing bone defects, Sci. Rep. 6 (2016) 1–11. doi:10.1038/srep34072.

[71] P. Ouyang, H. Dong, X. He, X. Cai, Y. Wang, J. Li, H. Li, Z. Jin, Hydromechanical mechanism behind the effect of pore size of porous titanium scaffolds on osteoblast response and bone ingrowth, Mater. Des. 183 (2019) 108151. doi:10.1016/j.matdes.2019.108151.

[72] S.J. Hollister, Porous scaffold design for tissue engineering, Nat. Mater. 4 (2005) 518–524. doi:10.1038/nmat1421.

[73] Y. Wang, S. Arabnejad, M. Tanzer, D. Pasini, Hip implant design with three-dimensional porous architecture of optimized graded density, J. Mech. Des. Trans. ASME. 140 (2018) 1–13. doi:10.1115/1.4041208.

[74] A. Rahimizadeh, Z. Nourmohammadi, S. Arabnejad, M. Tanzer, D. Pasini, Porous architected biomaterial for a tibial-knee implant with minimum bone resorption and bone-implant interface micromotion, J. Mech. Behav. Biomed. Mater. 78 (2018) 465–479. doi:10.1016/j.jmbbm.2017.11.041.

[75] R. Hedayati, A.M. Leeflang, A.A. Zadpoor, Additively manufactured metallic pentamode meta-materials, Appl. Phys. Lett. 110 (2017). doi:10.1063/1.4977561.

[76] D. Mahmoud, M.A. Elbestawi, Selective laser melting of porosity graded lattice structures for bone implants, Int. J. Adv. Manuf. Technol. 100 (2019) 2915–2927. doi:10.1007/s00170-018-2886-9.

[77] Y.K. Ahn, H.G. Kim, H.K. Park, G.H. Kim, K.H. Jung, C.W. Lee, W.Y. Kim, S.H. Lim, B.S. Lee, Mechanical and microstructural characteristics of commercial purity titanium implants fabricated by electron-beam additive manufacturing, Mater. Lett. 187 (2017) 64–67. doi:10.1016/j.matlet.2016.10.064.

[78] A. Mohammadhosseini, S.H. Masood, D. Fraser, M. Jahedi, Dynamic compressive behaviour of Ti-6Al-4V alloy processed by electron beam melting under high strain rate loading, Adv. Manuf. 3 (2015) 232–243. doi:10.1007/s40436-015-0119-0.

[79] D.K. Pattanayak, A. Fukuda, T. Matsushita, M. Takemoto, S. Fujibayashi, K. Sasaki, N. Nishida, T. Nakamura, T. Kokubo, Bioactive Ti metal analogous to human cancellous bone: Fabrication by selective laser melting and chemical treatments, Acta Biomater. 7 (2011) 1398–1406. doi:10.1016/j.actbio.2010.09.034.

[80] J. Parthasarathy, B. Starly, S. Raman, A. Christensen, Mechanical evaluation of porous titanium (Ti6Al4V) structures with electron beam melting (EBM), J. Mech. Behav. Biomed. Mater. 3 (2010) 249–259. doi:10.1016/j.jmbbm.2009.10.006.

[81] S.M. Ahmadi, S.A. Yavari, R. Wauthle, B. Pouran, J. Schrooten, H. Weinans, A.A. Zadpoor, Additively manufactured open-cell porous biomaterials made from six

different space-filling unit cells: The mechanical and morphological properties, Materials (Basel). 8 (2015) 1871–1896. doi:10.3390/ma8041871.

[82] Ó.L. Rodríguez-Montaño, C.J. Cortés-Rodríguez, A.E. Uva, M. Fiorentino, M. Gattullo, G. Monno, A. Boccaccio, Comparison of the mechanobiological performance of bone tissue scaffolds based on different unit cell geometries, J. Mech. Behav. Biomed. Mater. 83 (2018) 28–45. doi:10.1016/j.jmbbm.2018.04.008.

[83] P.F. Egan, V.C. Gonella, M. Engensperger, S.J. Ferguson, K. Shea, Computationally designed lattices with tuned properties for tissue engineering using 3D printing, PLoS One. 12 (2017) 1–20. doi:10.1371/journal.pone.0182902.

[84] P. Heinl, L. Müller, C. Körner, R.F. Singer, F.A. Müller, Cellular Ti-6Al-4V structures with interconnected macro porosity for bone implants fabricated by selective electron beam melting, Acta Biomater. 4 (2008) 1536–1544. doi:10.1016/j.actbio.2008.03.013.

[85] F. Brenne, T. Niendorf, H.J. Maier, Additively manufactured cellular structures: Impact of microstructure and local strains on the monotonic and cyclic behavior under uniaxial and bending load, J. Mater. Process. Technol. 213 (2013) 1558–1564. doi:10.1016/j.jmatprotec.2013.03.013.

[86] K. Lietaert, A. Cutolo, D. Boey, B. Van Hooreweder, Fatigue life of additively manufactured Ti6Al4V scaffolds under tension-tension, tension-compression and compression-compression fatigue load, Sci. Rep. 8 (2018) 1–9. doi:10.1038/s41598-018-23414-2.

[87] M.G. Lee, J.W. Lee, S.C. Han, K. Kang, Mechanical analyses of "shellular", an ultralow-density material, Acta Mater. 103 (2016) 595–607. doi:10.1016/j.actamat.2015.10.040.

[88] C. Yan, L. Hao, A. Hussein, P. Young, Ti-6Al-4V triply periodic minimal surface structures for bone implants fabricated via selective laser melting, J. Mech. Behav. Biomed. Mater. 51 (2015) 61–73. doi:10.1016/j.jmbbm.2015.06.024.

[89] F. Liu, D.Z. Zhang, P. Zhang, M. Zhao, S. Jafar, Mechanical properties of optimized diamond lattice structure for bone scaffolds fabricated via selective laser melting, Materials (Basel). 11 (2018). doi:10.3390/ma11030374.

[90] O. Al-ketan, R. Rezgui, R. Rowshan, H. Du, N.X. Fang, Microarchitected Stretching-Dominated Mechanical Metamaterials with Minimal Surface Topologies, 1800029 (2018) 1–15. doi:10.1002/adem.201800029.

[91] D.W. Abueidda, R.K. Abu Al-Rub, A.S. Dalaq, D.W. Lee, K.A. Khan, I. Jasiuk, Effective conductivities and elastic moduli of novel foams with triply periodic minimal surfaces, Mech. Mater. 95 (2016) 102–115. doi:10.1016/j.mechmat.2016.01.004.

[92] W. Yang, J. An, C.K. Chua, K. Zhou, Acoustic absorptions of multifunctional polymeric cellular structures based on triply periodic minimal surfaces fabricated by stereolithography, Virtual Phys. Prototyp. 15 (2020) 242–249.

doi:10.1080/17452759.2020.1740747.

[93] X.C. Ye, X.C. Lin, J.Y. Xiong, H.H. Wu, G.W. Zhao, D. Fang, Electrical properties of 3D printed graphite cellular lattice structures with triply periodic minimal surface architectures, Mater. Res. Express. 6 (2019). doi:10.1088/2053-1591/ab569b.

[94] A. Ataee, Y. Li, D. Fraser, G. Song, C. Wen, Anisotropic Ti-6Al-4V gyroid scaffolds manufactured by electron beam melting (EBM) for bone implant applications, Mater. Des. 137 (2018) 345–354. doi:10.1016/j.matdes.2017.10.040.

[95] A. Ataee, Y. Li, M. Brandt, C. Wen, Ultrahigh-strength titanium gyroid scaffolds manufactured by selective laser melting (SLM) for bone implant applications, Acta Mater. 158 (2018) 354–368. doi:10.1016/j.actamat.2018.08.005.

[96] F.S.L. Bobbert, K. Lietaert, A.A. Eftekhari, B. Pouran, S.M. Ahmadi, H. Weinans, A.A. Zadpoor, Additively manufactured metallic porous biomaterials based on minimal surfaces: A unique combination of topological, mechanical, and mass transport properties, Acta Biomater. 53 (2017) 572–584. doi:10.1016/j.actbio.2017.02.024.

[97] Z. Hashin, S. Shtrikman, A variational approach to the theory of the elastic behaviour of multiphase materials, J. Mech. Phys. Solids. 11 (1963) 127–140. doi:10.1016/0022-5096(63)90060-7.

[98] P.M. Suquet, Overall potentials and extremal surfaces of power law or ideally plastic composites, J. Mech. Phys. Solids. 41 (1993) 981–1002. doi:10.1016/0022-5096(93)90051-G.

[99] P.P. Castaneda, G. Debotton, On the Homogenized Zield Strength of Two-Phase Composites, Proc. R. Soc. Lond. A. 438 (1992) 419–431. doi:10.1021/bi051624q.

[100] S.K. Maiti, M.F. Ashby, L.J. Gibson, Fracture toughness of brittle cellular solids, Scr. Metall. 18 (1984) 213–217. doi:10.1016/0036-9748(84)90510-6.

[101] J.S. Huang, J.Y. Lin, Mixed-mode fracture of brittle cellular materials, J. Mater. Sci. 31 (1996) 2647–2652. doi:10.1007/BF00687295.

[102] N.A. Fleck, J.W. Hutchinson, Strain Gradient plasticity, Adv. Appl. Mech. 33 (1996) 295–361.

[103] N.A. Fleck, G.M. Muller, M.F. Ashby, J.W. Hutchinson, Strain gradient plasticity: Theory and experiment, Acta Metall. Mater. 42 (1994) 475–487. doi:10.1016/0956-7151(94)90502-9.

[104] N.A. Fleck, J.W. Hutchinson, A phenomenological theory for strain gradient effects in plasticity, Hazard. Waste Consult. 24 (1993) 3.1-3.2. doi:10.1016/0022-5096(93)90072-N.

[105] C.B. Banks, M. Sokolowski, On certain two-dimensional applications of the couple stress theory, Int. J. Solids Struct. 4 (1968) 15–29. doi:10.1016/0020-7683(68)90030-9.

[106] Z.P. Bazant, M. Christensen, Analogy between micropolar continuum and grid

frameworks under initial stress, 8 (2011). doi:10.1103/PhysRevD.86.015023.

[107] J.Y. Chen, Y. Huang, M. Ortiz, Fracture analysis of cellular materials: A strain gradient model, J. Mech. Phys. Solids. 46 (1998) 789–828. doi:10.1016/S0022-5096(98)00006-4.

[108] N.A. Fleck, X. Qiu, The damage tolerance of elastic – brittle , two-dimensional isotropic lattices, 55 (2007) 562–588. doi:10.1016/j.jmps.2006.08.004.

[109] I. Quintana-Alonso, N.A. Fleck, Major accomplishments in composite materials and sandwich structures: anthology of ONR sponsored research, Springer, Heidelberg, New York, 2009. doi:10.1007/978-90-481-3141-9.

[110] J.S. Huang, L.J. Gibson, Fracture toughness of brittle foams, Acta Metall. Mater. 39 (1991) 1627–1636. doi:10.1016/0956-7151(91)90250-5.

[111] I. Quintana-Alonso, N.A. Fleck, Damage tolerance of an elastic-brittle diamond-celled honeycomb, 56 (2007) 693–696. doi:10.1016/j.scriptamat.2006.12.027.

[112] I. Quintana-alonso, S.P. Mai, N.A. Fleck, D.C.H. Oakes, M. V Twigg, The fracture toughness of a cordierite square lattice, Acta Mater. 58 (2010) 201–207. doi:10.1016/j.actamat.2009.08.069.

[113] J.S. Huang, M.S. Chiang, Effects of microstructure, specimen, and loading geometries on KIC of brittle honeycombs, 54 (1996).

[114] M.F. Kanninen, C.H. Popelar, Advanced Fracture Mechanics, OUP, Oxford, UK, 1985.

[115] M.L. Williams, On the stress distribution at the base of a stationary crack, J. Appl. Mech. 24 (1957) 109–114. doi:10.1115/1.3640470.

[116] I. Schmidt, N.A. Fleck, Ductile fracture of two-dimensional cellular structures, Int. J. Fract. 111 (2001) 327–342. doi:10.1023/A:1012248030212.

[117] N.E.R. Romijn, N.A. Fleck, The fracture toughness of planar lattices: Imperfection sensitivity, J. Mech. Phys. Solids. 55 (2007) 2538–2564. doi:10.1016/j.jmps.2007.04.010.

[118] G.C. Sih, P.C. Paris, G.R. Irwin, On Cracks in Rectilinearly Anisotropic Bodies, Int. J. Fract. Mech. 59 (1965) 1014. doi:10.1017/S0003055400080564.

[119] I. Christodoulou, P.J. Tan, Crack initiation and fracture toughness of random Voronoi honeycombs, Eng. Fract. Mech. 104 (2013) 140–161. doi:10.1016/j.engfracmech.2013.03.017.

[120] H.C. Tankasala, V.S. Deshpande, N.A. Fleck, 2013 Koiter Medal Paper: Crack-Tip Fields and Toughness of Two-Dimensional Elastoplastic Lattices, J. Appl. Mech. 82 (2015) 091004. doi:10.1115/1.4030666.

[121] J.W. Cahn, On spinodal decomposition, Acta Metall. 9 (1961) 795–801. doi:10.1016/0001-6160(61)90182-1.

[122] H. Jinnai, T. Koga, Y. Nishikawa, T. Hashimoto, S. Hyde, Curvature Determination of Spinodal Interface in a Condensed Matter System, Phys. Rev. Lett. 78 (1997) 2248–2251. doi:10.1103/PhysRevLett.78.2248.

[123] A.M. Hodge, J. Biener, J.R. Hayes, P.M. Bythrow, C.A. Volkert, A. V. Hamza, Scaling equation for yield strength of nanoporous open-cell foams, Acta Mater. 55 (2007) 1343–1349. doi:10.1016/j.actamat.2006.09.038.

[124] M.N. Lee, A. Mohraz, Bicontinuous macroporous materials from bijel templates, Adv. Mater. 22 (2010) 4836–4841. doi:10.1002/adma.201001696.

[125] M.N. Lee, A. Mohraz, Hierarchically porous silver monoliths from colloidal bicontinuous interfacially jammed emulsion gels, J. Am. Chem. Soc. 133 (2011) 6945–6947. doi:10.1021/ja201650z.

[126] M.N. Lee, J.H.J. Thijssen, J.A. Witt, P.S. Clegg, A. Mohraz, Making a robust interfacial scaffold: Bijel rheology and its link to processability, Adv. Funct. Mater. 23 (2013) 417–423. doi:10.1002/adfm.201201090.

[127] D.A. Porter, K.E. Easterling, M.Y. Sherif, Phase Transformations in Metals and Alloys, CRC Press, 1981.

[128] J. Biener, A. Wittstock, L.A. Zepeda-Ruiz, M.M. Biener, V. Zielasek, D. Kramer, R.N. Viswanath, J. Weissmüller, M. Bäumer, A. V. Hamza, Surface-chemistry-driven actuation in nanoporous gold, Nat. Mater. 8 (2009) 47–51. doi:10.1038/nmat2335.

[129] D.A. Crowson, D. Farkas, S.G. Corcoran, Geometric relaxation of nanoporous metals: The role of surface relaxation, Scr. Mater. 56 (2007) 919–922. doi:10.1016/j.scriptamat.2007.02.017.

[130] D.A. Crowson, D. Farkas, S.G. Corcoran, Mechanical stability of nanoporous metals with small ligament sizes, Scr. Mater. 61 (2009) 497–499. doi:10.1016/j.scriptamat.2009.05.005.

[131] J.W. Cahn, J.E. Hilliard, Free Energy of a Nonuniform System. I. Interfacial Free Energy, J. Chem. Phys. 28 (1958) 258–267. doi:10.1063/1.1744102.

[132] X.-Y. Sun, G.-K. Xu, X. Li, X.-Q. Feng, H. Gao, Mechanical properties and scaling laws of nanoporous gold, J. Appl. Phys. 113 (2013) 023505. doi:10.1063/1.4774246.

[133] Y. Kwon, K. Thornton, P.W. Voorhees, Morphology and topology in coarsening of domains via non-conserved and conserved dynamics, Philos. Mag. 90 (2010) 317–335. doi:10.1080/14786430903260701.

[134] H.Y.Ni.T.I.T.Ni. Jinnai, Emerging Technologies for the 3D Analysis of Polymer Structures, Adv. Polym. Sci. 171 (2004) 137–194. doi:10.1007/b13016.

[135] A. Baldan, Progress in Ostwald ripening theories and their applications in nickel-base super alloys, J. Mater. Sci. 37 (2002) 2379–2405. doi:10.1023/A:1015408116016.

[136] ASTM D695-15, Standard Test Method for Compressive Properties of Rigid Plastics, West Conshohocken, PA, 2008. doi:10.1520/D0695-15.2.

[137] L.R. Meza, A.J. Zelhofer, N. Clarke, A.J. Mateos, D.M. Kochmann, J.R. Greer, Resilient 3D hierarchical architected metamaterials, Proc. Natl. Acad. Sci. 112 (2015) 11502–11507. doi:10.1073/pnas.1509120112.

[138] X.Y. Zheng, H. Lee, T.H. Weisgraber, M. Shusteff, J. Deotte, E.B. Duoss, J.D. Kuntz, M.M. Biener, Q. Ge, J.A. Jackson, S.O. Kucheyev, N.X. Fang, C.M. Spadaccini, Ultralight, ultrastiff mechanical metamaterials, Science (80-.). 344 (2014) 1373–1378. doi:10.1126/science.1252291.

[139] A.M. Schwartzberg, D. Olynick, Complex Materials by Atomic Layer Deposition, Adv. Mater. 27 (2015) 5778–5784. doi:10.1002/adma.201500699.

[140] G.O. Mallory, J.B. Hajdu, Electroless Plating: Fundamentals and Applications, 1st ed., William Andrew Publishing, New York, USA, 1990.

[141] M.-T. Hsieh, B. Endo, Y. Zhang, J. Bauer, L. Valdevit, The mechanical response of cellular materials with spinodal topologies, J. Mech. Phys. Solids. 125 (2019) 401–419. doi:10.1016/J.JMPS.2019.01.002.

[142] A. Guell Izard, J. Bauer, C. Crook, V. Turlo, L. Valdevit, Ultrahigh Energy Absorption Multifunctional Spinodal Nanoarchitectures, Small. 466 (2019) 1903834–1903838.

[143] A.E. Garcia, C.S. Wang, R.N. Sanderson, K.M. McDevitt, Y. Zhang, L. Valdevit, D.R. Mumm, A. Mohraz, R. Ragan, Scalable synthesis of gyroid-inspired freestanding three-dimensional graphene architectures, Nanoscale Adv. 350 (2019) 1508–1513.

[144] I. Maskery, L. Sturm, A.O. Aremu, A. Panesar, C.B. Williams, C.J. Tuck, R.D. Wildman, I.A. Ashcroft, R.J.M. Hague, Insights into the mechanical properties of several triply periodic minimal surface lattice structures made by polymer additive manufacturing, Polymer (Guildf). 152 (2018) 62–71. doi:10.1016/j.polymer.2017.11.049.

[145] S.B.G. Blanquer, M. Werner, M. Hannula, S. Sharifi, G.P.R. Lajoinie, D. Eglin, J. Hyttinen, A.A. Poot, D.W. Grijpma, Surface curvature in triply-periodic minimal surface architectures as a distinct design parameter in preparing advanced tissue engineering scaffolds, Biofabrication. 9 (2017). doi:10.1088/1758-5090/aa6553.

[146] Hsieh, Meng-Ting (2020), “Spinodal solid and shell CAD files in STL and Abaqus input file format”, Mendeley Data, V2, doi: 10.17632/84cg6f23b2.2. http://dx.doi.org/10.17632/84cg6f23b2.2.

[147] M.-T. Hsieh, L. Valdevit, Minisurf – A minimal surface generator for finite element modeling and additive manufacturing, Softw. Impacts. 6 (2020) 100026. doi:10.1016/j.simpa.2020.100026.

[148] L. Bai, C. Gong, X. Chen, Y. Sun, J. Zhang, L. Cai, S. Zhu, S.Q. Xie, Additive manufacturing of customized metallic orthopedic implants: Materials, structures, and surface modifications, Metals (Basel). 9 (2019). doi:10.3390/met9091004.

[149] M. Tanaka, T. Adachi, Model and Simulation of Bone Remodeling Considering Residual Stress, Springer, Tokyo, 1996. doi:10.1007/978-4-431-66951-7_1.

[150] J.Y. Rho, R.B. Ashman, C.H. Turner, Young's modulus of trabecular and cortical bone material: Ultrasonic and microtensile measurements, J. Biomech. 26 (1993) 111–119. doi:10.1016/0021-9290(93)90042-D.

[151] H.H. Bayraktar, E.F. Morgan, G.L. Niebur, G.E. Morris, E.K. Wong, T.M. Keaveny, Comparison of the elastic and yield properties of human femoral trabecular and cortical bone tissue, J. Biomech. 37 (2004) 27–35. doi:10.1016/S0021-9290(03)00257-4.

[152] G.M. Erickson, J. Catanese, T.M. Keaveny, Evolution of the biomechanical material properties of the femur, Anat. Rec. 268 (2002) 115–124. doi:10.1002/ar.10145.

[153] J. Currey, G. Butler, The mechanical properties of bone tissue in children, J Bone Jt. Surg Am. 57 (1975) 810–814.

[154] M.J. Hossain, M.M. Rahman, M. Alam, In vivo measurement of mechanical properties of human long bone by using sonic sound, AIP Conf. Proc. 1754 (2016). doi:10.1063/1.4958354.

[155] A. Özkan, Y. Kişioğlu, The rotational loading capacity and effects of fibula on lower exterimity, 2 (2013) 138–143. www.journaleras.com.

[156] J.B. Park, Structure-Property Relationships of Biological Materials, Springer, Boston, 1979. doi:https://doi.org/10.1007/978-1-4684-3423-1_7.

[157] U.N. Manganyi, K. Mpofu, Biological considerations in the structural design of smart prosthetics, (2011). doi:10.13140/2.1.1523.9683.

[158] R.A. Martínez-Celorio, R. González-Peña, R. Cibrián, R. Salvador, M.F. Mínguez, L. Martí-López, Young's modulus measurement of the radius bone using a shearing interferometer with carrier fringes, Opt. Lasers Eng. 48 (2010) 727–731. doi:10.1016/j.optlaseng.2010.03.001.

[159] M.R. Bosisio, M. Talmant, W. Skalli, P. Laugier, D. Mitton, Apparent Young's modulus of human radius using inverse finite-element method, J. Biomech. 40 (2007) 2022–2028. doi:10.1016/j.jbiomech.2006.09.018.

[160] T. Motoshima, Studies on the strength of bending of human long extremity bones, Jkyoto Pref Med Univ. 68 (1960) 1377–1397.

[161] D.T. Reilly, A.H. Burstein, V.H. Frankel, The elastic modulus for bone, J. Biomech. 7 (1974). doi:10.1016/0021-9290(74)90018-9.

[162] D.T. Reilly, A.H. Burstein, The elastic and ultimate properties of compact bone tissue, J. Biomech. 8 (1975). doi:10.1016/0021-9290(75)90075-5.

[163] H.S. Alghamdi, Methods to improve osseointegration of dental implants in low quality (type-IV) bone: An overview, J. Funct. Biomater. 9 (2018). doi:10.3390/jfb9010007.

[164] R. Gilbert Triplett, U. Frohberg, N. Sykaras, R.D. Woody, R.G. Triplett, Osseointegration of Dental Implants, J. Long-Term Eff Ects Med. Implant. 13 (2003)

485–501.

[165] R. Schwaiger, L.R. Meza, X. Li, The extreme mechanics of micro- and nanoarchitected materials, MRS Bull. 44 (2019) 758–765. doi:10.1557/mrs.2019.230.

[166] L.R. Meza, G.P. Phlipot, C.M. Portela, A. Maggi, L.C. Montemayor, A. Comella, D.M. Kochmann, J.R. Greer, Reexamining the mechanical property space of three-dimensional lattice architectures, Acta Mater. 140 (2017) 424–432. doi:10.1016/j.actamat.2017.08.052.

[167] M.R. O'Masta, L. Dong, L. St-Pierre, H.N.G. Wadley, V.S. Deshpande, The fracture toughness of octet-truss lattices, J. Mech. Phys. Solids. 98 (2017) 271–289. doi:10.1016/j.jmps.2016.09.009.

[168] M.-T. Hsieh, V.S. Deshpande, L. Valdevit, A versatile numerical approach for calculating the fracture toughness and R-curves of cellular materials, J. Mech. Phys. Solids. 138 (2020) 103925. doi:10.1016/j.jmps.2020.103925.

[169] S. Choi, B. V. Sankar, A micromechanical method to predict the fracture toughness of cellular materials, Int. J. Solids Struct. 42 (2005) 1797–1817. doi:10.1016/j.ijsolstr.2004.08.021.

[170] N.A. Fleck, Fracture of brittle lattice materials :A review, Major Accompl. Compos. Mater. Sandw. Struct. An Anthol. ONR Spons. Res. (2009) 1–818. doi:10.1007/978-90-481-3141-9.

[171] ASTM E1820, Standard test method for measurement of fracture toughness, ASTM Int. West Conshohocken, PA, USA. i (2011) 1–56. doi:10.1520/E1820-11.2.

[172] G. Bao, S. Ho, Z. Suo, B. Fan, The role of material orthotropy in fracture specimens for composites, Int. J. Solids Struct. 29 (1992) 1105–1116. doi:10.1016/0020-7683(92)90138-J.

[173] L. Dong, V. Deshpande, H. Wadley, Mechanical response of Ti-6Al-4V octet-truss lattice structures, Int. J. Solids Struct. 60 (2015) 107–124. doi:10.1016/j.ijsolstr.2015.02.020.

[174] S.P. Timoshenko, S. Woinowsky-Krigerm, Theory of Plates and Shells, 2nd ed., Mcgraw-Hill, New York, USA, 1959.

[175] ASTM C393/C393M, Standard Test Methods for Core Shear Properties of Sandwich Constructions by Beam Flexure, ASTM International, West Conshohocken, PA, 2016.

[176] T.D. Gatzke, C.M. Grimm, Estimating Curvature on Triangular Meshes, Int. J. Shape Model. 12 (2006) 1–28. doi:10.1142/S0218654306000810.

[177] T. Surazhsky, E. Magid, O. Soldea, G. Elber, E. Rivlin, A Comparison of Gaussian and Mean Curvatures Estimation Methods on Triangular Meshes, 2003 IEEE Int. Conf. Robot. Autom. (Cat. No.03CH37422). 1 (2003) 1021–1026. doi:10.1109/ROBOT.2003.1241726.

[178] C. Leys, C. Ley, O. Klein, P. Bernard, L. Licata, Detecting outliers: Do not use standard

deviation around the mean, use absolute deviation around the median, J. Exp. Soc. Psychol. 49 (2013) 764–766. doi:10.1016/j.jesp.2013.03.013.

[179] P.K. Tomaszewski, N. Verdonschot, S.K. Bulstra, G.J. Verkerke, A comparative finite-element analysis of bone failure and load transfer of osseointegrated prostheses fixations, Ann. Biomed. Eng. 38 (2010) 2418–2427. doi:10.1007/s10439-010-9966-9.

[180] E. Parzen, On the Estimation of Probability Density Functions and Mode, Ann. Math. Stat. 33 (1962) 1065–1076.

[181] R.A. Davis, K.-S. Lii, D.N. Politis, Remarks on Some Nonparametric Estimates of a Density Function, Sel. Work. Murray Rosenblatt. (2011) 95–100. doi:10.1007/978-1-4419-8339-8_13.

[182] M.A. Wolters, W.J. Braun, A practical implementation of weighted kernel density estimation for handling shape constraints, Stat. 7 (2018) e202. doi:10.1002/sta4.202.

[183] D.R. Carter, M. Wong, The role of mechanical loading histories in the development of diarthrodial joints, J. Orthop. Res. 6 (1988) 804–816. doi:10.1002/jor.1100060604.

[184] M. Wong, D.R. Carter, A theoretical model of endochondral ossification and bone architectural construction in long bone ontogeny, Anat. Embryol. (Berl). 181 (1990) 523–532. doi:10.1007/BF00174625.

[185] D.R. Carter, T.E. Orr, D.P. Fyhrie, D.J. Schurman, Influences of Mechanical Stress on Prenatal and Postnatal Skeletal Development, Clin Orthop. 219 (1987) 237–250.

[186] R.D. Mindlin, Influence of Rotatory Intertia and Shear De-formation on Flexural Motion of Isotropic, Elastic Plates., J. Appl. Mech. 18 (1951) 31–38.

[187] E. Reissner, The Effect of Transverse Shear Deformation on the Bending of Elastic Plates, J. Appl. Mech. 12 (1945) A68–A77.

APPENDIX A

Synopsis of algorithm for spinodal decomposition

The spinodal decomposition equation (Eq. (2-1)) is solved numerically with a Finite Difference scheme, as described in detail in Sun et al., 2013. Here we report the key details of the algorithm for completeness.

Equation (2-1) is solved on a cubic volume with edge length, *L=100*, which is discretized into a lattice of mesh size, $\ell = L/100 = 1$. Let u_{ijk}^{m} denote the discrete value of the phase field variable $u(i,j,k,m\tau)$ at nodal point (i,j,k), where τ is the integration time step (τ =0.005 is chosen as a good compromise between solution accuracy and computational cost, as suggested by [132] and m is the number of time steps.

A finite difference scheme is used to discretize equation (2-1) as:

$$\frac{u_{ijk}^{m+1}-u_{ijk}^{m}}{\tau} = \Delta[\left(u_{ijk}^{m}\right)^{3} - u_{ijk}^{m} - \theta^{2}\Delta u_{ijk}^{m}] \tag{A1}$$

where again θ represents the thickness of the phase A / phase B interface (here chosen as 1.1) and Δ is the Laplacian operator. Equation (A1) is solved with periodic boundary conditions:

$$u(i,j,k,m\tau) = u(i+L,j,k,m\tau) \tag{A2.1}$$

$$u(i,j,k,m\tau) = u(i,j+L,k,m\tau) \tag{A2.2}$$

$$u(i,j,k,m\tau) = u(i,j,k+L,m\tau) \tag{A2.3}$$

and a randomly generated initial condition, $u(i,j,k,0) = u_0(i,j,k,0) \in [-5,5] * 10^{-4} \neq 0$.

Here, phase A ($u=-1$) represents void space, and phase B ($u=1$) represents solid material. As the solution progresses, the system phase separates at relative early times, and subsequently continues to coarsen; during the coarsening phase, the curvature of the

interface between solid and void decreases and the size of the single-phase domains increases.

To enforce a specific relative density (i.e., a prescribed ratio of phase A and phase B regions), the threshold method with the cutoff u_c^m is used. The phase value of point (i, j, k) at time $m\tau$ is defined as:

$$PV_{ijk}^m = H\left(u_{ijk}^m - u_c^m\right) \tag{A3}$$

where $H(u_{ijk}^m - u_c^m)$ is the Heaviside function. When $u_{ijk}^m - u_c^m > 0$, then $PV_{ijk}^m = 1$, indicating the space is occupied by material. When $u_{ijk}^m - u_c^m < 0$ then $PV_{ijk}^m = 0$ indicating void space. For a desired relative density $\bar{\rho}$, the cutoff u_c^m is adjusted such that:

$$\bar{\rho} = \frac{1}{L^3}\sum_1^L\sum_1^L\sum_1^L PV_{ijk}^m = \frac{1}{L^3}\sum_1^L\sum_1^L\sum_1^L H(u_{ijk}^m - u_c^m) \tag{A4}$$

With this approach, dense spinodal topologies with arbitrary relative densities are generated.

APPENDIX B

Algorithm for extraction of curvature probability maps

The principal curvatures of a surface at a point *P*, κ_1 and κ_2, are defined as the minimum and maximum curvatures at that point, respectively. A paraboloid fitting method can be used to extract these curvatures at each point of the shell spinodal meshes, as proposed in [176,177]. The following procedure is implemented: (i) The triangular shell mesh (generated as described in sec. 2.2.3) is imported in Matlab. (ii) For any node *P* in the surface mesh, a number *J* of elements is identified as the set of elements belonging to the three neighboring rings of node *P*, with the first neighboring ring defined as all the elements sharing node *P*, and the next two rings as the elements sharing the boundary nodes of the previous ring. (iii) Unit normal vectors to each element in the set *J* is are constructed by normalizing the cross product of two edges of the element. (iv) The unit normal of the surface at node *P*, $\mathbf{n_p}$, is obtained as the average of the unit normals of all the elements in the first three neighboring rings of the point *P* as follows

$$\mathbf{n}_{\mathrm{P}} = \frac{1}{\mathrm{J}}\sum_{1}^{\mathrm{J}} \mathbf{n}_{\mathrm{e}} \tag{B1}$$

where $\mathbf{n}_{\mathrm{e}}$ is the unit normal of element "e". (v) All the nodes in the first three rings of *P,* along with *P,* are transformed using a rotation matrix such that $\mathbf{n}_{\mathrm{p}}$ align with the z-axis of the global coordinate system. (vi) The transformed coordinates of these nodes are used to least-square fit the coefficients $\mathrm{a_o}$ to $\mathrm{a_5}$ of the biquadratic polynomial surface:

$$\mathrm{z_v} = \mathrm{a_o} + \mathrm{a_1 x} + \mathrm{a_2 y} + \mathrm{a_3 xy} + \mathrm{a_4 x^2} + \mathrm{a_5 y^2} \tag{B2}$$

(vii) The Hessian matrix of the polynomial surface is calculated as:

$$\begin{bmatrix} 2a_4 & a_3 \\ a_3 & 2a_5 \end{bmatrix} \tag{B3}$$

(viii) The pairs of minimum and maximum principal curvatures, κ_1 and κ_2, at *P* are extracted as the eigenvalues of the Hessian matrix. (ix) The process above is repeated to find the principal curvatures at every single node of the spinodal shell mesh. Outliers in κ_1 and κ_2 are determined based on a median absolute deviation method [178], and any (κ_1, κ_2) pair that has an outlier is removed. (x) Principal curvature density function maps are generated as contour plots of the probability density function $P(\kappa_1, \kappa_2)$, defined as:

$$P(\kappa_1, \kappa_2) = \frac{N(\kappa_1,\kappa_2)}{\sum N(\kappa_1,\kappa_2)} \tag{B4}$$

where $N(\kappa_1, \kappa_2)$ is the number of (κ_1, κ_2) pairs having curvatures in the range $[(\kappa_1, \kappa_2), (\kappa_1 + \Delta\kappa_1, \kappa_2 + \Delta\kappa_2)]$. Here, $\Delta\kappa_1 = \frac{\max(\kappa_1)-\min(\kappa_1)}{N_1}$ and $\Delta\kappa_2 = \frac{\max(\kappa_2)-\min(\kappa_2)}{N_2}$, with N_1 and N_2 the number of intervals in κ_1 and κ_2, respectively.

This procedure was used to generate the contour plots in Fig. 2.6.

APPENDIX C

Evaluation of peak stresses

The peak stress, s_{peak} (i.e., the maximum stress) extracted by finite element analysis of architected materials is in general vey localized and mesh sensitive. To allow a robust and unambiguous estimation that allows comparison across different topologies, we define the peak stress in a porous implant as the von Mises stress that is exceeded by exactly one percent of the implant volume (Fig. C1); a similar implementation has been previously used in finite element analyses of bones [179].

The procedure to obtain the peak stress in a porous implant subject to an externally applied compressive effective stress of 10 MPa is as follows:

(1) The load-controlled stress field σ_l is obtained using the relation $\sigma_d/\sigma_l = \sigma_{de}/10$ (all in MPa), where σ_d and σ_{de} are displacement-controlled stress field and displacement-controlled effective stress that can be found from mechanical simulations in section 2.3.

(2) The elemental volume and the von Mises stress at the centroid of each element are extracted as pairs.

(3) The volume-von Mises stress pairs are then fitted with the weighted kernel density estimator [180–182]:

$$f(s|\boldsymbol{p}) = \frac{1}{eh}\sum_{j=1}^{e} p_j \cdot K\frac{s-s_j}{h} \tag{C1}$$

where f is a probability distribution as a function of von Mises stress variable s and probability weight vector $\boldsymbol{p} = [p_1, p_2, \dots, p_e]^T$; p_j is the volume of j-th element divided by the volume of all elements, and e is the total number of elements. K is a symmetric kernel

smoothing function which takes the shape of a normal distribution in this study. h is the bandwidth that controls the smoothness of the resulting probability distribution.

(4) S_{peak} (1% von Mises threshold) is extracted by calculating the inverse cumulative distribution of f such that the probability that a random von Mises stress variable s to take on a value less than or equal to s_{peak} is 99%, $P(s \leq s_{peak}) = 0.99$.

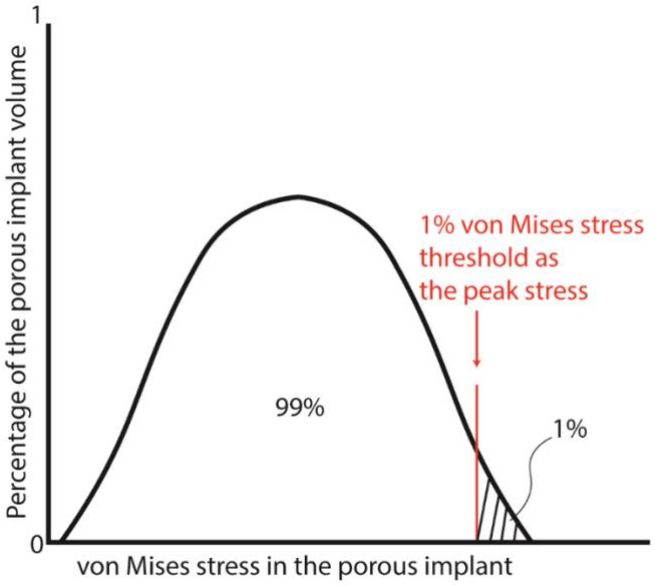

Fig. C1 *Determination of 1% von Mises stress threshold as the peak stress in a porous implant. Percentage of the porous implant volume is defined as the volume of partial implant regions, that have a specific von Mises stress value, divided by the total volume of the implant.*

APPENDIX D

Prediction of long bone growth

Most of the bones in human bodies are long bones such as femurs and tibias. These long bones grow longer through endochondral ossification, the process by which cartilage is gradually turned into bones. It was shown that endochondral ossification is related to the osteogenic index I (defined in [183]) as a linear combination of shear stresses (bone growth facilitator) and compressive dilatational stresses (bone growth inhibitor) experienced in cartilage cells [183–185]; we can write a similar relation for the relative bone growth in the tissues surrounding the implants as a linear combination of average maximum shear strain $\bar{\varepsilon}_{maxs} > 0$ and average compressive volumetric strain $\bar{\varepsilon}_{vol} < 0$, experienced in the tissue matrix phase of the composite models, as:

$$I = V_m \cdot (\bar{\varepsilon}_{maxs} + \kappa \cdot \bar{\varepsilon}_{vol}) \tag{D1}$$

where V_m is the volume of the matrix phase over the volume of the composite and $0 \leq \kappa \leq -\bar{\varepsilon}_{maxs}/\bar{\varepsilon}_{vol}$ is an empirical constant. $\bar{\varepsilon}_{maxs}$ and $\bar{\varepsilon}_{vol}$ are assumed to have the equal weight ($\kappa = 1$) in the current study. Note, I is only a relative index for comparative purposes.

In order to obtain the osteogenic index I for the tissue matrix phase, we perform the following procedures:

(1) The three normal strains ε_{11}, ε_{22}, ε_{33}, the maximum principal strain ε_{maxp} and the minimum principal strain ε_{minp} are extracted at the centroid of each element, together with the volume fraction of the corresponding element — where p is the ratio of the volume of the element to the total volume of the matrix phase.

(2) The quantity ε_{maxs} is calculated as

$$\varepsilon_{maxs} = \frac{(\varepsilon_{maxp} + \varepsilon_{minp})}{2},$$

and ε_{vol} is calculated as

$$\varepsilon_{vol} = \varepsilon_1 + \varepsilon_2 + \varepsilon_3.$$

(3) We then produce two sets of data for all elements, with one consisting of $[\boldsymbol{\varepsilon_{maxs}}\ \boldsymbol{p}]$ and the other consisting of $[\boldsymbol{\varepsilon_{vol}}\ \boldsymbol{p}]$, where $\boldsymbol{p} = [p_1, p_2, \dots, p_e]^T$, $\boldsymbol{\varepsilon_{maxs}} = [\varepsilon_{maxs,1}\ \varepsilon_{maxs,2}, \dots, \varepsilon_{maxs,e}]^T$, $\boldsymbol{\varepsilon_{vol}} = [\varepsilon_{vol,1}\ \varepsilon_{vol,2}, \dots, \varepsilon_{vol,e}]^T$, and e is the total number of elements in the matrix phase.

(4) In order to reduce the effect of extreme high local strains (outliers) on the measures of central tendency, we eliminate all rows in $[\boldsymbol{\varepsilon_{maxs}}\ \boldsymbol{p}]$ whose first component is less than the 0.5th or greater than the 99.5th percentile of $\boldsymbol{\varepsilon_{maxs}}$. Similarly, we eliminate all rows in $[\boldsymbol{\varepsilon_{vol}}\ \boldsymbol{p}]$ whose first component is less than the 0.5th or greater than the 99.5th percentile of $\boldsymbol{\varepsilon_{vol}}$.

(5) Weighted kernel density estimators (A.1) are used to fit $[\boldsymbol{\varepsilon_{maxs}}\ \boldsymbol{p}]$ and $[\boldsymbol{\varepsilon_{vol}}\ \boldsymbol{p}]$ as f_{maxs} and f_{vol} respectively.

(6) $\bar{\varepsilon}_{maxs}$ and $\bar{\varepsilon}_{vol}$ can be calculated as the mean of f_{maxs} and the mean of f_{vol} respectively. $I = V_m \cdot (\bar{\varepsilon}_{maxs} + \kappa \cdot \bar{\varepsilon}_{vol})$ then can be found.

APPENDIX E

Extraction of the minimum number of unit cells for accurate toughness modeling

Linear elastic, small-strain finite element simulations were performed to calculate the minimum number of unit cells along the y-direction, n_y, of SENB specimens in order to secure accurate toughness measurements. The overall specimen dimensions follow the ASTM E1820 standard [171], with aspect ratio of $S = 4W$, $W = 2B$ and $a/W = 0.5$, as shown in Fig. E1 (a). Displacement-controlled boundary conditions were applied as follows (see Fig. E1(a)): (i) A unit displacement of 1 mm was applied along the negative y-direction on the top surface node at the mid-span of the specimen; (ii) Two pin-jointed supports were applied at bottom nodes, distanced $W/4$ away from each end of the specimen, to prevent displacement in the y-direction. (iii) A fixed boundary condition was applied at one of the pin-jointed supports, to prevent rigid body motion in the x-direction. Each bar is represented by a single Euler-Bernoulli beam element (element B23 in Abaqus) with cubic interpolation; these elements can capture the deformation of a slender bar subjected to arbitrary bar end moments and forces in a small strain analysis. We varied the number of unit cells in the y-direction from $n_y = 4$ to $n_y = 45$, while keeping the unit cell size at $\ell = 3$ mm and relative density at $\bar{\rho} = 0.1$. The pre-factor, D, for each topology was then calculated as $D = \mathrm{K_{IC}}/(\sigma_{\mathrm{TS}}\bar{\rho}\sqrt{\ell})$. As these are small-displacement linear elastic analyses, $\mathrm{K_{IC}}/\sigma_{\mathrm{TS}}$ can be replaced by $\mathrm{K_{IC}}/\sigma_{\mathrm{max}}$, where K_I is the imposed mode-I stress intensity factor and σ_{max} is the maximum stress around the crack tip under the imposed displacement. Note that the constituent material properties are immaterial and would not change the results in these analyses. The normalized axial stress contours of triangular specimens with $n_y = 8$ and $n_y =$

40 were plotted in Fig. E1 (b). Maximum axial stress occurred immediately in front of the crack tip; the same conclusion can be drawn for hexagonal and kagome specimen (contours not shown here). The pre-factors *D* for the three topologies were plotted against n_y, and the minimum n_y for sufficient accuracy is then determined as the number of unit cells at which the pre-factor is within 5% of the final converged value. The chosen n_y for hexagonal, kagome, and triangular lattices are 40, 45, and 40 respectively, as shown in red circles in Fig. E1 (c)

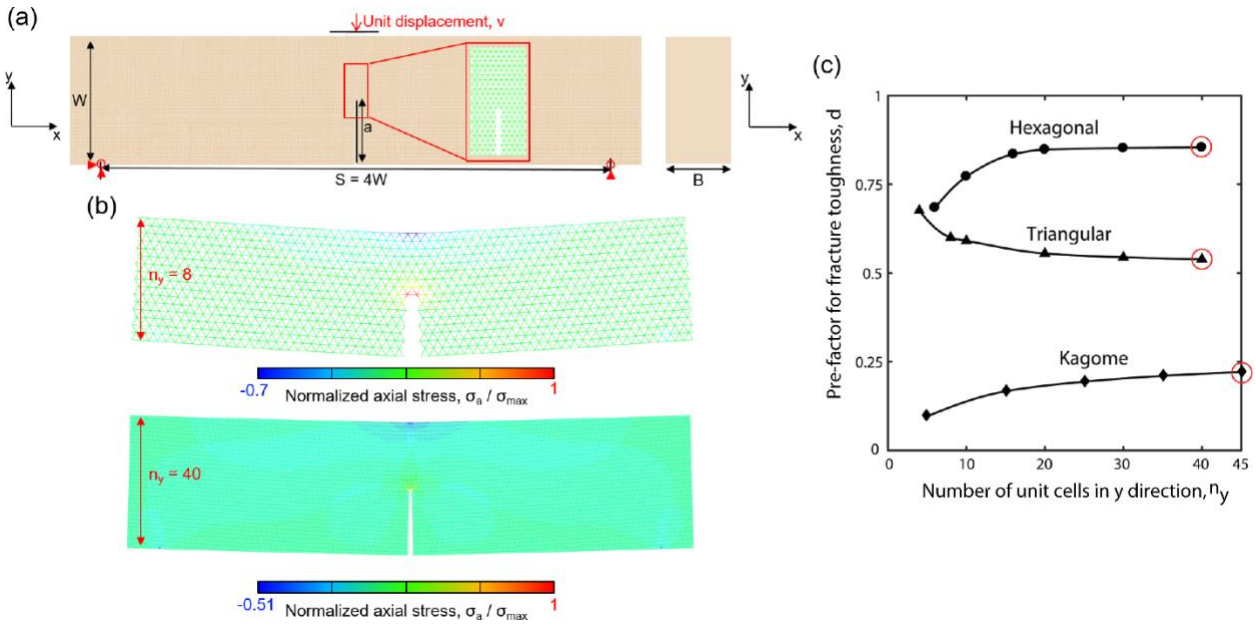

Fig. E1 *Specimen design: number of unit cells. (a) Specimen aspect ratio. (b) Normalized axial stress contour of triangular specimens at number of unit cells,* n_y *= 8 and* n_y *= 40. (c) Convergence of the pre-factor, D, with number of unit cells,* n_y*. The chosen* n_y *for the simulations are circled in black.*

APPENDIX F

Mesh sensitivity analysis

Finite-strain elasto-plastic finite element simulations were performed to determine the number of elements per bar, n_e, required to accurately capture the initial fracture response of SENB specimens. The minimum number of unit cells in the y-direction, n_y, determined for each topology in Appendix E was used in all simulations, while keeping $\bar{\rho}$ = 13% and ℓ = 3 mm. The boundary conditions described in section 4.2.4 were applied. Each bar, representing a Mindlin-Reissner isotropic plate [186,187], was modeled with first-order Timoshenko beam elements (element B21 in Abaqus) for large strain and rotation analyses. To increase computational efficiency, only a rectangular region spanning approximately 10 x 13 unit cells in each in-plane direction around the crack tip has refined mesh, varying from n_e = 4 to n_e = 50 as shown in Fig. F1 (a) and (b). We ensured that this rectangular region encompasses the maximum crack length extension specified in ASTM E1820 [171]. Outside of the rectangular region, each bar is modeled with one Timoshenko beam element. Such coarse meshing far away from the crack tip would only affect local deformation and simulated results would give the fracture response of an ideally scaled-up specimens. Titanium alloy (Ti-6Al-4v) is chosen as representative material, with plane-strain-modified Young's modulus, E_s' = 135 GPa and modified Poisson's ratio, ν_s'= 0.43; the plastic behavior is modeled as $\sigma = \sigma_{ys}(1 + \varepsilon_p{}^n)$, where σ_{ys} = 932 GPa is the initial yield strength, n = 0.7237 is the strain hardening power, and ε_p is the plastic strain; a fracture strain ε_f = 0.1105 is assumed. The load-line displacement at which the maximum axial strain around the crack tip reached ε_f was plotted against n_e. The minimum n_e was then determined as the number

of elements per bar at which the load-line displacement is within 10% of the final converged value. The chosen minimum n_e for hexagonal, kagome, and triangular lattices are 30, 20, and 4 respectively, as shown in red circles in Fig. F1 (c).

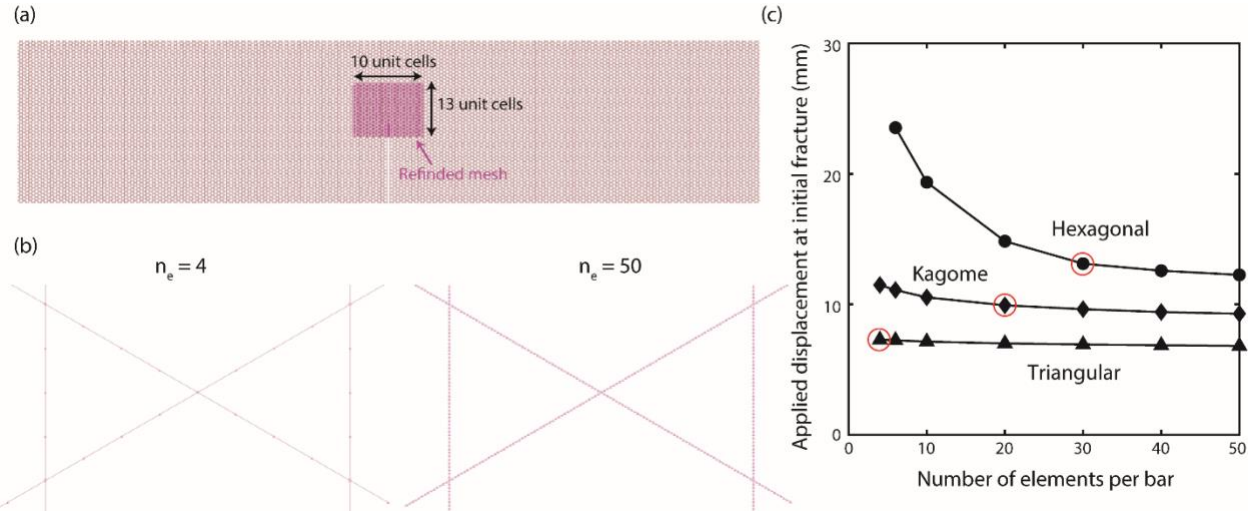

Fig. F1 *Specimen design: number of elements per bar. (a) Demonstration of refined mesh region around the crack tip. (b) Magnified views of mesh seeding around the crack tip with number of elements per bar, n_e = 4 and n_e = 50. (c) Convergence of the load-line displacement, at which the maximum axial strain around the crack tip reached ε_f, with number of elements per bar, n_e. The chosen n_e for simulations are circled in red.*

APPENDIX G

FE linear perturbation analysis to calculate the natural frequencies of 2D lattice materials

Linear perturbation finite element simulations were performed to calculate the natural frequencies, ω_n, of all SENB specimens. Similar boundary conditions as defined in appendix A were applied, but without any loadings, as shown in Fig. G1. The minimum number of unit cells, n_y, and required number of elements per bar, n_e, derived from appendix E and F were used. Titanium alloy (Ti-6Al-4V) was used as constituent material, with modified Young's modulus, E_s' = 135 GPa and Poisson's ratio, ν_s' = 0.43, and density ρ_s = 4,500 kg/m^3. The ten smallest eigen-frequencies with corresponding eigen-modes were first extracted in each simulation. The smallest eigen-frequency with a physical eigen-mode was then taken as the natural frequency. Natural frequencies at each relative density and topology are reported in Table G1. For lattice specimens made of silicon carbide and/or with mass scaling (artificial increase of density in Abaqus to speed up simulation), natural frequencies were inferred proportionally, using $\omega_n = (E_s'/\rho_s)^{0.5}$.

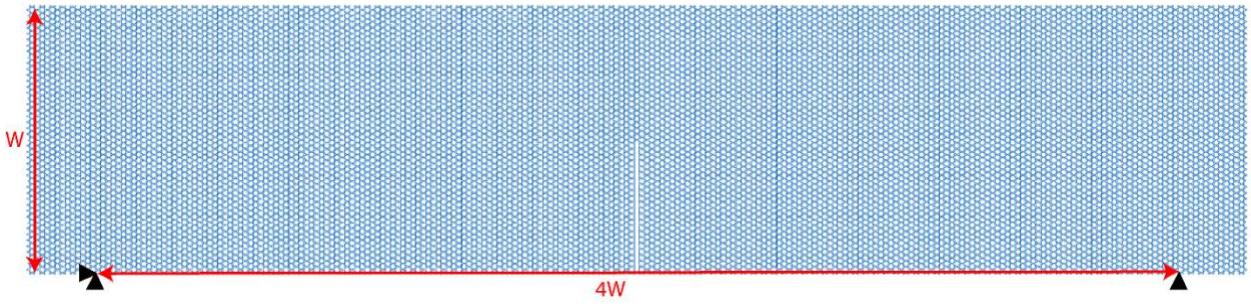

Fig. G1. *Illustration of boundary conditions applied in linear perturbation analyses: (i) two pin-jointed supports at 4W distance apart to prevent translate in the vertical direction and (ii) a fixed boundary condition applied at the left pin-jointed support to prevent rigid body motion.*

Table G1 Natural frequencies of titanium alloy (Ti-6AL-4V) lattice specimens made of triangular, kagome, and hexagonal topologies, at $\bar{\rho}$ = 0.13, 0.16, and 0.2. Base material properties of modified Young's modulus, E_s' = 135 GPa and Poisson's ratio, ν_s' = 0.43, and density ρ_s = 4,500 kg/m^3 were used.

Titanium Alloy Ti-6L-4V	Natural frequency, ω_n(cycles/s)		
Topology	$\bar{\rho}$ = 13%	$\bar{\rho}$ = 16%	$\bar{\rho}$ = 20%
Triangular	202	202	202
Kagome	140	140	140
Hexagonal	51	61	74

APPENDIX H

Fracture toughness calculation procedures

Fracture toughness calculation procedures are taken from ASTM E1820 [171] and summarized below with minor modifications. Fracture toughness is first quantified in terms of J-integral, *J*. *J* is composed of an elastic part, J_{el} and a plastic part, J_{pl}:

$$J = J_{el} + J_{pl} \tag{H1}$$

These components are calculated at instant (i), corresponding to each crack extension (load drop), as $J_{el}\ (i)$ and $J_{pl}\ (i)$ respectively. $J_{el}\ (i)$, is related to mode-I stress intensity factor, K_I as follows:

$$J_{el}\ (i) = \frac{(K_I\ (i))^2}{E} \tag{H2}$$

where E is the effective Young's modulus of the lattice specimens. K_I (i) at each instant of crack extension is related to the load-line reaction force, P (i) as shown in Fig. H1:

$$K_I\ (i) = \left[\frac{4P\ (i)}{B\sqrt{W}}\right] \cdot f\left(\frac{a\ (i)}{W}\right) \tag{H3}$$

where $a\ (i)$ is the crack length at the instant *(i)* and the calibration factor $f(a\ (i)/W)$ is calculated as,

$$f\left(\frac{a\ (i)}{W}\right) = 3\sqrt{\frac{a\ (i)}{W}} \cdot \frac{1.99 - \frac{a\ (i)}{W}\cdot\left(1 - \frac{a\ (i)}{W}\right)\cdot\left(2.15 - 3.93\frac{a\ (i)}{W} + 2.7\left(\frac{a\ (i)}{W}\right)^2\right)}{2\left(1 + 2\frac{a\ (i)}{W}\right)\cdot\left(1 - \frac{a\ (i)}{W}\right)^{1.5}} \tag{H4}$$

As the specimens under investigation are 2D lattices, crack extensions can be visually determined in post-processing. $J_{pl}\ (i)$ is related to the area under the load-line force / displacement curve, $A_{pl}\ (i)$, at instant *(i)* as follows (see Fig. H1):

$$J_{pl}\ (i) = \frac{2A_{pl}\ (i)}{B \cdot (W - a\ (i))} \tag{H5}$$

The fracture toughness at crack extension instant *(i)*, K_J *(i)*, is then calculated as $K_J(i) = (E \cdot J(i))^{0.5}$.

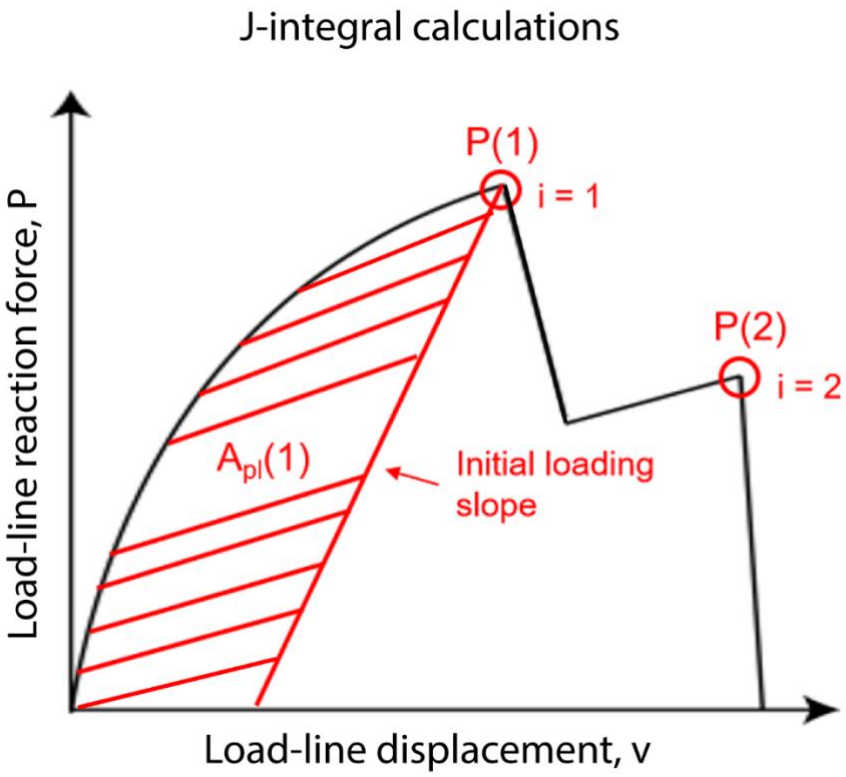

Fig. H1 *Illustration of load-line reaction force, P, versus load-line displacement, v, at crack extension instant i = 1 and 2 with the area under the curve, A_{pl}, at crack extension instant i = 1 for J-integral calculations.*

Supplementary Material

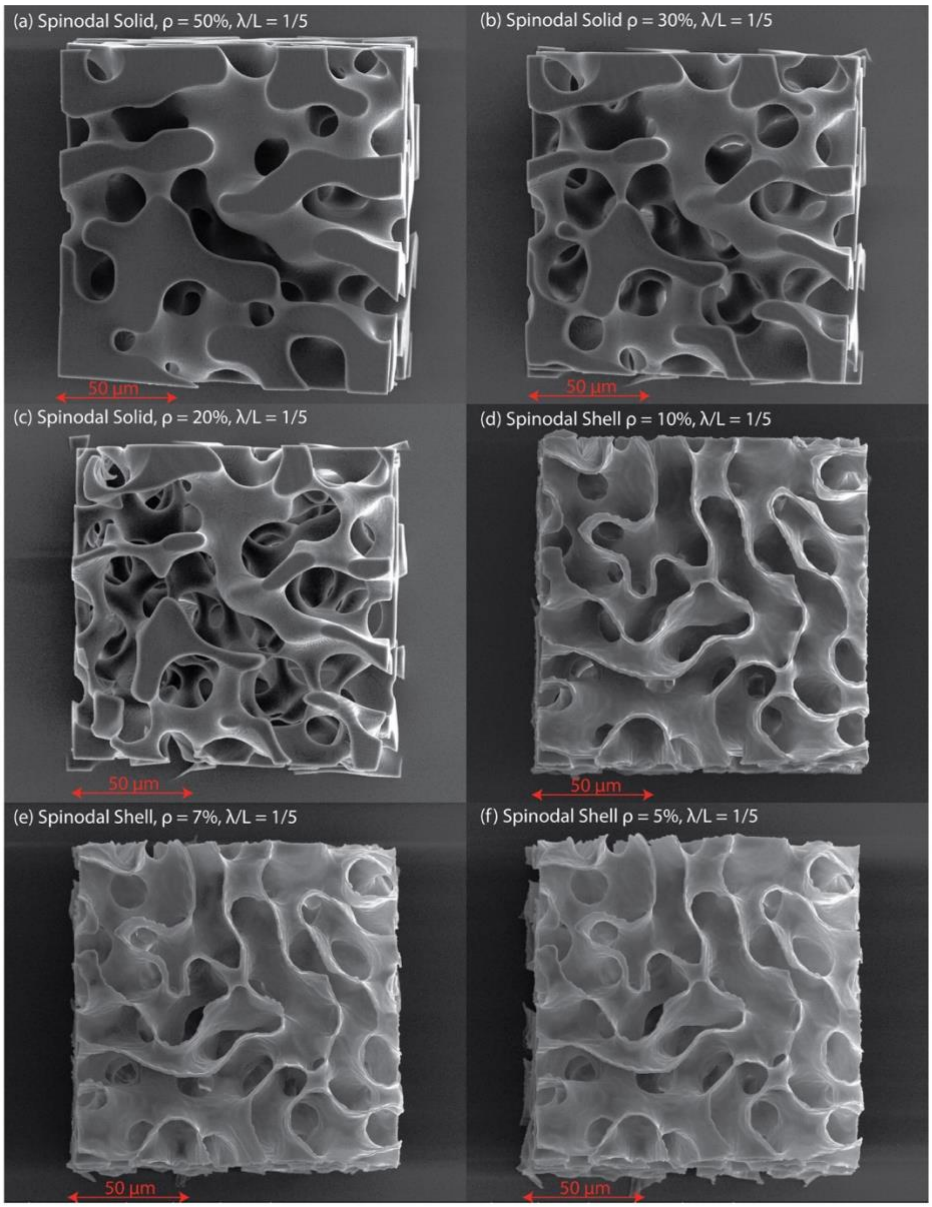

Fig. S1 *SEM images of spinodal samples fabricated in IP-Dip by two-photon polymerization Direct Laser Writing. All samples have characteristic feature size,* $\frac{\lambda}{L} = \frac{1}{5}$*, with L the domain size. (a) Spinodal solid model,* $\bar{\rho}$ *= 50%. (b) Spinodal solid model,* $\bar{\rho}$ *= 30%. (c) Spinodal solid model,* $\bar{\rho}$ *= 20%. (d) Spinodal shell model,* $\bar{\rho}$ *= 10%. (e) Spinodal shell model,* $\bar{\rho}$ *= 7%. (f) Spinodal shell model,* $\bar{\rho}$ *= 5%.*

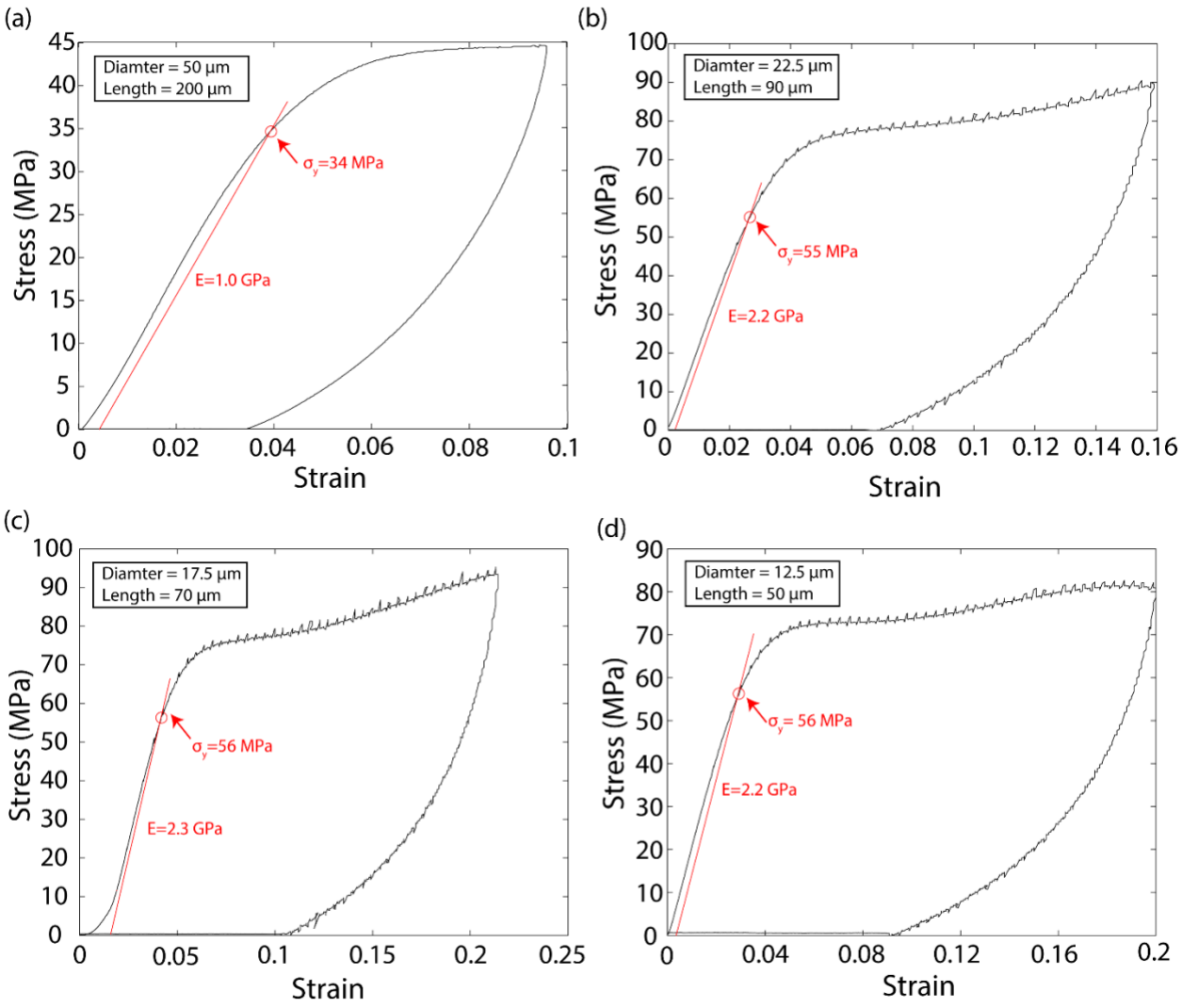

Fig. S2 *Uniaxial response of the material IP-Dip, measured by compression experiments on micro-pillars of aspect ratio of 4 and different diameters, manufactured by two-photon polymerization Direct Laser Writing with a Nanoscribe Photonics GT Professional.*